1-1-2013

Imaging Iron Content In Patients With Multiple Sclerosis Using Magnetic Resonance Imaging

Charbel Abdo Habib
Wayne State University,

IMAGING IRON CONTENT IN PATIENTS WITH MULTIPLE SCLEROSIS USING MAGNETIC RESONANCE IMAGING

by

CHARBEL A. HABIB

DISSERTATION

Submitted to the Graduate School

of Wayne State University,

Detroit, Michigan

in partial fulfillment of the requirements

for the degree of

DOCTOR OF PHILOSOPHY

2013

MAJOR: BIOMEDICAL ENGINEERING

Approved by:

_____

Advisor Date

_____

_____

_____

_____

DEDICATION

I dedicate my work to my family

ACKNOWLEDGMENTS

First and foremost, I would like to thank God for his blessing and for giving me the strength and the opportunity to expand my knowledge in two of the most interesting research areas combined: Engineering and Medicine. The PhD journey is never easy and therefore, it is indeed God's blessings to have the great people around you to support you along this path.

Therefore, I would like to thank my family for their encouragement, for their prayers and for their everlasting support.

I would like to thank my mother, Mrs. Yolla Abdo Habib, for her prayers and constant support. She always taught us to seek the best and never stop! She was always ready to give everything so we can excel and succeed, even though this meaning that we will be far from her! Thank you Mother for this selfless love; you are such a blessing in my life; I hope I can be in my life half of what you have been for us.

I would like to thank my dear wife, Mrs. Rana El Hachem-Habib, for her love, her patience, and her "silent wisdom". Thank you my love for your support even from thousands and thousands of miles away, and for your understanding of how tough this route is and yet…, you honored me by sharing it with me... I love you dearly and looking forward for more and more great challenges and successes to share.

I would like to thank my sister, Dr. Zeina Habib-Adel, for being such an inspiration over the years and for her support and guidance since day one. You are truly the amazing sister and you definitely deserve the best, because you are the best.

I would like to thank my uncles, Fr. Fadi Bou Chebel and Mr. Antoine Bou Chebel, who enlightened me over the years and advised me on making the right steps which led me to this day. I will be in a lifetime debt for everything you have done for me. Thank you!

I would like to thank Dr. E. Mark Haacke, my mentor and my advisor, for giving me the opportunity to train in his lab. Dr. Haacke doesn't only teach his students about Magnetic Resonance Imaging, but he also teaches us how to always make our work "perfect" and never settle for "good"! Thank you for being such a great mentor and advisor, and for all the support you provided during my graduate studies.

I would like to thank my dissertation committee members: Dr. Monte Harvill, Dr. Jiani Hu and Dr. Weiping Ren for their guidance and their constructive critique to make my research more complete and sharp. I would like to thank all the co-authors of my papers, for their contribution to the work. Special thanks go to Dr. Jean Peduzzi, Dr. Kenneth Casey and Dr. Elizabeth Dawe.

I would like to thank the MR Research Facility group, faculty, post docs, graduate students and staff for all their help and advices. I would especially like to thank Mrs. Lisa Brownshidle, Mrs. Rachel Martis-Laze and Mr. Zahid Latif for all their help. I would also like to thank Dr. Jessy Mouannes-Srour and Uday Bhaskar Krishnamurthy for proof reading my dissertation.

Last but not least, I would like to thank all my friends, who, when I was many miles away from home, made me feel I'm home. I would like to thank Mr. Richard Chaaya, Dr. Areen Al Bashir, Mr. Maurice Farah, Ms. Judith Farah, Mr. Emil Pacurar and Dr. Gabriela Trifan. Thank you for all the moments we shared, thank you for all the advices you gave and all the support you provided.

PREFACE

Magnetic resonance imaging is widely used as a diagnostic tool in clinical settings. Being non-invasive and non-ionizing makes it an ideal method to image human subjects in both cross-sectional and longitudinal studies. In the past decade, susceptibility weighted imaging (SWI) has received a great deal of attention in both the research and clinical realms. Due to its new source of contrast compared to conventional MRI, SWI offers new directions in studying the brain and its vasculature as well as imaging magnetic material (such as iron). Imaging iron is important because it is thought to be associated with normal aging and some neurodegenerative disease. For example, in multiple sclerosis (MS), a complex autoimmune neurodegenerative disease, iron involvement has been reported in patients both *in vivo* and post mortem. This iron deposition is believed to be not only associated with the inflammatory process in MS but also with vascular abnormalities in the brain and neck.

In this work, we will first validate the ability of SWI to create contrast based on local iron content and we will use this technique to evaluate iron content in MS patients compared to normal (healthy) subjects. We will present a new means to extract iron content in large areas, which eliminates the effect of averaging (previously used) on data assessment. Finally, in order to study the relation between increased iron content, lesion load and the new theory of vascular involvement in MS (mentioned above), we will introduce the possibility of developing a vascular animal model of MS, by emphasizing the similarities and differences in the human and swine venous drainage system and presenting some preliminary data toward that direction.

TABLE OF CONTENTS

LIST OF TABLES

LIST OF FIGURES

ABBREVIATION LIST

ADHD:	Attention Deficit Hyperactivity Disorder
AFV:	Anterior Facial Vein
BBB:	Blood Brain Barrier
BW:	Bandwidth
CC:	Crus Cerebri
CCSVI:	Chronic Cerebrospinal Venous Insufficiency
CIS:	Clinically Isolated Syndrome
CMG:	Central aspect of Medial Geniculate body
CN:	Caudate Nucleus
CNPase:	Cyclic Nucleotide Phosphodiesterase
CNR:	Contrast to Noise Ratio
CNS:	Central Nervous System
CSF:	Cerebrospinal Fluid
DMT-1:	Divalent Metal Transporter-1
DSS:	Dorsal Sagittal Sinus
EAE:	Experimental Autoimmune Encephalomyelitis
EJV:	External Jugular Veins
FA:	Flip Angle
FDRI:	Field-Dependent Relaxation Rate Increase
FLAIR:	Fluid Attenuated Inversion Recovery
FLASH:	Fast Low Angle Shot
Foxp3:	Fork head box P3 transcription
GD:	Gadolinium

GM:	Gray Matter
GP:	Globus Pallidus
GRE:	Gradient Recalled Echo
HP:	High Pass
HSB:	Human Brain and Spinal Fluid Resource Center
IA:	Intermediate Area between RN and SN
ICC:	Intra-Class Correlation Coefficient Reliability
IJV:	Internal Jugular Veins
IL:	Interleukin
LFB:	Luxol Fast Blue
LMG:	Lateral aspect of the Medial Geniculate body
MAG:	Myelin-Associated Glycoprotein
MFC:	Magnetic Field Correlation
MOG:	Myelin Oligodendrocyte Glycoprotein
MRA:	Magnetic Resonance Angiography
MRI:	Magnetic Resonance Imaging
MRV:	Magnetic Resonance Venography
MS:	Multiple Sclerosis
NAWM:	Normal-Appearing White Matter
PC:	Phase-Contrast
PD:	Phase Difference
PPMS:	Primary Progressive Multiple Sclerosis
PRMS:	Progressive Relapsing Multiple Sclerosis

PT: Pulvinar Thalamus

PTA: Percutaneous Transluminal Angioplasty

PUT: Putamen

QSM: Quantitative Susceptibility Mapping

rf: Radiofrequency

RN: Red Nucleus

ROI: Region of Interest

RRMS: Relapsing Remitting Multiple Sclerosis

RSXRF: Rapid Scanning X-Ray Fluorescence

SD: Standard Deviation

SN: Substantia Nigra

SNc: Substantia Nigra, pars compacta

SNr: Substantia Nigra, pars reticulata

SNR: Signal to Noise Ratio

SPIN: Signal Processing In Nuclear magnetic Resonance

SPMS: Secondary Progressive Multiple Sclerosis

SPSS: Statistical Package for Social Sciences

SS: Straight Sinus

SSRL: Stanford Synchrotron Radiation Lightsource

SWI: Susceptibility Weighted Imaging

SWIM: Susceptibility Weighted Imaging and Mapping

T: Tesla

T1: Spin Lattice Relaxation Time

T2: Spin-Spin Relaxation Time

Tf: Transferrin

TE: Echo Time

THA: Thalamus

TOF: Time Of Flight

TR: Repetition Time

USPIO: Ultra Small Superparamagnetic Particles Of Iron Oxide

v_{enc}: Velocity Encoding

VIBE: Volumetric Interpolated Breath-Hold Sequence

VVVP: Ventral Vertebral Venous Plexus

WM: White Matter

Chapter One

INTRODUCTION

1.1. Background and Project Motivation

Assessing normal human physiological processes and their pathology *in vivo* became possible with the advent of medical imaging techniques. Magnetic resonance imaging (MRI), in particular, is the technique of choice especially in longitudinal studies, since it is a non-invasive and non-ionizing imaging modality (and therefore safe) (Haacke et al. 1999). It has been shown to be sensitive and specific in imaging the human anatomy and function due to its high resolution (which is currently provided at a millimeter level). In most cases, human scanners use proton imaging. In this case, the source of signal for human MR images comes from the proton molecules in the body. Historically, contrast has been based on the spin density and relaxation properties of each tissue although today there are many other tissue properties that can now be imaged including tissue susceptibility (Haacke et al. 2009). This latter property makes it possible to image iron.

Iron, is a paramagnetic molecule, and is known to be the most abundant metal in the brain (Haacke et al., 2007). Its role in the biochemistry of the human body has made it an interesting substance for researchers to investigate including but not limited to its distribution, accumulation over time, and its abnormal deposition in many neurodegenerative diseases such as multiple sclerosis (Hare et al. 2013).

Multiple sclerosis (MS) has long been defined as an inflammatory demyelinating autoimmune disease of the central nervous system (CNS) (Noseworthy et al., 2000b). What initiates the disease and the sequence of events underlying the development of MS is not yet well understood (Noseworthy et al., 2000b). However, technological progress has shed some

important insights on many of the factors involved in the pathology of this complex disease. The pathological landmarks of MS (structural and functional) are characterized by areas of demyelinated plaques mostly in white matter (WM) and altered global as well as local perfusion (Filippi et al., 1998; Haacke et al., 2009a). This is also observed to a lesser degree, in the cortical regions, specifically near the gray matter (GM)/WM boundary and in gray matter as well (Haacke et al., 2009a; Nelson et al., 2007). Determining whether the starting point is in the GM or WM remains unclear (Allen et al., 2001; Neema et al., 2009; Nelson et al., 2007). Finally iron accumulation has been reported predominantly in the deep gray matter (basal ganglia and midbrain) (Adams, 1988; Eissa et al., 2009; Filippi and Rocca, 2009; Haacke et al., 2009a; Varga et al., 2009).

Brain iron accumulation in MS has been shown histologically in the past (Craelius et al., 1982; Levine and Chakrabarty, 2004). Iron deposition was seen in and around white matter lesions (mostly perivenular), in the deep gray matter area (basal ganglia and midbrain) and in an antegrade fashion along the venous drainage system (such as thalamostriate system) (Haacke et al. 2010). This has been hypothetically linked to a new theory known as chronic cerebrospinal venous insufficiency. This study showed that MS patients tend to have extracranial venous abnormalities such as obstruction of the internal jugular veins in the neck and the azygos vein along the thoracic vertebral column (Zamboni et al., 2009), (Haacke et al., 2012c). These abnormalities lead to alteration in the blood drainage from the brain and produce a hemodynamic effect which is thought to be related to the clinical outcomes of MS. These outcomes have increased the research community's interest in assessing iron and flow involvement in MS which might provide clues to the link between white matter lesions, iron content and flow abnormalities.

The motivation for studying iron and its relation with vascular abnormalities in this thesis was therefore based on all the observations mentioned above. Specifically, I will address: 1) the ability of susceptibility weighted imaging in resolving the main structures and substructures of the midbrain which are thought to be affected in neurodegenerative diseases; 2) measuring iron content in MS patients with age matched healthy normal controls *in vivo* as a means to develop a new imaging biomarker for MS; and 3) the possibility of developing a new MS vascular animal model to study the link between vascular abnormalities, iron deposition and sclerotic lesions.

The remaining chapters in this thesis are arranged as follows. Chapter two gives a detailed overview on iron in the body and the brain, its function under normal conditions and its involvement in many diseases ("when it behaves badly"). Chapter three presents the basics of the MR gradient echo concept and how it is used to generate susceptibility weighted magnitude and phase images (which will be used to visualize different structures of the brain and assess their iron content in MS patients and healthy controls). Chapter four uses high contrast SWI data to differentiate between basic mesecephalic structures including the red nucleus, the substantia nigra and the crus cerebri (paper published in AJNR). Chapter five describes the basics of what is known about MS and its clinical manifestation including white matter and gray matter lesions as well as iron deposition. Chapter six tests the specificity of SWI compared to X-Ray fluorescence in imaging iron content in MS cadaver brains (paper published in AIP). In chapter seven, iron in the basal ganglia and the midbrain is assessed using SWI and compared between healthy controls and MS patients (published in AJNR). Chapter eight presents part of our work on developing a new MS vascular animal model where we assess the similarities and differences in the venous drainage system between pigs and humans (published in JMRI). Finally, chapter nine discusses conclusions and future directions.

1.2. Project Aims:

In this dissertation, MRI methods will be used to visualize and evaluate iron content in the basal ganglia and midbrain, to assess whether MS patients (*in vivo* and *ex vivo*) suffer from increased iron content in the brain and to evaluate the similarities between the cerebral vasculature of the swine and the human, as a means to develop a new vascular model for neurodegenerative diseases such as MS. The specific aims and hypotheses of this proposal are:

Specific aim 1: To collect high-contrast SWI data to differentiate between and within the basic mesencephalic structures; namely, the red nucleus, substantia nigra and crus cerebri.

Hypothesis: Using SWI, it is possible to create better anatomical images of the mesencephalon, with improved contrast compared to conventional T1 or T2-weighted sequences.

Specific aim 2: To visualize and validate iron deposition using rapid scanning X-Ray Fluorescence (RS-XRF) and SWI in two MS cadaver brains.

Hypothesis: XRF will show similar contrast as SWI and reveal perivascular iron deposition in MS lesions.

Specific aim 3: To evaluate iron content in the basal ganglia and midbrain of MS patients using SWI and to compare the results to a previously established baseline of normal iron content as a function of age.

Hypothesis: MS patients have much higher iron in the midbrain and basal ganglia than age matched normal controls.

Specific aim 4: To investigate the similarities and differences between the human and pig (swine) cerebral vasculature using MR venography and angiography.

Hypothesis: The swine brain's vasculature and flow will be similar to that in humans, presenting the swine as a good large animal model to study the vascular aspects of MS.

Chapter Two

IRON IN THE BRAIN

Chapter Overview

In this chapter, we explore the most abundant metal in the brain, iron, and we emphasize its importance in the body and in the brain. We describe its different types and their role based on their composition. The iron distribution in the brain and its relation with age are discussed. Pathological examples are given showing the potential role of abnormal iron level in neurological diseases. Finally, common magnetic resonance imaging methods that have been used to image and quantify iron *in vivo* are highlighted.

Introduction

Understanding the pathological role of iron in the brain has been one of the major focuses of neurological research for decades. Iron has been associated with the outcome and potential pathogenesis of many neurodegenerative diseases such as Friedrich's ataxia, Huntington's disease, multiple sclerosis, Parkinson's disease and other iron related genetic diseases (Bartzokis et al., 1994; Beard et al., 1993; Connor and Menzies, 1995; Connor et al., 1995; Gelman et al., 1999; Goodman, 1953; Haacke et al., 2005; Hallgren and Sourander, 1958; Koeppen, 1995; Ogg and Steen, 1998; Ordidge et al., 1994; Pfefferbaum et al., 2009; Quintana et al., 2006; Schenck and Zimmerman, 2004; Schenker et al., 1993; Siemonsen et al., 2008; Stankiewicz et al., 2007; Vymazal et al., 1996; Xu et al., 2008; Zaleski, 1886). The importance of iron homeostasis in the brain is due to its major role in several biological processes such as normal brain metabolism, cell division, mitochondrial function, oxygen transport, neurotransmitter synthesis, electron transfer and myelin production (Quintana et al., 2006; Stankiewicz et al., 2007). However, it is believed that any deviation from homeostasis of iron can cause neurotoxicity leading to a

spectrum of neuropathological outcomes (Quintana et al., 2006; Schenck and Zimmerman, 2004; Stankiewicz et al., 2007). To avoid this issue, living organisms have developed systems to store this excess of iron and work as a buffer against iron overload and deficiency (Ropele et al., 2011).

The normal adult human body contains 3 to 5g of iron. Iron is categorized as being either heme-iron (found in hemoglobin - in this state, iron plays a major role in oxygen transport) or non-heme iron. Non-heme iron can appear in low molecular weight complexes, metalloproteins (such as transferrin), ionic iron, as well as ferritin and hemosiderin (molecules that are responsible for iron storage) (Haacke et al., 2005).

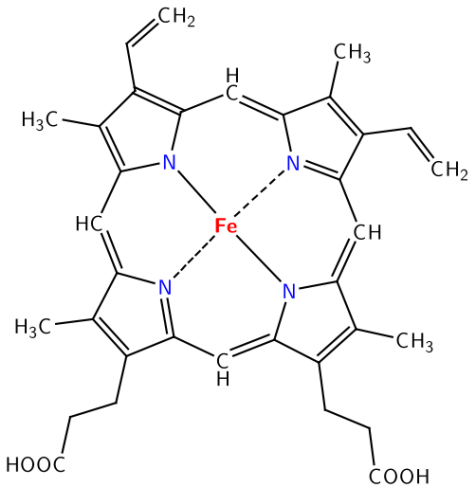

Figure 2.1: The heme cofactor of the protein hemoglobin (Bizzi et al., 1990)

Heme-iron (figure 2.1) contains two thirds of the total iron in the body while the other third appears as non heme-iron mostly in the form of ferritin (Hallgren and Sourander, 1958). Iron appears to preferentially be in the form of ferric (Fe^{3+}) more than in ferrous (Fe^{2+}) iron.

2.1 Iron types

Ferritin (molecular weight = 474kg/mol) is mainly a soluble iron storage protein and barely involved in metabolic activities. It plays a role in maintaining homeostatic levels of iron in the human body. This protein can store up to 4500 iron atoms (figure 2.2). It is composed of twenty four subunits consisting of heavy (H-ferritin) and light (L-Ferritin) subunits. Different combinations of H and L chains define the physiochemical properties of each ferritin protein. H-rich ferritin proteins are more efficient in iron sequestration (where iron uptake is dominant, given that H-chains take up and release iron more rapidly than L-chains) (Beard et al., 1993). Heretofore, H- ferritin is the responsive protein that acts in the early stages of iron accumulation whereas L-subunit ferritin plays a role as storage protein in later stages making L-rich ferritin the proteins of choice for iron storage (Haacke et al., 2005). H-chains are usually found in neurons (oligodendrocytic cells) and L-chains are found in glial cells (macrophages and microglia) (Connor and Menzies, 1995; Connor et al., 1995). Moreover, H-ferritin is dominant in organs that require iron detoxification such as the heart and the brain since its physiological task is to protect cells from the redox active Fe^{2+}. That is why it accumulates almost 90% of non-heme

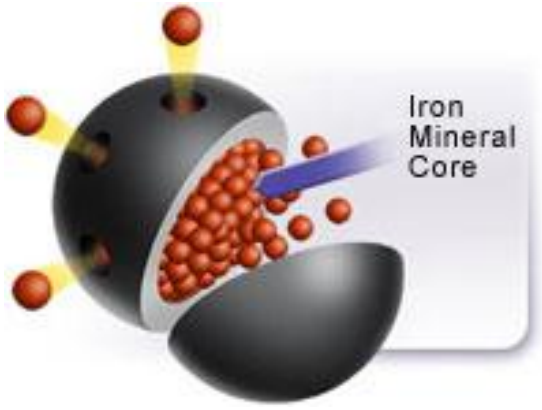

Figure 2.2: Ferritin molecules store thousands of iron atoms within their mineral core. (cdc.gov)

iron in order to provide a cellular protection through its H-subunit. On the other hand, L-subunits are responsible for the facilitation of mineralization (Connor and Menzies, 1995; Connor et al., 1995). These ferritin proteins increase with age except in the substantia nigra, and the ratio H/L decreases with age (Connor and Menzies, 1995; Connor et al., 1995).

Hemosiderin, the second iron storage protein, is insoluble and is considered to be a degradation product of ferritin. Studies have showed that the majority of brain iron in diseased brains is in the form of hemosiderin aggregates rather than isolated ferritin molecules (Schenck and Zimmerman, 2004). For instance, when an extravasation of blood takes place, the brain converts the heme-iron to hemosiderin. This is important when studying subarachnoid hemorrhage (Imaizumi et al., 2003), stroke (Kleinig, 2013), cerebral amyloid angiopathy in dementia (Chao et al., 2006) and in traumatic brain injury (Benson et al., 2012).

Transferrin (molecular weight = 79.6kg/mol) – another non-heme iron protein – plays a role in delivering the iron to the whole body and the brain across the blood brain barrier (from the blood to the brain tissue) via specific receptors located in the microvasculature (Haacke et al., 2005). The transferrin chain (which is composed of two carbohydrate groups and amino acids) can only bind two iron atoms (making transferrin undetectable using magnetic resonance imaging). Transferrin, transferrin mRNA and transferrin receptor expression in the normal brain are related to oligodendrocytes and myelin formation whereas ferritin is a marker for normal and activated microglia in the CNS.

2.2 Iron distribution in the brain

Iron in the brain is heterogeneously distributed, specifically in the white matter, gray matter, and the cerebral cortex (Haacke et al., 2005). Enhancing Perl's staining for visualizing

iron in tissue using diaminobenzidine tetrahydrochlride has revealed more histochemical details showing iron in many cell types of the CNS such as neurons microglia, oligodendroglia, astrocytes and in some myelin sheaths (Koeppen, 1995). Iron and ferritin have been histologically reported to be equally distributed in GM and WM, while transferrin seemed to be more abundant in WM compared to GM (Connor et al., 1992). In the deep gray matter, the structures were found to accumulate ferritin at different rates as a function of age (see next section). Total iron values have been found to be highest in the globus pallidus (GP), followed by the putamen (PUT), caudate nucleus (CN), thalamus, cortical gray matter and cortical white matter as well as in the dentate nucleus (Koeppen, 1995). The distribution of non heme iron is found in the motor cortex with highest concentration followed by, decreasingly, the occipital, sensory, parietal, prefrontal and temporal cortex (Hallgren and Sourander, 1958). Xu et al. showed that the left hemisphere has more iron than the right hemisphere specifically in the PUT, GP, substantia nigra (SN), thalamus (THA) and the frontal WM. However, no significant difference was found while comparing the results according to gender (Xu et al., 2008).

2.3 Iron and Age

Another point of interest in studying iron in the brain is the understanding of its dependability on age. Iron levels have been shown to be low in newborn brain and start increasing rapidly until the age of 20 to 30 years, where it reaches stable levels (Goodman, 1953; Hallgren and Sourander, 1958; Xu et al., 2008; Zivadinov et al., 2010). Iron uptake into the brain reaches its maximum during rapid brain growth which concurs the peak of myelinogenesis (Beard et al., 1993), and continues throughout life. However, some controversies have been reported based on the assessments of specific regions and using different methods (Haacke et al.,

2010c). In the literature, iron deposition as a function of age has been reported for many structures individually (basal ganglia, thalamus and midbrain). For instance, the PUT, pulvinar thalamus (PT) and red nucleus (RN) showed increased iron deposition till the 5th decade and 6th decade, with the highest rate in the first two decades (Hallgren and Sourander, 1958; Zivadinov et al., 2010). Same effect was seen in the CN but at a faster rate in the 4th decade. The GP on the other hand showed an increase till the 3rd decade to reach a plateau at the age of 30. There was no agreement between studies on how does iron behave in the thalamus with age (Zivadinov et al., 2010). One study reported no change as a function of age (Xu et al., 2008); another showed increase linearly with age (Haacke et al., 2010c), while others showed a similar behavior as the GP (Hallgren and Sourander, 1958). Finally, many studies agreed that iron the SN increases rapidly in the first 2 decades of age and reaches a constant value throughout life (Haacke et al., 2010c). Striatal and brain stem structures have higher iron concentrations in older people whereas cortical white matter and thalamus have higher iron concentrations in the younger people (Pfefferbaum et al., 2009). This effect has been seen in the RN and SN as well. As can be seen from the previous discussion, levels of non-heme iron are not uniform spatially or temporally.

In the next section, we will go over some pathologies where iron abnormalities seem to contribute to the etiology of these diseases.

2.4 Iron and Neurodegenerative Disease

Iron misregulation in the body and specifically in the brain, has long been associated with neurodegenerative disease (Sullivan, 2004). The mechanisms of damage linked to iron are differently described based on each disease and yet these mechanisms are still debatable (Hare et

al., 2013). Some studies reported that oxidative stress might be the triggering factor, while others stated that a pathological process leads to iron accumulation and creates a pathophysiological loop involving iron (Hammond et al., 2008). Some of these processes have been identified as cellular, immunological and others as vascular (Haacke et al., 2012b). The complexity of the iron uptake and regulation on a cellular level makes this mechanism susceptible, leading to disruption of its normal function and to cellular degradation and pathogenic pathways.

To emphasize the complexity of this mechanism, the following paragraph will briefly go over iron circulation and brain uptake. A more detailed description of these mechanisms can be found in the review by Hare el al. (Hare et al., 2013).

Transferrin is the major iron transporter in the body. It can hold two iron molecules each. At a given time, and under normal conditions, only 30% of transferrin proteins are occupied. Once in the blood and occupied, Fe_2Tf cannot cross the blood brain barrier due to the hydrophobic barricade. To cross the blood brain barrier (BBB), Tf binds to Tf receptors, which pass through the brain capillary endothelial cells, as an endocytotic mechanism. Another way of iron import to the cell is through low molecular weight complexes. Export of iron is regulated by ferroportin, which is manipulated by the expression of tau and ceruloplasmin, controlling the available iron in the so-called labile iron pool. The latter is regulated by cellular metal sensing and iron binding protein expression (such as ferritin), based on the status of iron and the demand by the cell. Controlling iron homeostasis doesn't only happen with iron regulation, but can also be manipulated via regulation of iron associated proteins. For instance, Tf export from the cell is done through divalent metal transporter-1 (DMT-1). The proper function of DMT-1 will play a role in the availability of apo-Tf which in charge of binding to iron and deliver them under iron overload or depletion conditions (Hare et al., 2013). This shows the number of factors involved

in iron regulation and therefore, it can be expected that disturbance of iron metabolism can occur at several levels: iron uptake and release, storage, intracellular metabolism and regulation (Stankiewicz et al., 2007).

When any of these iron levels are disturbed, neurochemical effects go into play leading to perturbation of neurotransmitter signaling and variation in energy and myelin production (Hare et al., 2013). These changes lead to a spectrum of pathogenic pathways based on their role in maintaining a healthy body. One would expect that changes in the neurotransmitter levels will affect motor skills, language, mood and attention. One well-known disorder that manifests in hyperactivity, inattention and impulsiveness is attention deficit hyperactivity disorder (ADHD). It is believed that the involvement of iron in dopamine neurotransmission might be play a role in ADHD if brain iron deficiency occurs (Konofal et al., 2004). In addition, the brain is always in high energy demand. Given that mitochondrial enzymes do frequently utilize iron, iron depletion might impair their function leading to a decrease in energy production and increase in oxidative stress (Walter et al., 2002). On the other hand, when production of myelin is in jeopardy, one would expect a series of neurological symptoms due to the decrease integrity of the neurons. Although this is still an underexplored subject, iron accumulation and demyelination accompany many neurodegenerative diseases, including Parkinson's disease, Huntington's Disease and Multiple Sclerosis (Quintana, 2007; Stankiewicz et al., 2007). In the past, abnormal iron deposition assessment was only possible postmortem; however, with recent advances in imaging techniques, it became possible to not only visualize but also monitor these changes *in vivo*. These techniques are discussed in the next section.

2.5 Iron as seen with MRI

The ability of MRI to create an image of the human body lies behind the fact that its signal originates from the protons of the water molecules. In addition, the contrast generated is based on the tissue properties of each structure whether via total water content, relaxation times or other imaging characteristics. The presence of metals in sufficient amount will alter the magnetic properties of the tissue and generate a contrast change (via relaxivity and susceptibility effects), making it possible to visualize and quantify them *in vivo*. However, if other metals also exist in the brain but in small concentrations (such as copper, zinc, etc…), their presence will not affect the quantification of iron given that their effects on the local magnetic field is negligible.

There has been considerable interest in normal brain iron quantification as well as in neurodegenerative diseases in order to understand their pathogenesis, monitor their progress and establish neuro-protective treatments (Hagemeier et al., 2013; Langkammer et al., 2013; Lim et al., 2013; Muhoberac and Vidal, 2013; Yang et al., 2013). Developing and improving MRI has been an important task for decades, trying to establish a correlation between the observed signal and iron concentration. Ferritin and hemosiderin are the two major molecules that are considered to be the only forms of non-heme iron present in sufficient quantities to affect MR contrast in the brain (Haacke et al., 2005). On the other hand, iron related proteins such as transferrin, transferrin receptor and the ferritin receptor protein are almost undetectable using MR due to their low concentrations.

Many MR imaging techniques have been used to measure iron *in vivo* due to the effect of iron on signal intensity. As described below, each technique has its advantages as well as its drawbacks. While some MRI sequences did not achieve a strong correlation with iron (such as T2, for example), many others showed promising results for iron evaluation such as T2′ and T2*

quantification (Gelman et al., 1999; Ordidge et al., 1994) as well as Field-Dependent Relaxation Rate Increase (FDRI) (Bartzokis et al., 1993), magnetic field correlation (MFC) (Jensen et al., 2009), and susceptibility weighted imaging (SWI) (Haacke et al., 2010c).

T2, T2 and T2' weighted imaging:*

Relaxation rates (R2, R2* and R2') are reported to increase with an increase in the concentration of paramagnetic material (Haacke et al., 2005). Therefore, in the presence of iron, darkening or hypointensities are visualized in structures with high iron deposition. In addition, T2* and T2 both decrease with increasing magnetic field. The drawback of R2 (also R2* given that R2* = R2 + R2'), is its sensitivity to not only iron but also water content, which makes R2 an imprecise method to evaluate iron when diseased tissue is imaged. For instance, if a lesion with edema is imaged, it has high water content, which will lead to a decrease in R2, and therefore, iron content will be underestimated. Therefore, R2' has become a better, more accurate approach to image iron, as it takes out the water fraction effect and makes it possible to evaluate the signal change due to local susceptibility variations seen in the presence of iron. These measures have been reported to better correlate with iron concentration. Although R2 showed more sensitivity to GM/WM differentiation then R2′, R2 was not able to present specificity for iron (Ordidge et al., 1994). On the other hand, R2′ showed a good correlation with iron load (Schenker et al., 1993). In another study, T2′ and T2* decreased in GM but increased in WM in the aging brain (Siemonsen et al., 2008). More detailed discussion of these concepts, as used in this thesis, will appear in chapter 3.

T1 weighted imaging:

T1 weighted imaging has also been used as a means to investigate iron in the brain. Iron can create a dipolar relaxation mechanism, during which water protons sense magnetic field fluctuation created by ferritin and water diffusion in its vicinity. This dipolar relaxation has an effect on the longitudinal magnetization and, theretofore, a signal increase is seen on T1 weighted images. Based on this mechanism, T1WI can correlate iron concentrations in the brain as seen in postmortem brains (Ogg and Steen, 1998; Vymazal et al., 1996) and shows a good linear dependency on iron, but with a lower effect compared to T2. In addition, T1 effect is field dependent and falls off at higher field while T2 is field independent (Vymazal et al., 1996).

Phase Imaging:

Phase is proportional to local magnetic field changes. The latter is proportional to the local magnetic susceptibility which is a direct measure of local iron content. Phase has been shown to be sensitive to iron and shows a strong correlation as a function of age (Haacke et al., 2010c). More recently, phase has been used to generate a quantitative susceptibility map (Zheng et al., 2013), which also correlates well with iron deposition. This approach takes away the dependability of phase on spatial susceptibility distribution and orientation and avoiding many of the problems currently faced with phase alone (Schafer et al., 2009). The ability of phase to image iron will be described in more detail in the next chapter.

Several other techniques have been used to image iron *in vivo* but will not be discussed in details here. Of these methods, FDRI (which evaluates the differences in R2 at two different field strength), was used by Bartzokis et al. to image iron content and has shown a good agreement with iron concentration (ferritin specific) in normal aging (Bartzokis et al., 1993); and MFC

Imaging (Jensen et al., 2009) (which is composed of a series of asymmetric spin echo sequences giving a T2* like contrast to evaluates microscopic field variations as a means to assess iron content).

Each of these methods mentioned above has its drawbacks, however, some methods will always present relative measures (relaxation times and MFC approaches), while others will offer (when all confounding factors are eliminated) an absolute quantification approach by directly evaluating and mapping magnetic susceptibilities (such as QSM). It is strongly noted that although phase and susceptibility effects seen on MR images exhibit a strong contrast between white matter and gray matter, this contrast is not solely generated by iron; instead, myelin sheaths which are wrapping the neuronal bundles in the WM are diamagnetic, which decreases the susceptibility values in the region of interest and underestimates iron contact in these regions (Liu et al., 2011). This chapter presented an overview on iron and its role in the human body and brain and discussed some pathological consequences when iron deviates from its normal levels. We also listed some approaches which are currently in use to evaluate iron content *in vivo*. In the next chapter, we will talk in depth about one of these MR methods, phase imaging, acquired using gradient echo acquisition scheme, and which will then be used to evaluate iron content in normal controls and MS patients as will be described in chapters 4, 6 and 7.

Chapter Three

SUSCEPTIBILITY WEIGHTED IMAGING

Chapter overview

In the past decade, susceptibility weighted imaging (SWI) has received a great deal of attention in both the research and clinical realms (Haacke et al., 2009b; Mittal et al., 2009). Due to its new source of contrast compared to conventional MRI, SWI presents new directions in studying the brain and its vasculature as well as other organs in the body, where magnetic materials (source of contrast) seem to play an important role in normal aging and disease states of these structures. In this chapter, we will explore the basic concepts of SWI, ranging from basic physics, image acquisition to post processing and creation of the magnitude, phase and SW images which will be used in later chapters to image the brain and assess iron content *in vivo*. We will emphasize the effect of susceptibility on the MR signal, the gradient echo acquisition scheme used in SWI, and how phase will be used to generate the SW image contrast.

Introduction

As emphasized in its name, SWI highlights the susceptibility differences between tissues, presenting a new type of contrast different from what is seen in spin density, T1 and T2 weighted imaging (Haacke and Reichenbach, 2011). The information that underlies this new contrast comes from the phase images which prior to the introduction of SWI were disregarded for a long time in MR applications. As we will see in the next few sections, phase reflects the sources of magnetic material distribution, albeit often in a non-local fashion. The steps used to create SW images are shown in figure 3.1 (Haacke and Reichenbach, 2011) , and will be described in detail throughout this chapter.

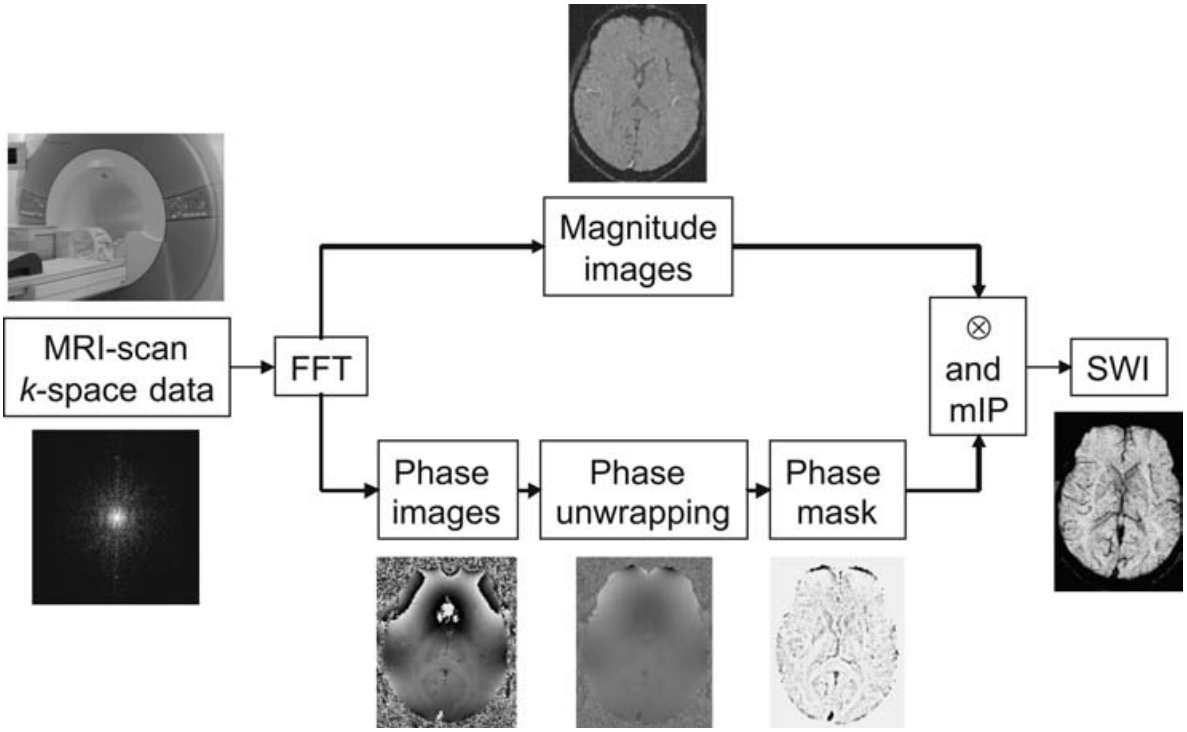

Figure 3.1: Steps involved in creating SW Images

In brief, SW images are acquired based on a 3D, fully flow compensated, high resolution gradient echo sequence. The 3D high resolution nature of SWI allows for the acquisition of thinner slices which reduces the signal loss from background field homogeneities (Haacke et al., 2009b). To make the phase images useful, a special high pass filter is applied to remove unwanted low spatial frequency undulations and aliasing artifacts. This new filtered phase image is used to create a phase mask that is then applied onto the magnitude image. The final SW image combines both magnitude and phase contrast: the former coming from the T2* effects and the latter reflecting susceptibility effects. The details of these steps will be expanded in the remaining sections of this chapter.

3.1 Magnetic Susceptibility

Magnetic susceptibility is defined as the tendency of a substance to become magnetized when it is placed within an external static magnetic field (Haacke et al., 1999). Once magnetized, an induced magnetic field (M) is seen inside the object and will lead to perturbation in the magnetic field outside the object to a different degree based on the object shape, volume, magnetization and position. The full expression for the magnetic field inside the material, under the influence of the magnetic field (B_0), is given by Equation 3.1:

$$\mathbf{B} = \mu_0 (\mathbf{H}+\mathbf{M}) \qquad (3.1)$$

where B is the resultant magnetic field in Tesla (T), H is the magnetic flux in A/m, M is the bulk magnetization per unit volume of the substance in A/m, and μ_0 is the absolute permeability of free space ($4\pi \times 10^{-7}$) with units of Tm/A.

M inside the object and the H field are related through the magnetic susceptibility χ:

$$\mathbf{M} = \chi \mathbf{H} \qquad (3.2)$$

Therefore, Equation (3.1) can be re-written as:

$$\mathbf{B} = \left(\frac{1+\chi}{\chi}\right) \mu_0 \mathbf{M} \qquad (3.3)$$

For linear materials with $\chi << 1$, equation (3.3) can be written as:

$$\mathbf{M} = \chi\mathbf{B}/\ \mu_0 \qquad (3.4)$$

showing the proportionality between the induced magnetization, the main field and the magnetic susceptibility (Haacke et al., 2009b). Based on the value of χ, the material can be characterized as paramagnetic ($\chi > 0$), diamagnetic ($\chi < 0$) and ferromagnetic ($\chi >> 1$). Ferromagnetic materials are not reported in biological organisms, however, paramagnetic forms of iron and diamagnetic forms of calcium are both found in humans (Haacke and Reichenbach, 2011).

Based on what we discussed earlier, any object placed within an external magnetic field gets magnetized (based on its susceptibility) and usually changes the induced magnetic field within and outside the object (Haacke et al., 1999). These changes have a high dependence on the object geometry and its orientation with respect to the main magnetic field. These field changes are easily calculated for objects with structural symmetries like a sphere and a cylinder. These two geometries are convenient given that blood vessels can be modeled by long cylinders and sinuses are modeled by spheres. The derived solutions for these structures implicitly explain what we see on phase images when we look at structures like vessels. Following equation 3.4 and considering that the objects are in vacuum, the field perturbation inside and outside these objects are summarized in table 3.1. However, when these objects are embedded in an external medium with some finite susceptibility, χ is replaced by $\Delta\chi$, in addition to other terms related to the geometry of the external compartment (Haacke and Reichenbach, 2011).

From the concepts described above, tissues with different susceptibilities will exhibit spatially varying precession frequencies as manifest through the Larmor frequency that is given by:

$$\boldsymbol{\omega} = -\gamma.\mathbf{B} \qquad (3.4)$$

where γ is the gyromagnetic ratio of the proton, **ω** is the precession angular frequency and B is the induced magnetic field seen by the proton. How this signal is acquired will be the topic of next section.

Table 3.1: Expressions for Field Inside and Outside a Uniform Sphere and an Infinitely Long Cylinder (Haacke and Reichenbach, 2011).

	Internal Field	External Field
Sphere	B_0	$B_0 + \frac{\chi B_0}{3} \cdot \frac{a^3}{\lvert\mathbf{r}\rvert^3} \cdot (3\cos^2\theta - 1)$
Cylinder	$B_0 + \frac{\chi B_0}{6} \cdot (3\cos^2\theta - 1)$	$B_0 + \frac{\chi B_0}{2} \cdot \frac{a^2}{\lvert\mathbf{r}\rvert^2} \sin^2\theta \cos 2\phi$

In this table, a is the radius of the cylinder or the sphere; θ represents the angle that the long axis of the cylinder makes with B_0 or the angle that the position vector r of the point of observation makes with the main magnetic field B_0 for the spherical case; r is the position vector of the point of observation and Φ is the polar angle subtended by r on the plane perpendicular to the long axis of the cylinder.

3.2 Gradient Echo Imaging

In the presence of an external magnetic field (B_0), the proton spins tend to align in a parallel and anti-parallel fashion along B_0, based on their thermal and magnetic energy. Spin excess in the direction of the main field leads to a bulk magnetization M (Haacke et al., 1999). In order to be able to measure an MR signal, M should be tipped away from the main magnetic field direction. A time varying radiofrequency pulse perpendicular to M, corresponding to the

precessional frequency of M (known as Larmor frequency – eq. 3.4), is applied to the system. Once in the transverse plane, the net magnetization starts precessing along B_0, creating a varying flux across the receiving coil and generating an electromotive force (emf). The measured emf is is referred to as the free induction decay (figure 3.2). This decay is caused by intrinsic interactions of the spins (dephasing) and field inhomogeneities (Haacke et al., 1999). The latter was addressed historically by the use of the spin echo. The spin echo sequence used a π-pulse to invert the phase of these spins and create an echo. However, these sequences take long time, limiting the ability to rapidly acquire high resolution MR data. With a modern system, where global field inhomogeneity has become less of a problem, and the availability of dependable time varying gradients, a more modern concept known as gradient recalled echo (GRE) imaging has become routinely used in every clinical MR application (Haacke and Reichenbach, 2011). The advantages of GRE relies on the fact that short echo times are possible eliminating a lot of artifacts from the T2* signal decay. In addition, the use of high bandwidth decreases the distortion.

GRE imaging uses large and fast switching gradients to dephase and rephase the MR signal in order to create an echo or multiple echoes based on the application (Haacke et al., 2009b). Figure 3.3 represented an example of a 1D gradient echo showing the dephasing, the rephasing and the echo. In the figure on the left, the gradient is dephasing the spins between t_1 and t_2. In the figure on the right, the spins are rephased when the polarity of the gradient has switched, creating an echo at time $t = t_4 – (t_4-t_3)/2$ (Haacke et al., 1999). When the spins are refocused in the MR signal, only the dephasing created by the gradients is reversed and not the phase shifts from the field inhomogeneities, tissue susceptibilities and the chemical shift fields.

Some of these effects will be dealt with later by the application of special filters (high pass filter: see section 3.4).

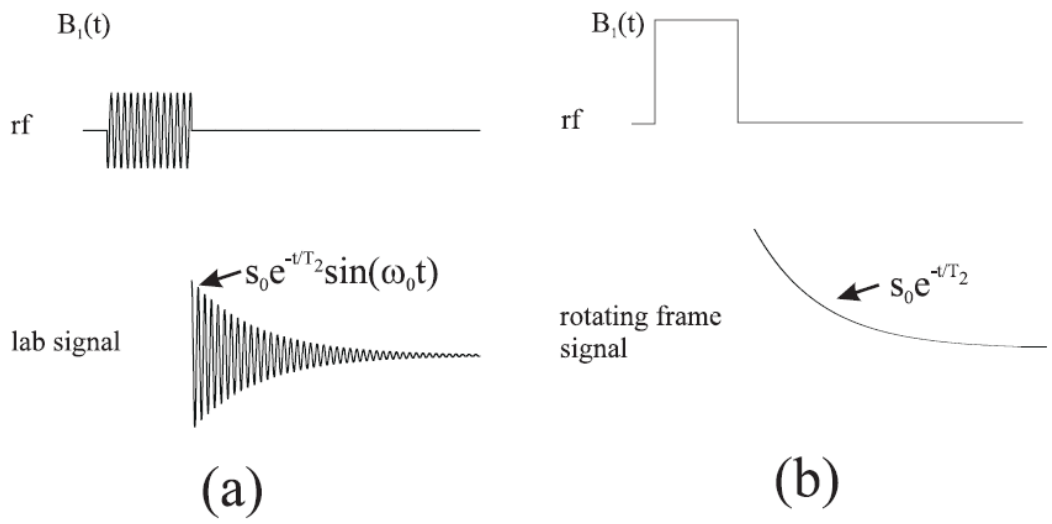

Figure 3.2: a) Free induction decay in the laboratory frame. b) the free induction decay signal in the rotating frame.

Understanding the effect of imaging parameters on gradient echo sequences is very important. For instance, in order to collect a 2D or 3D dataset, the diagram shown in figure 3.3 should be repeated many times (Frahm et al., 1986). The repetition time (TR) will now play an important role in manipulating the available signal. Therefore, it is critical to understand how TR affects the available magnetization at each repetition time in both the longitudinal and transverse planes. In the cases were TR is much longer than T2 relaxation, transverse magnetization tend to vanish prior to the next rf pulse. However, when TR is shorter than T2, transverse magnetization is still available and needs to be removed prior to the next acquisition. On the other hand, longitudinal magnetization availability is affected by TR and the flip angle (FA). The right combination of TR and FA will be required to get the best contrast and signal to noise in the

image (Haacke and Reichenbach, 2011). To get a better flavor of this concept, we will introduce the concept of steady state gradient echo imaging.

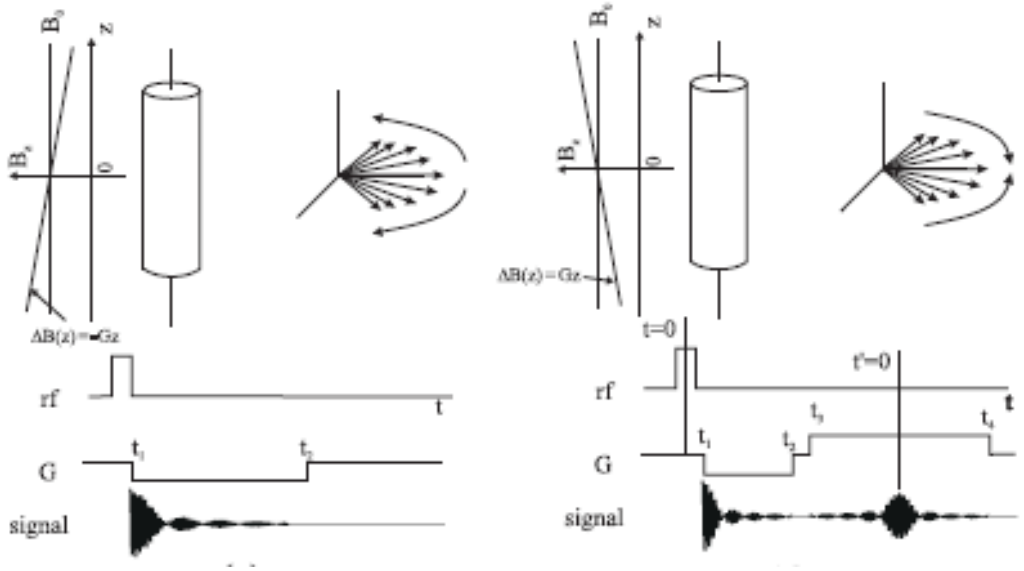

Figure 3.3: 1D gradient Echo experiment.

The repetition of the rf pulse prior to data collection is needed to reach magnetization equilibrium. This will depend on the FA used for that case. For large flip angles, the equilibrium is reached with only few rf pulses compared to several hundred rf pulse with low flip angles (Frahm et al., 1986; Frahm J, 1986). The equilibrium longitudinal magnetization is given by equation 3.5:

$$M_{ze} = M_0 . (1-e^{-TR/T1})/(1-\cos\alpha . e^{-TR/T1}) \qquad (3.5)$$

A clear dependence on both FA and TR is seen in equation 3.5. The transverse equilibrium magnetization based on eq. (3.5) is given by:

$$\rho_m(\alpha) = M_\perp = M_0 . (1-e^{-TR/T1})/(1-\cos\alpha . e^{-TR/T1}) . \sin\alpha . e^{-TE/T2^*} \quad (3.6)$$

Taking the derivative of eq. (3.6), one can show that the maximum signal occurs at the Ernst angle α_E with:

$$\alpha_E = \cos^{-1}(e^{-TR/T1}) \quad (3.7)$$

where $\alpha_E = \sqrt{\frac{2TR}{T1}}$

when TR<<T1 (Haacke et al., 1999).

Equation 3.6 can tell us a little more about how changing the parameters affect the image contrast. For instance, at low flip angles, the image becomes dominated by spin density contrast for TE much smaller than T2*. On the other hand, T1 weighted imaging is achieved when a large flip angle is selected.

The acquired MR signal is a complex signal which can be represented by a magnitude and phase (Haacke et al., 2009b):

$$S_{xy}(t) = |S_{xy}(0)| \, e^{i\varphi(r, t)} \quad (3.8)$$

The MR scanner hardware is used to demodulate the signal into real ($S_x(t)$) and imaginary ($S_y(t)$) channels. The final images usually output on the scanner are the magnitude of the complex signal $|S_{xy}(t)|$ and the phase image (equal to $\tan^{-1}(S_y/S_x)$) (Haacke et al., 1999). This phase is dependent on the position of the spin and the time. Therefore, phase is represented as:

$$\varphi(r, t) = -\omega_0.t + \gamma(B(r))t = -\gamma\Delta Bt \text{ (with } \Delta B = g\Delta\chi B_0) \quad (3.9)$$

B(r) shown in eq. (3.9) includes the susceptibility information in addition to field variations due to chemical shifts and global geometry. As shown in the spherical and cylindrical cases, field variation can occur not only locally inside the object but also external to the object as well. These field variations were the main reason why the phase images were usually disregarded in the past. Finally, adding the phase component to eq. (3.6) yields:

$$\rho(\alpha) = \rho_m(\alpha)\, e^{-i\gamma\Delta BTE} \quad (3.10)$$

Now that we have explained the concept of gradient echo imaging, we will move forward to a more detailed description of how this imaging approach is applied to acquire SW images.

3.3 Susceptibility Weighted Imaging

SWI is a 3D, fully flow compensated, rf spoiled gradient echo sequence (figure 3.4) (Haacke and Reichenbach, 2011) . The terminologies mentioned herein will be described one at a time. 3D sequences are generally used to allow a higher resolution imaging in plane and through plane (better definition independent of the rf pulse). In some cases, the signal to noise of the dataset acquired is higher compared to 2D. 3D imaging is achieved by exciting a slab to cover the area of interest and then the data is spatially resolved in the 3D volume by applying partition, phase and frequency encoding. In addition, flow is compensated in all three directions (Haacke et al., 1999). The reason we are interested in applying flow compensation apart from avoiding motion artifacts is our interest in the phase that results from local susceptibility.

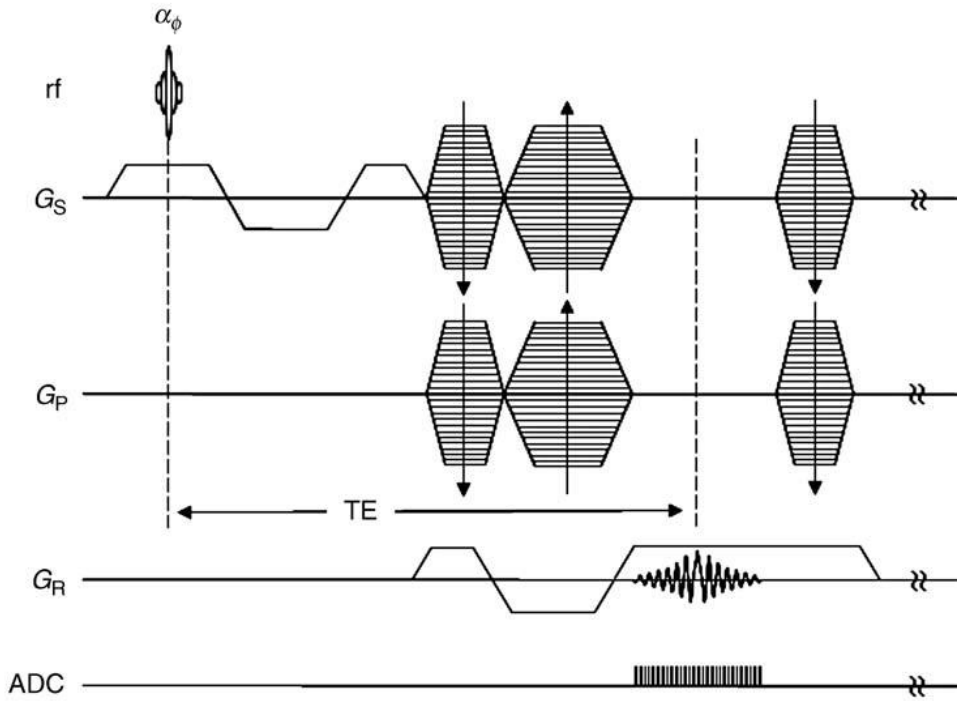

Figure 3.4: Original sequence diagram for SWI with flow compensation.

For uncompensated sequences, the presence of flow in the vasculature of the brain along the bipolar dephasing/rephasing gradient direction leads to an additional accumulation of phase to what was shown in eq. (3.8) (Haacke et al., 1999). A spin moving with a constant velocity v along the read gradient will have phase of:

$$\varphi = \gamma G_x v \tau^2 \qquad (3.10)$$

Therefore, using a first order gradient moment nulling in the read and slice select direction and applying appropriate velocity compensating gradient waveforms in the phase and partition encoding gradients will lead to a full flow compensation, by removing all the accumulated phase from flow at echo time in addition to removing all the pulsatility effects

caused by variable phases across the cardiac cycle. On the other hand, signal variations caused by varying inflow, can only be removed by using low flip angles which reduce T1 dependence on the signal. Given the short TR used in SWI, transverse magnetization is usually still available prior to the second rf pulse. Therefore, gradient and rf spoiling methods are applied in every repetition to ensure no remnant magnetization is found in the transverse plane (Haacke and Reichenbach, 2011). The former is achieved by including variable gradients between rf pulses (after data acquisition) while the latter is achieved by varying the phase of the rf pulse (usually 117 degrees) as a function of the rf number. Resultant magnitude and phase images are shown in figure 3.5 below.

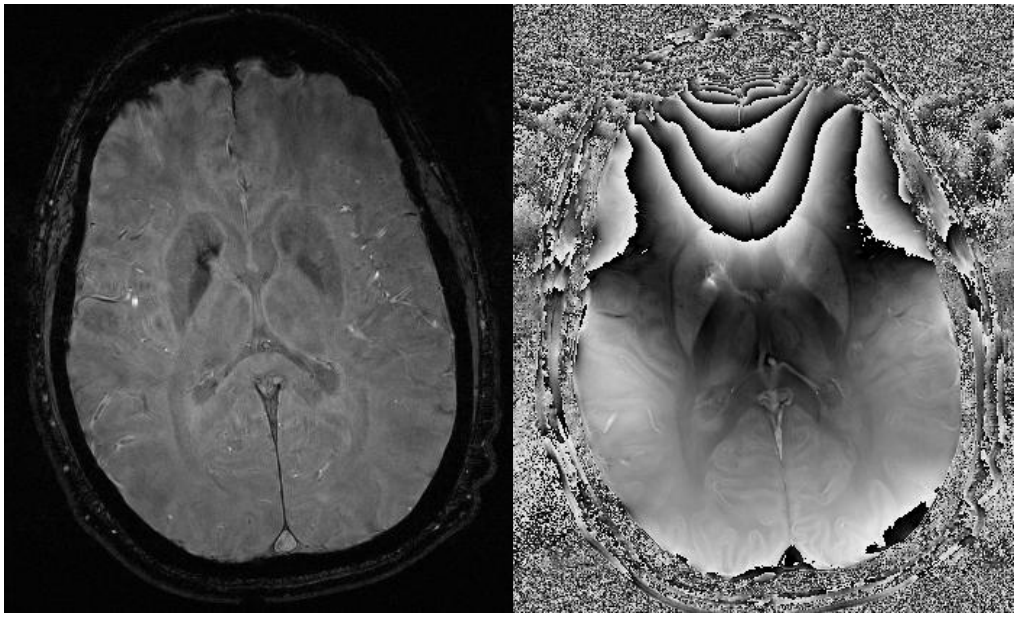

Figure 3.5: SWI magnitude and phase images acquired at 4T with a TR/TE/FA of 35/25/15.

3.4 SWI filtered Phase Images (Homodyne High Pass filter)

The images in figure 3.5 show beautiful contrast between different structures of the brain, however, the phase image on the right is confounded by unwanted artifacts resulting from low

spatial frequency components of the background field ($\Delta B_{global\ geometry} + \Delta B_{main\ field}$) (Haacke et al., 2009b). To make this image more useful, a high pass filter is applied. This high pass filter is created by using an n x n low pass filter divided into the original phase image. This is mathematically represented by equation 3.11 below:

$$\rho'(r) = \rho(r) / \rho_n(r) \qquad (3.11)$$

where $\rho_n(r)$ represents the truncated n x n complex image.

This filter size can vary from as little as 16 x 16 for a 512 x 512 original image, to 96 x 96. However, it should be noted that choosing too large a high filter size can remove useful information from large structures, decreasing their contrast and adding an error in quantification studies based on phase images. Studies have shown that a 64x64 filter size does a good job removing low spatial frequency components while maintaining useful information in the phase data (Haacke et al., 2007). An example showing the effect of different filter size is shown in figure 3.6.

As mentioned earlier, this approach presents in a single image the susceptibility contrast from the phase images and the signal intensity contrast (based on T2*) from the magnitude images. This is accomplished by creating a binary mask from the phase images, which suppresses phase of certain values.

For instance, when the negative phase is of interest, the binary mask sets all the phase values at point x, which are positive to 1, and emphasizes the negative values (Haacke et al., 2009b). This negative mask is given mathematically in equation (3.12):

$$f(x) = \begin{cases} [\pi + \varphi(x)]/\pi & \text{for } -\pi < \varphi(x) < +\pi \\ 1 & \text{otherwise;} \end{cases} \quad (3.12)$$

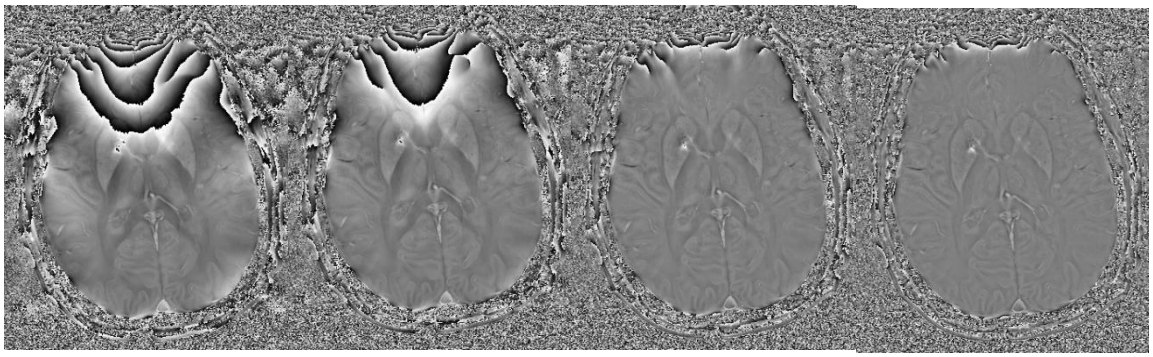

Figure 3.6: Applying a high pass filter of different sizes. From the left, 16x16, 32x32, 64x64 and 96x96 respectively.

This mask can be applied more than once. It has been shown that applying this mask four times fits best for all phase values in the image (Haacke et al., 2009b). An example of SWI images is shown in figure 3.7. This is an MS patient imaged at 4T. The SWI image is mipped over 8 slices to better enhance the vessel connectivity between slices, presenting a new contrast that is not seen in either magnitude or phase images alone.

The link between the susceptibility of a material and the final MR image has been carefully tailored throughout the chapter. The discussion has shown that the presence of magnetically susceptible material such as iron for instance, can be visualized and "relatively" measured by phase shifts in the MR signal. The SWI acquisition and processing scheme tries to reduce the effect of other phase contributors (flow compensation, high pass filter, short TE and TR, low flip angle), to make sure that what we measure is reliable. In the next chapters, we will use the phase images to assess iron content in the brain. The word "relatively" which was

emphasized before informs the reader that an absolute quantification of iron derived from phase is not robust yet due to many contributing factors in the imaging method itself and the imaged object (Haacke et al., 2009b).

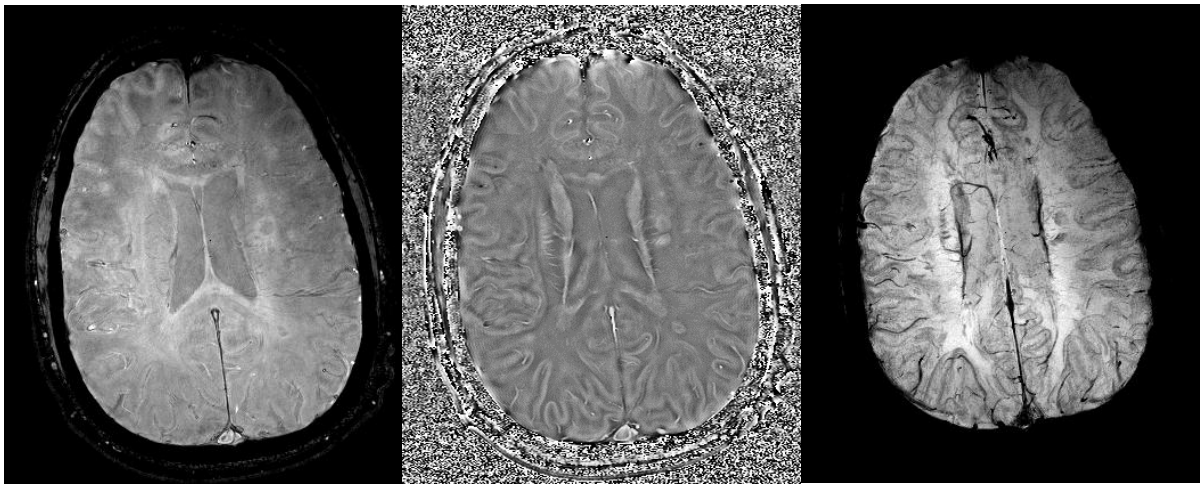

Figure 3.7: Magnitude, phase and SWI images (mipped over 8 slices) showing sclerotic white matter lesions (red arrows), created from the 3D GRE sequence described in this chapter.

In the next chapter, we will assess the contrast to noise ratio and the signal to noise ratio of the SWI images compared to conventional MRI, and test its ability to image the midbrain and resolve its different structures and substructures.

Chapter Four

CHARACTERIZING THE MESENCEPHALON USING SUSCEPTIBILITY WEIGHTED IMAGING

Introduction

In recent years, imaging of neurodegenerative disorders like Alzheimer's, Parkinson's and Huntington's disease have attracted much attention. Most of these diseases' pathological landmarks have been found in parts of the brainstem, especially in the mesencephalon. The substantia nigra, which is the primary source of dopamine synthesis and whose pathways are known to involve iron (Sofic et al., 1991) is affected in a number of diseases. Its atrophy and/or altered functionality could lead to a disruption of dopamine balance in the brain and may lead to motor and/or cognitive deficits. Two other structures involved in coordinating motor function are the crus cerebri (located lateral to the substantia nigra) and the red nucleus, which has connections to the cerebellum and the spinal cord via a number of key motor tracts. The progression of Alzheimer's, Parkinson's and Huntington's diseases has been thought to be associated with an increase in iron content in the red nucleus and substantia nigra (Sohmiya et al., 2004). Therefore, the ability to differentiate among mesencephalic structures should be helpful in visualizing specific damage to these structures and establishing better diagnoses for neurodegenerative diseases (Kim et al., 2007; Semnic et al., 2005; Sofic et al., 1991; Sohmiya et al., 2001; Sohmiya et al., 2004).

To date, T1-, T2- and T2*-weighted magnetic resonance imaging (MRI) methods have been used to image the mesencephalon (Gelman et al., 1999). Generally, the workhorse in anatomical measurements has been 3D T1-weighted gradient-echo imaging. This approach is often done with a magnetization-prepared, rapid acquisition gradient-echo (MP RAGE) approach that uses an inversion pulse followed by the slice encoding gradients and then loops over the

phase encoding gradients (Mugler and Brookeman, 1990). Alongside MP RAGE, a short-TR, low flip angle, gradient-echo fast low-angle shot (FLASH) sequence with radiofrequency spoiling can be used for T1 contrast (Frahm J, 1986). As an example of applied research in imaging the mesencephalon, Shibata, et al. (Sasaki et al., 2006) used T1-weighted imaging to investigate changes in neuromelanin levels in the lower tegmentum. Unfortunately, such T1-based sequences provide rather poor information about upper mesencephalic structures where high vascularization is present (Sofic et al., 1991) and where accurate differentiation between gray matter structures is needed. T2 imaging shows the substantia nigra and the red nucleus quite well but does not distinguish between their substructures (such as the pars reticulata and pars compacta of the substatia nigra, or the capsule and interior structures of the red nucleus). Today, at 3T and 4T, resolution can be pushed easily to 0.5 mm x 0.5 mm x 2 mm. This level of resolution should allow for good 3D imaging of the mesencephalon given that the structures of interest are only about 1 cm thick and require thin slices to be evaluated in detail.

Recently, a method called susceptibility weighted imaging (SWI) has been developed to enhance contrast in T2*-weighted imaging (Haacke et al., 2004; Reichenbach et al., 1997). It is acquired using a fully flow-compensated gradient-echo imaging method in order to pick up extra information from local susceptibility variations in tissue via the phase image (in the past, phase was usually discarded as not being useful clinically). Due to the fact that the phase signal is sensitive to local field change effects, phase data are used as a new source of contrast. When the MR data are collected, there are both real and imaginary components. These are then rearranged to create magnitude and phase images. The phase images contain information about local static field variations, geometry-induced field variations and the local tissue susceptibility of interest here. The first two components tend to have low spatial frequency and can be mostly eliminated

by applying a high pass filter. The resulting high pass filtered phase images can be considered to be a reasonable representation of the local tissue susceptibility (Haacke et al., 2007). Susceptibility changes can be caused by deoxygenated blood (due to the paramagnetic nature of deoxyhemoglobin), brain iron (in the form of ferritin or hemosiderin proteins), or calcium (which is diamagnetic). The SWI filtered phase images are themselves of anatomic interest and can be used to measure the putative non-heme iron content in the basal ganglia and in other areas of the brain (Haacke et al., 2007). The SWI filtered phase images can also be modified to produce a phase mask that is then multiplied into the magnitude images to create a set of SWI magnitude images (Haacke et al., 2004; Reichenbach et al., 1997). These new images now carry unique information from the phase and provide improved contrast between veins, arteries and surrounding tissue.

Although SWI has been used to show individual images of the mesencephalon previously (Abduljalil et al., 2003; Chakeres et al., 2002; Haacke et al., 2007; Haacke et al., 2004; Rauscher et al., 2005), no one has yet performed a systematic and quantitative analysis of the contrast between the different structures of the midbrain. In the present work, we quantify contrast between and within structures in the human mesencephalon at 1.5T and 4T using SWI. Specifically, the following structures will be shown on SWI filtered phase images: the red nucleus and its various vascular subcomponents, the capsule of the red nucleus, the substantia nigra pars compacta, the substantia nigra pars reticulata, the crus cerebri, the medial geniculate body, the sub-thalamic nucleus, the lateral geniculate body and the fascicula nigrale (pallidal-nigral pathway). The contrast of these structures, provided by SWI filtered phase images, will be shown to correlate with the contrast defined by the vascular content in the mesencephalon, highlighted by the India ink staining of cadaver brains in Duvernoy's work (Duvernoy, 1999).

High-resolution examples covering the entire mesencephalon (5 slices, each 2 mm thick) will be shown at both 1.5T and 4T.

Materials and Methods

Five volunteers (23 to 27 years old for SWI; 36 to 56 years old for T1 and T2) were imaged at 1.5T (Siemens Sonata, Erlangen, Germany) and another five volunteers (23 to 27 years old for SWI; 29 to 45 years old for T1 and T2) were imaged at 4.0T (Bruker/Siemens Medspec, Ettlingen, Germany). Institutional review board approval was obtained and all participants signed the appropriate consent forms. All images were collected in a predominantly axial orientation following the AC/PC line. Detailed imaging protocols are given below.

1.5T imaging protocol

A segmented echo-planar imaging sequence (5 echoes) was used for the SWI scans. The sequence was collected with a resolution of 0.5 mm by 0.5 mm by 2 mm, 64 slices, TR = 71 ms, TE = 40 ms, BW = 130 Hz/pixel, FA = 20°, a matrix size of 512x512, and an acquisition time of 8 minutes, 57 seconds. The conventional 3D T1-weighted images were collected with a resolution of 0.5 mm by 0.5 mm by 2 mm, 64 slices (with a parallel imaging factor of 2), TR = 20 ms, TE = 5.58 ms, BW = 130 Hz/pixel, FA = 25^{o}, a matrix size of 512x512, and an acquisition time of 4 minutes, 11 seconds. The T2 data were collected with a resolution of 0.5 mm by 0.5 mm by 4 mm, 25 slices, TR = 5230 ms, TE = 106 ms, FA = 160 ^{o}, BW = 130 Hz/pixel, a matrix size of 512x384, and an acquisition time of 4 minutes, 47 seconds.

4T imaging protocol

A fully flow-compensated gradient-echo sequence was used with parallel imaging (for a factor-of-two drop in acquisition time) for the SWI scans. The sequence was collected with a resolution of 0.5 mm by 0.5 mm by 2 mm, 64 slices, TR = 24 ms, TE = 15ms, BW = 80 Hz/pixel, and FA = 12^{o}, a matrix size of 512x512, and an acquisition time of 12 minutes, 52 seconds. The 3D T1-weighted images were collected with a resolution of 0.5 mm by 0.5 mm by 2 mm, 64 slices (with a parallel imaging factor of 2), TR = 20 ms, TE = 5.58 ms, BW = 130 Hz/pixel and FA = 25^{o}, a matrix size of 512 x 512, and an acquisition time of 4 minutes, 47 seconds. The T2 data were collected with a resolution of 0.8 mm by 0.8 mm by 3 mm, 36 slices, TR = 4950 ms, TE = 72 ms, FA = 150^{o}, BW = 120 Hz/pixel, a matrix size of 320x240 and an acquisition time of 4 minutes, 53 seconds.

Evaluating the SWI data

The data were processed with in-house Visual C++-based software called SPIN (Signal Processing In NMR). SWI data were processed using a 64 x 64 high-pass filter to create a filtered phase image. Window level adjustments were made to view the best image contrast. In measuring contrast, the signal for a given structure was measured from a 100-200 pixel region of interest (ROI) drawn within the structure of interest. For all sequences, contrast-to-noise ratios (CNRs) were calculated between a variety of structures as the signal difference between two structures (S_a, S_b), divided by the noise (σ), or $(S_a - S_b)/\sigma$. The noise was calculated as 0.8 times the mean of a 100-200 pixel ROI outside of the head and away from phase encoding artifacts (a region where only noise was present). Since the structures measured are bilateral, the CNR for a given structure was measured from the ROI having the best apparent contrast. Where the

appropriate contrast was visible, we calculated the CNR between: (1) the red nucleus and the intermediate area (separating the red nucleus from the substantia nigra); (2) the red nucleus and its capsule; (3) the capsule of the red nucleus and the intermediate area; (4) the substantia nigra and the intermediate area; (5) the substantia nigra and the crus cerebri; (6) the substantia nigra pars compacta and the substantia nigra pars reticulata; (7) the substantia nigra pars compacta and the intermediate area; (8) the substantia nigra pars reticulata and the crus cerebri; (9) the lateral and central aspects of the medial geniculate body; and (10) the central aspect of the medial geniculate body and the intermediate area. Background noise was also evaluated outside the image and compared with the standard deviation seen inside the ROI. Each subject data set was carefully scrutinized to find the five or six slices associated with the mesencephalic structures of interest. The MR results were compared to the measurements of mesencephalic capillary density in cadaver brains by Duvernoy, who (using 3-mm-thick slices) performed India ink staining and 5% gelatin injections to highlight anatomical differences.

Results

The area reviewed in the mesencephalon is shown in figure 4.1. A comparison between T1, T2 and SWI contrast, alongside Duvernoy's India ink-stained results, is shown in figure 4.2.

Overall, there is little contrast in the T1 images, while the T2 images show good contrast for the red nucleus and substantia nigra. The SWI images, however, show good contrast with details of the internal structures visible for the red nucleus, the substantia nigra, the crus cerebri and the medial geniculate body (figure 4.3). On the SWI filtered phase images, we see the red nucleus broken up into a highly vascularized portion and a less-vascularized portion. The images from Duvernoy show the horseshoe effect of the vascularized red nucleus, and this is well-

mimicked in the SWI results (figure 4.4C, D: *arrow 4.4a*). Also, the connecting tissue from the substantia nigra is seen to course laterally through the crus cerebri (figure 4.4C, D: *arrow 1*). The substantia nigra can occasionally be seen as having two parts: the pars reticulata (the lateral portion, containing more iron; figure 4.4: *arrow 2a*) and the pars compacta (the medial portion, containing slightly less iron; figure 4.4: *arrow 2b*). Similar to the behavior seen in the red nucleus, the dark, more vascularized region in the lateral aspect of the medial geniculate body is visualized in SWI (figure 4.4: *arrow 6*). Finally, the pallidal-nigral pathway (the fascicula nigrale)—which may transport iron between the substantia nigra and globus pallidus—is also seen (figure 4.4B-D: *arrow 5*). Much of these structures' anatomy changes with each 2 mm-thick slice and many details would not be visible with thicker slices.

In terms of capillary density, the patterns shown in Duvernoy's work appear to be duplicated in the SWI phase images. In addition to the differentiation displayed within the substantia nigra, the red nucleus is seen to contain two regions: a highly vascularized horseshoe area and a brighter central region (figure 4.4C, D: *arrows 4.4a, b*). In general, the local decrease in phase correlates with the darkened patterns of vascularization in Duvernoy's work.

In terms of quantitative tissue differentiation, we have found that SWI provides good contrast, especially when considering all components of the mesencephalon. CNR results are provided in Table 4.1 for 1.5T and Table 4.2 for 4T. The effect of improved SNR at high field and reduced T2 is evident in the images themselves wherever iron content is high. In SWI, the CNR generally increases from 1.5T to 4T, but this increase is dependent on the structure of interest. In some cases (in the medial geniculate body, for example) the CNR increases by a factor of three from 1.5T to 4T. In other cases, there is only a 25% increase in CNR (in the red nucleus, for example).

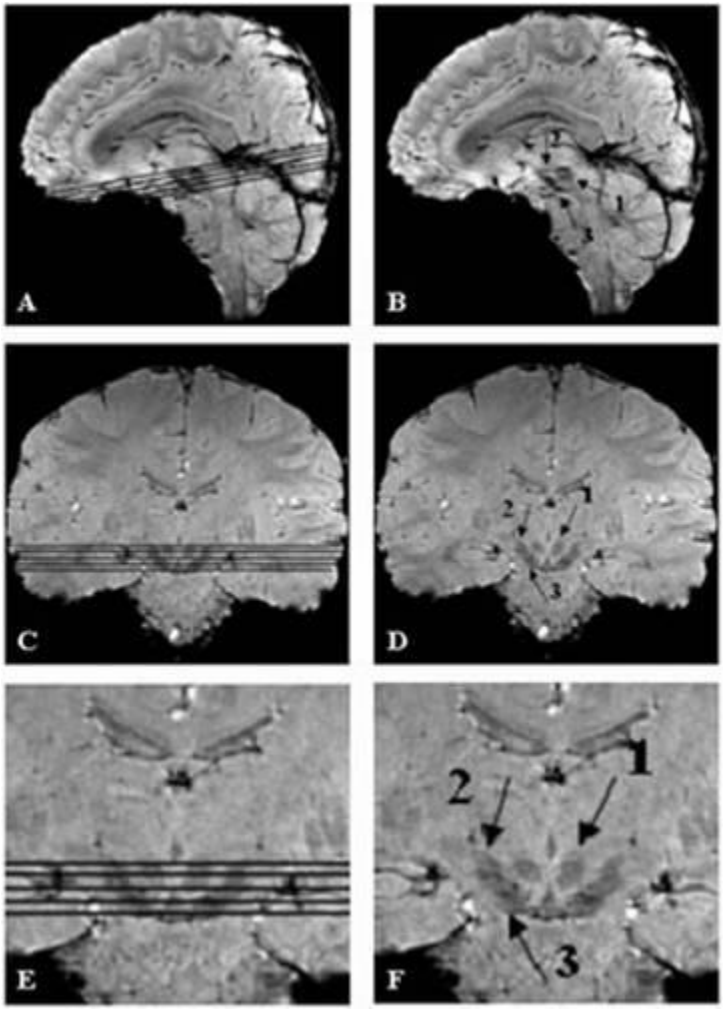

Figure 4.1: *A-F*, The midbrain as a region-of-interest on 4T SWI magnitude images shown in sagittal and coronal sections, with and without slice locators. Arrows 1, 2 and 3 point to the red nucleus, the subthalamic nucleus and the substantia nigra, respectively.

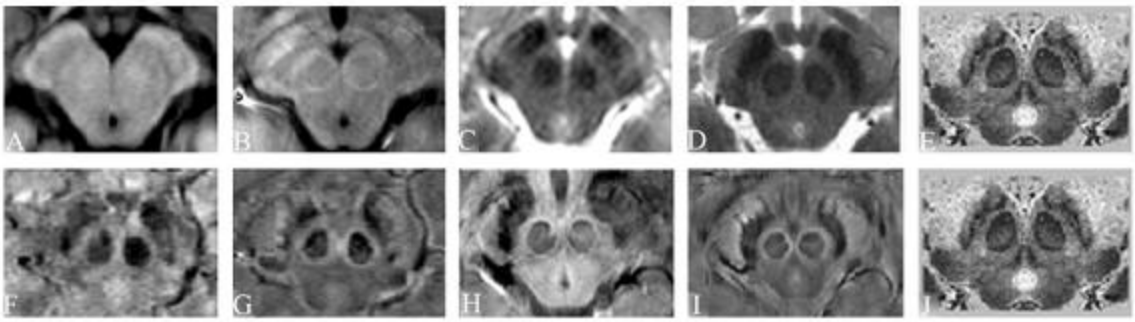

Figure 4.2: A comparison of one region of the mesencephalon for different sequences and field strengths with Duvernoy's stained cadaver brain results. *A*, T1 at 1.5T; *B*, T1 at 4T; *C*, T2 at 1.5T; *D*, T2 at 4T; *E*, Duvernoy's India ink-stained image; *F*, SWI magnitude at 1.5T; *G*, SWI high-pass filtered phase at 1.5T; *H*, SWI magnitude at 4T; *I*, SWI high-pass filtered phase at 4T; *J*, Duvernoy's India ink-stained image. (Images (E) and (J) obtained with kind permission of Springer Science and Business Media.)

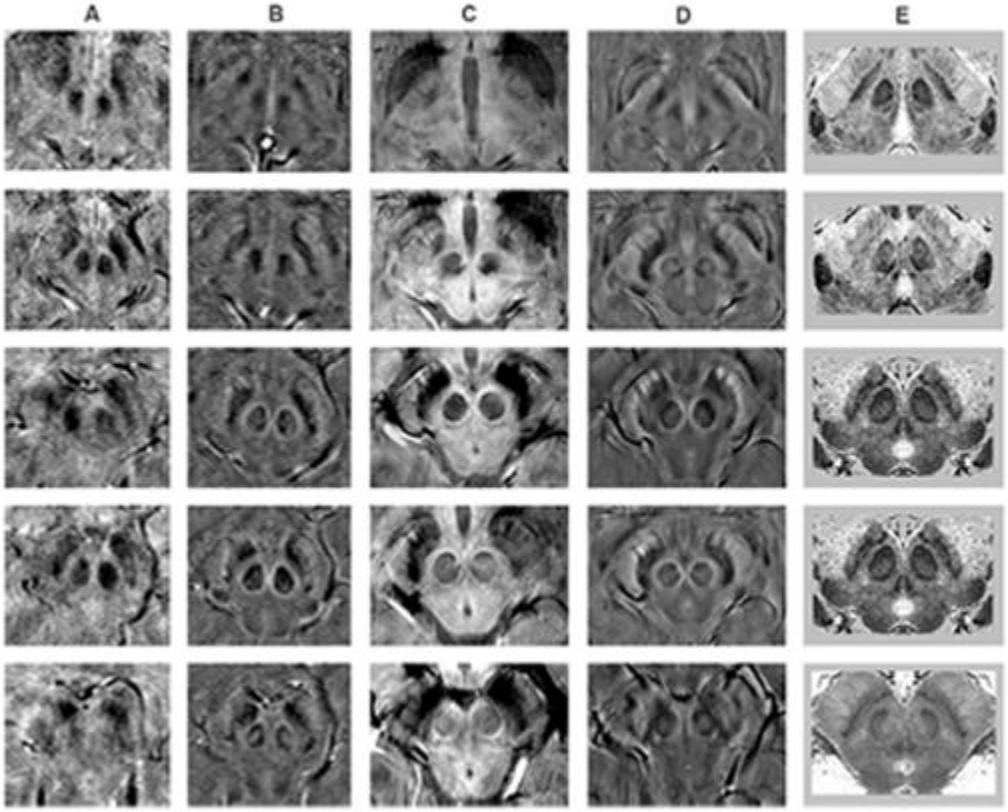

Figure 4.3: A comparison between adjacent slices in SWI magnitude and high-pass filtered phase images at 1.5T and 4T with Duvernoy's India ink-stained results. *A*, Magnitude SWI at 1.5T; *B*, High-pass filtered phase at 1.5T; *C*, Magnitude SWI at 4T; *D*, High-pass filtered phase at 4T; *E*, Duvernoy's results. Only three unique images from Duvernoy are shown here since his slice thickness is 3 mm. The third and fourth images from the top are identical. (Images in column (E) obtained with kind permission of Springer Science and Business Media.)

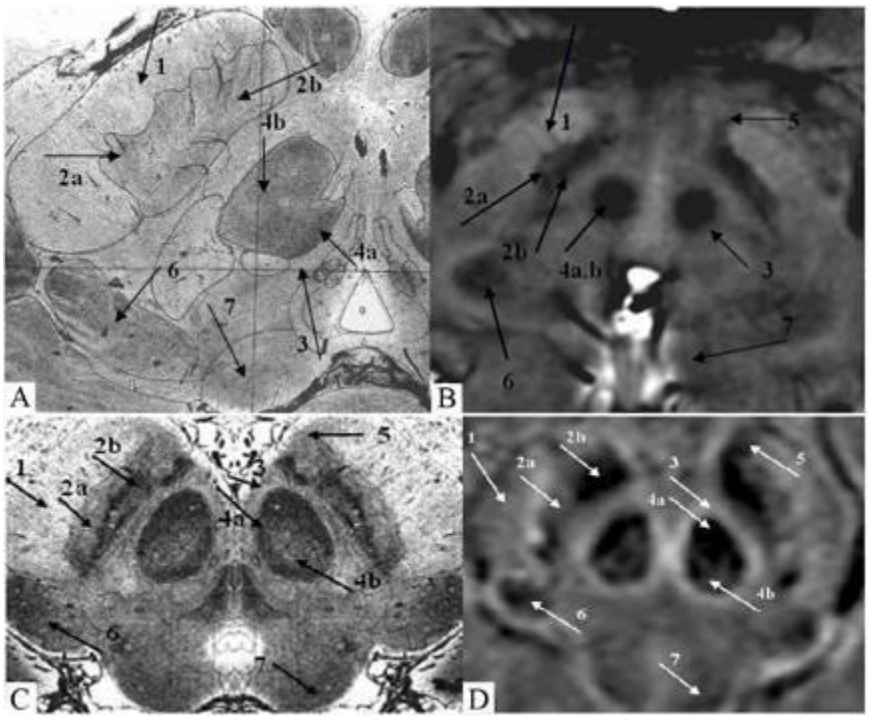

Figure 4.4: A comparison of SWI high-pass filtered phase images (B and D) with Duvernoy's India ink-stained results (A and C). Anterior (A and B) and posterior (C and D) mesencephalic structures are indicated. 1: crus cerebri; 2a: substantia nigra, pars reticulata; 2b: substantia nigra, pars compacta; 3: capsule of the red nucleus; 4a: red nucleus (vascularized region); 4b: red nucleus (non-vascularized region); 5: fascicula nigrale; 6: medial geniculate body; 7: superior colliculus. (Images (A) and (C) obtained with kind permission of Springer Science and Business Media.)

Table 4.1: 1.5T Contrast-to-Noise Ratio (CNR) measurements. The first row for each sequence represents the mean in a given region-of-interest (ROI), while the second row represents the standard deviation (SD) in the same ROI. (No contrast for the given ROIs was observed in the gradient echo T1 data.)

Sequence	Red Nucleus CNR			Substantia Nigra CNR			Medial Geniculate CNR	
	IA/RN	IA/RN capsule	RN/RN capsule	IA/SNc	CC/SNr	SNc/SNr	CMG/LMG	CMG/IA
T2 tse	4.13	—	—	6.19*	4.97*	—	—	—
T2 tse SD	1.23	—	—	1.44*	1.48*	—	—	—
SWI	—	1.43	4.54	5.58	2.84	3.74	1.38	0.45
SWI SD	—	0.73	1.62	0.6	0.75	1.46	1.47	0.35

Table 4.2: 4T Contrast-to-Noise Ratio (CNR) measurements. The first row for each sequence represents the mean in a given region-of-interest (ROI), while the second row represents the standard deviation (SD) in the same ROI. (No contrast for the given ROIs was observed in the gradient echo T1 data.)

Sequence	Red Nucleus CNR			Substantia Nigra CNR			Medial Geniculate CNR	
	IA/RN	IA/RN capsule	RN/RN capsule	IA/SNc	CC/SNr	SNc/SNr	CMG/LMG	CMG/IA
T2 tse	3.36	—	—	4.53*	6.27*	—	—	—
T2 tse SD	0.77	—	—	0.48*	1.64*	—	—	—
SWI	—	1.13	5.85	8.75	5.19	3.56	4.57	1.64
SWI SD	—	1.34	2.23	1.67	1.51	1.08	2.49	0.89

RN: red nucleus; SNc: substantia nigra, pars compacta; SNr: substantia nigra, pars reticulata; IA: intermediate area between RN and SN; CC: crus cerebri; LMG: lateral aspect of the medial geniculate body; CMG: central aspect of medial geniculate body. Empty data boxes show that CNR between certain structures could not be calculated because the structures could not be detected.

* Since SNc and SNr were not seen for T2, CNR is recorded here for IA/SN and CC/SN.

Discussion

Iron plays a key role in many neurological processes. It is of great interest in the study of neurodegenerative disease today and iron remains a topic of high interest in the medical community. SWI offers a way to look at iron content that is different from T1, T2 or T2* maps. The SWI filtered phase images are a sensitive means to not only visualize the presence of iron but also to quantify it (Haacke et al., 2007; Haacke et al., 2005; Ogg et al., 1999). The non-heme forms of iron that are likely seen with MR are ferritin and hemosiderin. Ferritin appears to be seen predominantly in the basal ganglia and primary motor cortex. Gray matter has more ferritin than white matter, although there are indications that ferritin is also present in white matter (Haacke et al., 2007). Iron in transferrin or in glial cells may be non-magnetic and therefore invisible to MR imaging. This may explain why white matter appears to have less iron than gray matter on MRI, while staining reveals the opposite (Haacke et al., 2005).

Based on the data collected at 1.5T and 4T, we can see that highly vascularized areas, like the vascularized region of the red nucleus (as specified in Duvernoy's work), become more prominent or darker on SWI filtered phase images at higher field (figures 4.2, 4.3). Thus, the contrast between the red nucleus and the surrounding brain tissue improves with increasing field strength. In fact, we are able to see the capsule of the red nucleus at 4T in the magnitude images for the first time (figures 4.2H, 4.3C). (SWI filtered phase images can visualize the capsule at 1.5T, but the magnitude images do not). Although the CNR is often large than 4:1 (the CNR needed to be able to visualize clearly one structure from another) this was not always the case. Further, the T2 images had thicker slices and hence their CNR is overestimated by the ratio of their thicknesses compared to the 2mm used in the SWI scans. Further, the CNR at 4T is even

further overestimated by a factor of 1.6 because of the lower resolution of 0.8mm compared to 0.5mm with the SWI scan.

Hypothetically, if we are able to prove that iron causes a reduction in T2 or T2* with increasing magnetic field strength, we would be able to predict that the areas with the higher capillary density would appear darker at high field. An interesting study would be to investigate the relationship between iron and vascular density. E. Sofic (Sofic et al., 1991) and C. M. Morris (Morris et al., 1992) showed that large ferritin deposits are associated with the small blood vessels of the basal ganglia. The strong correspondence of SWI phase and high-field magnitude images with Duvernoy's India ink-stained images (Duvernoy, 1999) and Morris, et al.'s results (Morris et al., 1992) therefore suggests that the non-heme iron visualized in MRI in normal brain is most likely due to ferritin associated with the vascular network. If this hypothesis is verified, these SWI magnitude and filtered phase images may prove to be an important means by which to understand microvascular effects in neurodegenerative diseases.

In conclusion, the high iron content in the red nucleus and substantia nigra leads to a susceptibility change in the tissue that causes a reduction of the phase in these regions in the SWI filtered phase images. This phase change can be used either by itself or to create a magnitude susceptibility weighted image. In either case, this property leads to improved contrast in the mesencephalon using SWI. The improved contrast in the phase images may provide a means by which to monitor changes in the mesencephalon with age or disease state.

Chapter Five

MULTIPLE SCLEROSIS

Chapter overview

Chapter 2 covered the importance of iron in the human body and brain and the potential consequences of free iron deposition being toxic and leading to the development of neurodegenerative diseases. In this chapter, we will present a broad overview of one such disease, multiple sclerosis (MS). The definition of MS, its types as well as its clinical manifestations, will be discussed. The main areas of ongoing research into MS pathogenesis will be emphasized including the immunological, cellular, molecular, neuronal as well as vascular involvement.

Introduction

MS is widely accepted as an autoimmune, inflammatory, demyelinating disease of the central nervous system (CNS) (Noseworthy et al., 2000b). This pathology is recognized as the most common cause of progressive neurologic disability in young adults worldwide. What initiates the disease and the sequence of events underlying the development of MS is not yet well-established (Noseworthy et al., 2000b). However, technological progress as well as the outcomes of successful research has been able to shed some important insights on most factors involved in the pathology of this complex disease. For instance, although there is no precise description or understanding of the nature of this disease, a lot of work has already been done to provide a reasonable clinical, immunological, neurological and vascular understanding of the disease.

Multiple Sclerosis: Clinical Landmarks

5.1 – Different types of MS

5.1.1 Definitions

For a long time, four main clinical phenomena have been recognized as expressed in the course of multiple sclerosis: initial attack, remission, relapse and progression (Confavreux and Vukusic, 2008). Clinically, relapses, also known as exacerbations or attacks, are usually associated with focal inflammation of acute lesions or reactivation of older lesions. These attacks usually end with a remission which can be either partial or complete. The duration of these exacerbations is usually more than 24 hours although 48 hours is the minimum required duration to be considered as attacks (Poser et al., 1983). The emergence of fatigue alone is not enough to be considered a relapse. The fourth phenomenon, progression, is defined as the steady increase in symptoms and signs for more than 6 months (Poser et al., 1983). In other words, progression is the clinical manifestation of chronic, progressive, diffuse degeneration of the CNS.

The occurrence of these relapses and progression defines two distinct phases in the course of MS: the relapsing-remitting (RR) phase, which is characterized by alternating relapses with episodes of clinical inactivity, and the progressive phase which occurs after consecutive relapses and remissions. In some circumstances, steadily progressive course can be reached right from clinical onset. To summarize:

1. *Relapsing-remitting* (RR) MS is characterized by well-defined relapses with full remissions or with some deficits on recovery.

2. *Secondary progressive* (SP) MS starts with a relapsing-remitting disease course and progresses with some chances of minor remissions, occasional relapses and sometimes plateaus.

3. *Primary progressive* (PP) MS is characterized by disease progression from initial clinical onset with some temporary improvements and occasional plateaus.

4. *Progressive-relapsing* (PR) MS is characterized by progressive disease from the beginning of clinical symptoms, with clearly defined relapses, and continuing progression between relapsing periods.

Although it is still under review by MS experts, clinically isolated syndrome is defined for individuals who have a first neurological (monofocal or multifocal) episode lasting 24 hours or more as a result of inflammation in the CNS. Monofocal episode might be limited to an optic neuritis attack, while multifocal episode might reveal weakness on one side in addition to optic neuritis for example. CIS is considered an early sign exhibited by those individuals that might develop one of the MS types mentioned above. However, if caught at that stage, these individuals can be treated early to avoid or delay the onset of clinically definite MS.

5.1.2 Comparison between MS types

At first glance, relapses appear to be the major player in MS pathology. Furthermore, many relapse-related factors are associated with the rapid accumulation of irreversible disability (i.e., an incomplete recovery from the initial neurologic episode, a short interval between the first two episodes, and a high rate of relapses during the first years of the illness (Weinshenker et al., 1991)). Evidence from the PP form of MS indicates that irreversible disability may occur without superimposed relapses. The rate of disability accumulation in these forms of the disease is similar to that seen in the PR form (Cottrell et al., 1999). In general, relapses occur in an unpredictable way, since their frequency varies between individuals as well as within a given individual. Apparently, progression pursues its course independent of individual relapses,

whereas relapses can be superimposed over and above the process of progression. In RRMS, a short-term confirmed increase in disability depends primarily on relapses and is often reversible. To get a better understanding of the difference between MS types, a comparison summary is provided below for the cases where major differences are recognized.

5.1.2.1 Secondary-progressive MS and relapsing-remitting MS

SPMS and RRMS share the same distribution of initial symptoms during the RR phase, the degree of remission from the first relapse, and the period between the onset and the second neurologic episode (Minderhoud et al., 1988). Most RRMS patients eventually become SPMS.

5.1.2.2 Primary-progressive and progressive-relapsing MS

No major differences could be observed clinically and demographically, when comparing these two forms of MS. This holds true for the rates of irreversible progression of PRMS and PPMS. However, PRMS tends to start at earlier age compared to PPMS (median age 37 compared to 41). (Confavreux et al., 1980).

5.1.2.3 Secondary-progressive MS and PPMS

These two types of MS do actually differ. For instance, the clinical manifestation, the onset age and the time it takes to reach a debilitating state are different between SPMS and PPMS (Confavreux and Vukusic, 2006). The latter is more dominant in male subjects (McDonnell and Hawkins, 1998). The former, on the other hand, tends to have a more rapid disability accumulation rate and occurs at a younger age than the latter.

5.2 - MS patients

5.2.1 Age at onset of Multiple Sclerosis

From a percentile perspective, the distribution of patient onset by age is as follows: 10% for 20 years old or younger; 70% between the ages 20 to 40 years old and 20% for subjects 40 years and older. Any onset after the age of 55 years is more likely to be questioned whether this is indeed an MS attack (Confavreux and Vukusic, 2006, 2008). Females often seem to have a slightly younger mean age at onset than males. Furthermore, the female/male ratio is usually found to decrease as age at onset increases.

5.2.2 Genetic and environmental factors

Multiple sclerosis has always been thought to be more common in women and whites (Frohman et al., 2008). Although the former still hold true, newer studies reported that MS is more common in African American females and more threateningly progressive in African Americans in general (Langer-Gould et al., 2013). They believe that this might be related to their vitamin D deficiency due to the darker skin tones. On the other hand, Hispanic and Asian individuals are at lower risk compared to other races. The disease is also common within families with a known history of MS which may be due to the set of immune response genes (built upon the exposure to triggering factors such as viral infections).

5.2.3 Initial symptoms and signs

Initial symptoms in MS (Confavreux and Vukusic, 2006) may be isolated optic neuritis (15%), isolated brainstem dysfunction (10%), isolated dysfunction of long tracts (50%), and various combinations of these symptoms (25%). There was no influence of gender on initial

symptoms. However, an obvious influence of age at onset has consistently been found (Confavreux and Vukusic, 2008).

5.2.4 Initial course

It is estimated that the initial course of MS is RR in 85% of the cases and progressive in 15% (Confavreux et al., 1980). RRMS is more common in female subjects while progressive MS is more prominent in men. Subjects diagnosed with long tract dysfunction (presence of motor, sensory, or sphincteric disturbances) tend to follow the progressive course of the disease. On the other hand, patients diagnosed with optic nerve and brainstem symptoms are mostly diagnosed with RRMS (Confavreux et al., 1980).

5.2.5 Remission

The duration of the ongoing neurologic episode is the key element in the MS prognosis (the probability of improvement) (Kurtzke et al., 1973). Usually, there is a high chance of a second neurologic episode immediately following the initial episode (but not in the cases of optic neuritis), and this probability progressively decreases afterwards. Clinical factors (such as gender and age) may also influence the rate of occurrence of the second neurologic episode in MS, but according to many studies, no clinical factor has had a strong correlation with initial symptoms, degree of recovery from the initial episode, and a RR or SP overall course of the disease (Confavreux et al., 1980). The probability of developing a second episode (although lower) was similar for optic neuritis, spinal cord syndromes, and brainstem-cerebellar symptoms (Tintore et al., 2005). This probability increases with the number of T2 lesions and volume on the MR image (Kappos et al., 2006). On the other hand, juxtacortical, infratentorial and periventricular

lesions do not predict whether a second neurologic episode will take place or not (Barkhof et al., 1997).

5.2.6 Relapse frequency

A huge variation in relapse frequency has been seen in MS patients. In RRMS, the yearly rate is estimated on average to be equal to 0.5 relapses per year. As the disease duration increases, the relapse rate tends to decline overtime. However, this statement has been contradicted by a 3-year longitudinal study which showed that the relapse rate was not influenced by overall disease duration (Goodkin et al., 1989).

5.2.7 Onset of progression

The time to enter the secondary progression phase is estimated to be 19 years on average following an RR onset in MS. However, the time to onset of progression has been shown to be strongly age dependent. For instance, patients diagnosed with RRMS at an older age tend to enter the progressive phase more rapidly (Confavreux et al., 1980; Trojano et al., 1995). Each year, 2% to 3% of the RRMS patients enter secondary progression. This rate is highly associated with gender, initial clinical symptoms, rate of recovery after the initial attack, the time period between the initial and secondary attack, as well as the relapse frequency (Confavreux et al., 1980; Trojano et al., 1995).

5.2.8 MS in children

Although it is rare, onset of MS in children has been reported (Hynson et al., 2001). The ratio of female to male is higher in children (3:1) compared to adult subjects (2:1). A difference

in clinical outcomes is seen between children and adults in the early stages of the disease although a similar pace is seen when the progressive phase is reached. Childhood onset MS patients have been reported to reach the progressive phase at a younger age compared to adult onset MS patients (Renoux et al., 2007).

5.2.9 Survival in MS

After being diagnosed with MS, the median survival for MS patients is 28 years for male and 33 years for females (Bronnum-Hansen et al., 2004). Compared to healthy controls, MS patients tend to live 10 years shorter compared to the age matched healthy controls. In addition, median survival from onset is higher in RRMS compared to PPMS (Grytten Torkildsen et al., 2008).

5.2.10 Living with MS

The person with MS can go through normal life events as all other members in society. This includes natural, accidental and interventional events (such as pregnancy, stress, trauma, infection anesthesia, surgery, and vaccinations). However, these patients are more susceptible to infection, which re-initiates the MS cascade and results in recurring relapses (Confavreux and Vukusic, 2006).

Multiple Sclerosis: Immunological, Cellular, Molecular and Vascular Involvement

5.3 Immunological approach

MS has been diagnosed as a multiphasic disorder, producing clinical attacks at different times in a patient's life, and affecting distinctly different CNS injury targets. Therefore, the

diagnostic criteria have been expanded to increase the sensitivity and specificity of clinical diagnosis (Polman et al., 2005). In the past, MS was only being declared at a time when a patient experienced multiple attacks. Nowadays, patients are classified as having MS when they present a single event that is not explained by an alternative etiology, or when there is evidence of disease seen anatomically using conventional MR imaging criteria. For instance, clinically isolated demyelinating syndrome is most typically associated with clear brain or spinal cord lesions (Frohman et al., 2003). However, there is little debate today that MS is radiographically more active than what is observed clinically over time. The advances in nonconventional MR imaging techniques shows a more global MS pathology and it is believed that MS may not be truly characterized by ‘‘multiple’’ areas of sclerosis, but rather a ‘‘diffuse’’ representation of sclerosis. One of the known landmarks of this disease is the mononuclear cell infiltrates that seem to assemble around post-capillary venules within the CNS. This is facilitated by the upregulation in the expression of adhesion molecules on cerebrovascular endothelium, serving as a scaffolding for the migration of these cells in the brain and spinal cord (Frohman et al., 2006). Once in the CNS, these cells contribute in a complex injury cascade that seems to result in inflammation and theretofore, leading to neurodegeneration. Hence, acute relapses are thought to be related to the development of inflammation within the CNS tract systems (Noseworthy et al., 2000a).

5.3.1 Inflammatory mechanisms underlying tissue injury in multiple sclerosis

In MS, it is believed that there is a major change in many regulatory mechanisms which disable the proper function of the immune system in identifying and neutralizing foreign bodies. In addition, the inability of the immune system to recognize self-epitopes leads to a series of

inflammatory reactions, and hence tissue injury. As such, failure of these mechanisms has been considered as a central hypothesis within the path of autoimmune disorders.

In MS patients, T cells (Treg) are actively primed against myelin antigens (Lovett-Racke et al., 1998). Their presence seems to affect and correlate with the clinical activity and outcome. These pathogenic lymphocytes become resistant to apoptosis, and fail to protect against auto-aggressive responses. Under these circumstances, one would think that the depletion of T cells would be a possible treatment plan to treat MS patients. However, this does not hold true given the importance of these cells in maintaining immune homeostasis (Noseworthy et al., 2000a).

In this section, we will discuss various histopathologic substrates which were unveiled from human MS brain investigations. The fork head box P3 transcription (Foxp3) and protein levels, which is required for the development and maintenance of the T cells compartment, were reported decreased in patients with MS (Fontenot and Rudensky, 2004; Frohman et al., 2006). Another study was conducted investigating the population of regulatory T cells (Brusko et al., 2005). This study showed that the parenchymal CNS infiltrate consisted of B and T cells along with macrophages, with the CD8 T cells being enriched and expanded in MS (Babbe et al., 2000). This study agreed with what is classically reported in RRMS (Crawford et al., 2004). In contrast, the improper function of CD8 regulatory T-cells perturbs the effectiveness of the immune system, inducing a pro-inflammatory state in MS. This was confirmed when restoration of CD8 regulatory T cells worked as an anti-inflammatory mechanism (controlling the excessive T cell response) and decreased clinical symptoms (Karandikar et al., 2002).

Another component of the immune system which seems to be involved in the pathogenesis of MS is the humoral immune response. Evidence of antibody synthesis was identified in the cerebrospinal fluid (CSF) of MS patients which seemed to be compartment-

driven. The presence of these oligoclonal bands in the clinically isolated demyelinating syndrome phase strongly predicts the conversion to clinically definite MS (Villar et al., 2008). Humoral immune responses involve the production of antibodies resulting from a series of complex molecular changes within B cells. Under altered regulatory control mechanisms, the immune system might generate B cell-derived antibodies targeted against infectious epitopes, which can be structurally homologous to self-tissue epitopes, thereby establishing the possibility of cross-reactivity and the development of auto-aggressive immune responses (Levin et al., 2002) and lead to humorally mediated tissue injury in MS. This process has been documented in B cells derived from the cerebrospinal fluid of MS patients (Owens et al., 2003) and has been emphasized by a recent study that showed that a selective monoclonal antibody against a B-cell developmental protein (CD20) led to a reduction in both clinical and imaging measures of disease activity (Hauser et al., 2008).

5.3.2 Epitope spreading

The alteration of the antigenic specificity of immune responses over the course of the disease seems to be relevant to the pathophysiology of MS. These changes take place in the cellular and the humoral levels of the immune response to ensure the recognition and neutralization of infectious agents. However, under pathogenic conditions, these reactions might be targeted against self-antigens, enhancing the reliability of such responses and maintaining the disease activity in the MS patients (Frohman et al., 2008).

5.3.3 Lymphocyte nomenclature and phenotype

The immune system provides surveillance diffusely and compartmentally to the entire body. TH_1 and TH_2 phenotypes play a major role in characterizing the behavior of T cells. TH_1 cells release proinflammatory cytokines (interferon-γ, tumor necrosis factor-β, interleukin (IL) – 12). IL-12 (increase expression) and tumor necrosis factor-β are thought to be associated with MS-related disease activity (Balashov et al., 1997). MS patients show augmented expression of IL-12 when compared with cells derived from control subjects (Comabella et al., 1998). On the other hand, TH_2 phenotype (elaborating IL-4, IL-5, IL-6, and IL-1344) is considered as anti-inflammatory cytokines. TH_{17} cells that produce IL-17, under the influence of IL-23 or IL-6 and transforming growth factor-β, are gaining a great deal of prominence as pathogenic cells in MS and other diseases. ‘‘TH_3’’ cells also seem to be involved in down-regulation of inflammation. Interferons’ anti-inflammatory immune effects have been assessment in many studies (Duda et al., 2000; Steimle et al., 1994). In an MS trial, they used interferon-γ to treat a RRMS and was shown to initiate new attacks through cellular and humoral immune responses (Panitch et al., 1987). On the other hand, treatment with a different interferon-β seems showed reduced disease activity and clinical symptoms (Duda et al., 2000). Nowadays, modulation of other type of T cells are being studied (TH_{17}, IL-17, OL22) which seem to play an important role in the pathogenesis of MS (Polman et al., 2005).

5.4 Cellular approach

Cellular trafficking across different tissues of the body is achieved through molecular interventions, which stabilize the cells and make them ready for migration to specific organs. In MS, and due to the breakdown of the BBB, an expanded number of cells enter the brain and

spinal cord. Part of those cells migrates through the expression of adhesion molecules on the endothelial surface of postcapillary venules. The adhesion molecules on the endothelium, selectins, facilitate the slowing and rolling of the mononuclear cells (lymphocytes and macrophages) on the vessel surface. These cell surface integrin receptors then interact with vascular cell adhesion molecule making the mononuclear cells more stabilized (Noseworthy et al., 2000a). Once attached to the endothelium, metalloproteinases digest fibronectin and basement membrane collagen and creates a channel of passage for the migration of into the brain and spinal cord. Once they reach the CNS, these cells mediate damage through a variety of injury cascades involving cytokines, chemokines, free radicals, superoxides, antibody- and complement-dependent reactions, and changes in ion channels and excitatory amino acid mechanisms (Frohman et al., 2006).

In the pathology of MS, the damage happens in both white matter and gray matter. Therefore, inflammation, degeneration as well as the adaptation to injury response are seen in both areas. The damage occurs as a result excitotoxicity leading to irreversible damage to the axons; hence neurodegeneration. From a cellular trafficking point of view, when demyelination occurs, axons recruit new sodium channels to recover proper function (Stys et al., 1992). The system, therefore, senses an exaggerated amounts of sodium, thereby driving the molecular mechanisms to reduce sodium. All these observations lead to more axonal injury and contributing to the progress of the disease (Frohman et al., 2008).

5.5 Molecular approach

5.5.1 Iron

As we learned from chapter 2, iron is the most abundant metal in the human brain, and plays an important role in many metabolic and functional processes (Stankiewicz et al., 2007). For instance, iron was shown to be a necessity for the synthesis of oligodendrocytes and a key factor in oxygen transport. Ferritin and hemosiderin are considered the two forms of iron storage elements in the cells (Quintana, 2007). Due to the importance of iron in the human body, any iron misregulation and abnormal iron deposition can result in neuronal death (Moos et al., 2007) leading to neurodegenerative diseases such as MS (Abo-Krysha and Rashed, 2008). It has been shown that there is a strong correlation between high iron concentrations (abnormal iron presence) in the brain and neurodegeneration (Ke, 2003). In MS, iron seen in lesions come from myelin or oligodendrocyte residues following demyelination, iron in the macrophages, or a resultant of local microhemorrhages following microvascular wall damage. All these sources have been strongly correlated with MS pathogenesis as mentioned earlier. On the cellular level, new proteins (the stress protein heme oxygenase-1, for example) have been identified as key players in iron metabolism. Although their specific role in the pathogenesis of neurodegenerative diseases is not yet well-established (Ke, 2003), suppressing heme oxygenase-1 protein has been shown to decrease the motor deficits seen in experimental autoimmune encephalomyelitis (EAE) models. Free iron is known to cause the formation of highly reactive hydroxyl radicals that can trigger cell membrane dysfunction and chronic microglial activation (Haacke et al., 2009a). It is believed that, iron in neurodegenerative diseases accumulates through a cyclic inflammatory process during which inflammation attracts iron-rich macrophages, leading to increases in the

local iron content. This iron accumulation leads to further inflammation and iron deposition, causing the system to be self-sustainable (Hammond et al., 2008).

To emphasize iron involvement in MS, several studies suggest abnormal iron deposition in different areas of the brain, such as white matter and gray matter areas (Bakshi et al., 2000; Haacke et al., 2009a; Hammond et al., 2008; LeVine, 1997; Neema et al., 2007). This evidence of iron deposition has been supported by histological studies as well as by animal models such as the EAE. Iron deposition has been typically seen in the neurons and oligodendrocytes (Celius et al., 2000) in the thalamus and the putamen (Drayer et al., 1987) as well as in macrophages and microglia (LeVine, 1997). To summarize, there have been indications (Brass et al., 2006; Tjoa et al., 2005) of correlations between iron deposition, gray matter damage and clinical manifestations of MS, providing evidence of the role of iron in the pathogenesis of MS. This has been shown in many recent studies where they found that abnormal iron in the gray matter structures such as the pulvinar thalamus, the thalamus and the globus pallidus correlates with clinical outcomes, lesion load and brain atrophy (Neema et al., 2009; Zivadinov et al., 2010). This will be more expanded in chapter 7.

5.5.2 Zinc

Many studies suggest zinc level alteration in multiple sclerosis (Cunnane et al., 1989; Dore-Duffy et al., 1983; Ho et al., 1986). One study reported that zinc levels in erythrocytes are significantly elevated (three-fold higher) in patients with MS versus controls but were dramatically decreased during clinically defined attacks (Ho et al., 1986). Zinc level increase may be due to altered levels of cholesterol in plasma and erythrocytes in MS patients (Cunnane et al., 1989). However, in a later study, zinc levels were reported low in the damaged areas of the

CNS in MS (Yasui et al., 1991). These results are in agreement with what we reported in our study (Habib et al., 2010), which is the topic of chapter 6.

5.6 Vascular involvement in MS

Recently, there has been an increased interest in a new theory that MS pathogenesis might have both intracranial and extracranial vascular components. In a study by Zamboni et al. in 2009 (Zamboni et al., 2009), data has shown that venous obstructions are found in MS patients extracranially in one (or more) of the following patterns: severely stenotic jugular or vertebral veins in the neck, a stenotic azygous vein, reduced flow in these veins, malfunctioning valves and/or the presence of septum. These reduced flow effects lead to what has been defined as chronic cerebrospinal venous insufficiency (CCSVI) (Zamboni et al., 2009). More recently, several papers have shown a proclivity of MS patients exhibit these vascular abnormalities compared to normal controls (Feng et al., 2012b). This association of extracranial venous abnormalities with MS is thought to lead to increased stress on the venous system in the brain and to either the development of sclerotic plaques in MS. It has also been considered to be a source of exacerbation of the immunological cascade. However, the direct relationship between venous obstruction, hypertension and inflammation (and hence tissue damage and lesion development), is not yet understood. Intracranially, it has been shown that MS patients demonstrated significant hemodynamic alterations in veins located around the lesions (Zamboni et al., 2007). This study suggests an anatomic relationship between veins and MS inflammatory and degenerated areas. They noted that a venous reflux was found in these areas, causing inflammatory reaction and specifically expression of surface adhesion molecules. They recommended that further investigations should be undertaken, since their study did not compare

patients with and without inflammatory neurological disorders, making their conclusions non-specific (Zamboni et al., 2007).

5.7 Neuronal Involvement in MS

Multiple sclerosis is characterized by the presence of focal demyelinated plaques in the white matter and gray matter of the brain and the spinal cord (Lassmann, 2008). Demyelinated lesions are seen around small veins and venules (as mentioned above) and are believed to exist as a result of an inflammatory process. Demyelination is usually followed by a reactive astrocytic scar formation resulting in axonal injury and loss. On the other hand, remyelination and repair are also seen in MS lesions as newly formed thin myelin sheaths, frequently seen in new lesions. This is a landmark which allows physicians to distinguish between MS and other diseases of CNS. This process seems not to affect white matter only; but also global changes in the gray matter and the normal-appearing white matter (NAWM) have been reported (Filippi et al., 1998). The location of MS lesions in the brain and the spine is heterogeneous. However, there is more tendency for lesions to develop the area of high vascular density (Zamboni et al., 2007) including the periventricular and the subcortical white matter of the forebrain, the optic nerves and chiasm, the cerebellar peduncles and the lateral columns of the spinal cord.

Active MS lesions contain many inflammatory infiltrates (T and B lymphocytes), some plasma cells, and activated macrophages or microglial cells. The debris of the myelin sheaths or of destroyed axons are found within the lysosomes of macrophages. Therefore, the stage of demyelination can be estimated from the molecular composition of these degradation products (Bruck et al., 1995). However, this is not the case in chronic inactive lesions. MR imaging is very sensitive in detecting focal white matter lesions but cannot differentiate between partially

demyelinated and remyelinated lesions given that they can exhibit the same cell density. However, contrast does exist with respect to inactive lesions which show small cell density due to the loss of oligodendrocytes (Lassmann, 2008) and NAWM (oligodendrocytes in the remyelinated lesions may even exceed that seen in the surrounding NAWM).

5.7.1 Axonal injury and widening of the extracellular space

An important feature of MS pathology is the axonal destruction within the plaques. These axonal injuries occur during the active stage of the lesion (Ferguson et al., 1997; Kornek et al., 2000; Trapp et al., 1998). In active lesions, axonal density is reduced by 30%, which is due to true axonal destruction, as well as inflammation and edema. Axonal loss is expressed much more within permanently demyelinated lesions. During the active stage of the lesions, substantial axonal injuries occur, while there is a further accumulation of axonal loss in demyelinated plaques at late stages (Kornek et al., 2000). However, in both stages, axonal injury is associated with inflammation and microglia activation (Ferguson et al., 1997; Kornek et al., 2000). Further, there is an association between demyelination and axonal loss with a widening of the extracellular space. This widening of the extracellular space is reported to be the result of axonal and myelin loss as well as to edema

5.7.2 Focal white matter changes.

At the early stages of the disease, subtle changes preceding inflammation in MS plaques are seen in white matter, which later turn into gadolinium enhanced lesions (Filippi et al., 1998). These changes are thought to be driven by microglial activation. The detection of initial tissue damage is possible given that multiple active lesions develop very rapidly. Afterwards, these

abnormalities exhibits mild inflammation (through lymphocytic inflammatory infiltrates), edema, and microglia activation (as well) in patients with progressive MS (Lassmann, 2008).

5.7.3 Diffuse changes in normal appearing white matter

Diffuse changes in NAWM are commonly seen on MR scans of patients with progressive MS and characterized by diffuse signal abnormalities, reduction of N-acetyl aspartate, or other quantitative MR indices. These landmarks are seen as secondary effects following axonal destruction in focal white matter lesions (De Stefano et al., 1999; Rocca et al., 2003). These alterations consist of some perivascular inflammatory infiltrates, small perivenous demyelinating lesions, and diffuse astroglia and microglia activation (Allen et al., 2001) depending on the stage of MS. For instance, in early stages, these changes represent significant diffusion of myelin density accompanied by mild BBB damage and persistent inflammation in the brain; in patients with primary and secondary progressive MS however, chronic perivascular and parenchymal infiltration of the tissue with T-lymphocytes and profound microglia activation are prominent. Therefore, white matter becomes affected globally and an inflammatory reaction within the brain compartment drives this diffuse white matter damage.

5.7.4 White Matter Lesions Classification

MS is classified as a heterogeneous neurological disease based on its clinical course, pathological mechanisms involved as well as its therapy outcomes. This heterogeneity was also reported in radiological assessments, and validated in *ex vivo* and *in vivo* studies that investigated different types of MS lesions.

The first study examined the immunological and the neurobiological markers of 83 biopsies and autopsies from actively demyelinating lesions (Lucchinetti et al., 2000). This study was able to classify these lesions into 4 categories. Category 1 (pattern I) revealed high activity of T-lymphocytes and macrophages. Category 2 (pattern II) showed the same characteristics of pattern I, in addition to the presence of IgG and complement C9neo at the site of myelin destruction. These two patterns were mainly centered at small veins and have very well defined edges (figure 5.1 A and B). On the other hand, the main difference between these two patterns was the mechanism of myelin injury. Category 3 (pattern III), is similar to pattern I in terms of activities (IgG is absent, but was mainly composed of T lymphocytes with macrophages and activated microglia. However, these lesions were not centered by veins; instead myelin rims were seen around inflamed veins within the demyelinated plaque (figure 5.1 C and D), with some cases revealing Balo-like alternative myelinated and demyelinated tissue. This category is also accompanies with oligodendrocytes dystrophy. Category 4 (pattern VI) was exclusively found in PPMS patients and showed extensive loss of oligodendrocytes and absence of remyelinated shadow plaques suggesting that the function of oligodendrocytes is impaired (figure 5.1 E-H).

Another study examined the magnetic characteristics of the MS lesions using magnetic resonance imaging (Haacke et al., 2009a). This study compared the visualization of MS lesions using different conventional MRI techniques and SWI. While conventional MR techniques evaluate water content in the lesions compared to their surrounding tissue (presence of edema for instance), SWI assessed their iron content, which we have seen throughout this thesis that is abnormally present in MS.

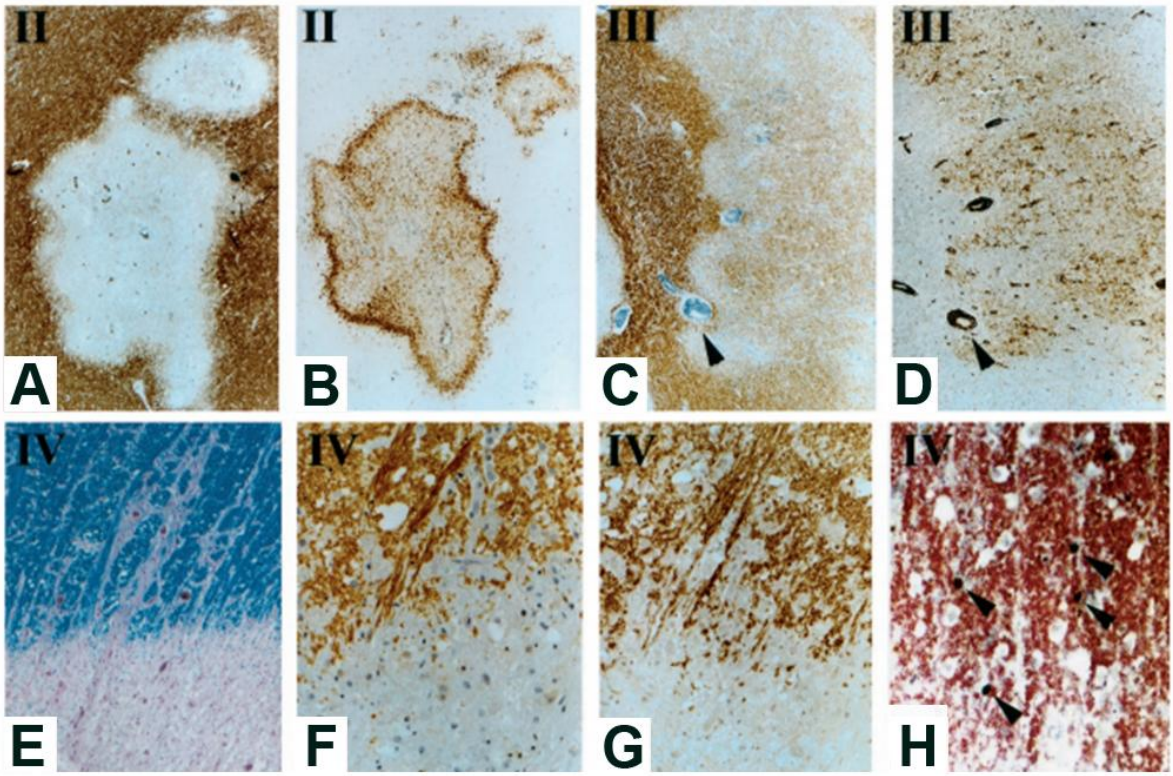

Figure 5.1. A and B. Acute multiple sclerosis; pattern II; perivenous confluent pattern 2 lesion with macrophage rim at active border. (A, myelin oligodendrocyte glycoprotein (MOG); B, CD68). C and D. Acute MS; pattern III; demyelinating lesion with ill-defined borders. The perivenous areas around inflamed vessels show lack of macrophage infiltration and demyelination (arrows). (C, MOG; D, CD68) E-H. Primary progressive MS; pattern IV lesion. Myelin antigens are similarly distributed in the lesions, and DNA fragmentation of oligodendrocytes is seen in the periplaque white matter (H). (E, Luxol fast blue (LFB); F, MOG; G, myelin-associated glycoprotein (MAG); H, double staining of in situ tailing (DNA fragmentation) and cyclic nucleotide phosphodiesterase CNPase [myelin and oligodendrocytes] (Lucchinetti et al., 2000).

This showed that some lesions were seen on both conventional and non conventional methods, while other lesions were seen on only one of these techniques. Lesions seen on SWI were further categorized into six different types (Haacke et al., 2009a): a) uniform dark lesions on phase images representing uniform iron deposition; b) lesions detected on SWI magnitude data only; c) perivenous lesions (similar to pattern I mentioned above) (figure 5.2A); d) hypointense rim surrounding MS lesions (which might reveal iron macrophage activity – similar

to pattern II seen above) (figure 5.2B); e) lesions with a dark central region (similar to pattern III) (figure 5.2C); and f) gray matter lesions (which will be discussed in the next section).

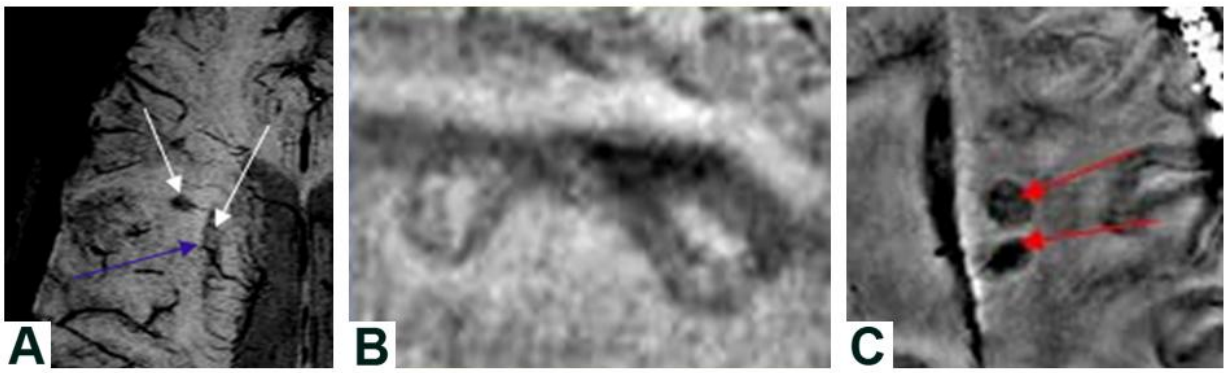

Figure 5.2: Different types of MS lesions seen on SWI images (Haacke et al., 2009a).

5.7.5 Cortical and gray matter pathology

Until recently, MS was regarded as a disease affecting only the white matter. However, a significant number of studies have shown that gray matter, and in particular the cerebral cortex, is affected by demyelination (Lassmann, 2008). This occurs in two different ways: cortical demyelination and diffuse neuronal loss with cortical atrophy.

5.7.6 Cortical demyelination

There are 3 different types of cortical demyelinated lesions: corticosubcortical, perivascular, and subpial cortical lesions. Corticosubcortical lesions result from the expansion of white matter lesions into the cortical tissue (Figure 5.3). Perivascular lesions are identified as small intracortical scars. Subpial lesions are mainly found in patients with progressive disease and are the most abundant in MS (Bo et al., 2003; Kidd et al., 1999). The locations of subpial cortical lesions are mainly in cortical sulci and deeply in the outer surface of the brain. Cortical demyelination are sometimes also seen the cerebellum and the hippocampus. The extent of

cortical demyelination is high in patients with primary or secondary progressive MS and it increases with disease duration. Subpial demyelination appears to be highly MS specific (Kutzelnigg et al., 2005). Corticosubcortical lesions are the only Gd-enhanced lesions compared to other cortical demyelinated lesions. BBB damage in the white matter parts of the lesions may lead to protein extravasation and edema, which may also penetrate into the adjacent cortical areas. Neuronal density is reduced in cortical lesions and in the adjacent normal-appearing cortex (Wegner et al., 2006). In active cortical lesions, neuronal apoptosis and some dystrophic axons are seen (Albert et al., 2007). Remyelination is frequently encountered and more pronounced in cortical MS lesions as in white matter lesions (Albert et al., 2007).

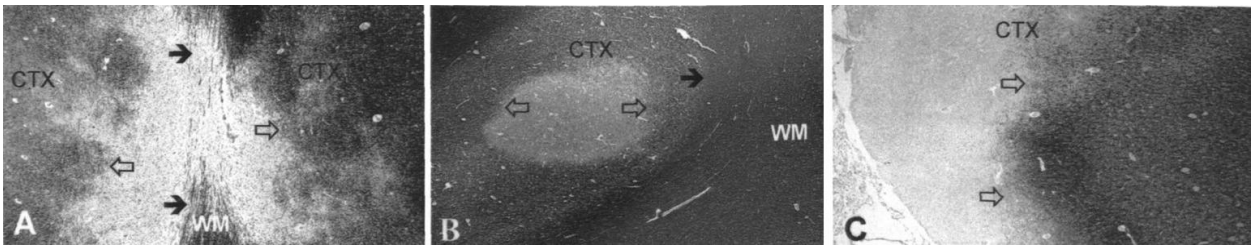

Figure 5.3: The three types of cortical lesions (Bo et al., 2003). a) corticosubcortial lesions; b) perivenous lesions (intracortical scars); c) subpial cortical lesions – CTX: cortex, WM: white matter.

5.7.7 Cortical atrophy

MR imaging studies showed that cortical volume decreases with time in MS patients. Moreover, neuronal and glial cell loss was seen in the demyelinated, but not in the normal cortex. This neuronal loss in the cortex is thought to be directly related to inflammatory tissue damage (Lassmann, 2008).

5.7.8 Remyelination

Myelin repair within the lesions has been noticed in many systematic studies. Remyelination is initiated in the early stages of lesion formation in many cases, but this newly formed myelin may be unstable and subject to subsequent demyelination, i.e. remyelinated lesions can be affected again by new demyelinating attacks (Prineas et al., 1993). Remyelination may lead to complete restoration of myelin within the entire plaque. In early stages of lesional activity, recruitment of new oligodendrocytes takes place and the formation of new thin myelin sheaths becomes more frequent (Prineas et al., 1989). On the other hand, remyelination fails in the later progressive stage of the disease. Extensive remyelination is seen in patients who die at very old ages and with long-standing disease (Patani et al., 2007). Evidently, only when the inflammatory disease process becomes inactive can remyelination become stable and permanent.

5.8 Correlational interpretations

5.8.1 Blood-brain barrier damage and inflammation

Using gadolinium (Gd) based MR techniques makes it possible to assess BBB damage in MS to a certain extent. BBB disturbances were seen in active lesions, in inactive plaques as well as in normal-appearing white matter with different degrees. Leakage of Gd has become a very useful tool to determine the activity of the disease process in clinical setting and therapeutic approaches. Gd enhancement characterizes the newly forming lesions in the brain and spinal cord (Miller et al., 1988). This enhancement of the new forming lesions was seen to be associated with inflammation (Bruck et al., 1997). On the other hand, in the progressive stage of the disease, Gd-enhancing lesions are rare or absent, given that most of the lesions become chronic, and does not correlate with inflammation.

The relationship between BBB disturbances and inflammation is complicated (Hochmeister et al., 2006). Massive BBB disturbances seen in classic active MS plaques is generally associated with intravascular and perivascular inflammatory infiltrates (Hochmeister et al., 2006; Kutzelnigg et al., 2005). Mild disturbance of the BBB, which seems to be below the detection limit of Gd enhancement, is seen in some of the inflamed or not inflamed vessels at this stage. Many vessels, however, show profound leakage of serum proteins and evidence for leaky endothelial cells in the absence of inflammatory infiltrates (He et al., 2005). This has been validated in MS by using a joint Gd - ultra small superparamagnetic particles of iron oxide (USPIO) approach. USPIO helps visualize macrophage activity *in vivo* and Gd reveals any leak in BBB. In animal studies (Dousset et al., 2006) as well as in a human subjects studies (Tourdias et al., 2012), the authors were able to characterize the MS lesions as follows: a) lesions enhanced with Gd and USPIO; b) lesions enhanced with Gd only; and c) lesions enhanced with USPIO only. The authors concluded that what is seen with USPIO is unique and complementary to what is seen with Gd and will better help to reveal myelin injury mechanisms *in vivo*.

5.8.2 BBB damage and active demyelination

Classic active lesions are infiltrated by macrophages that contain myelin degradation products in different stages of digestion (Bruck et al., 1995). Active plaques have a peripheral rim of ongoing myelin destruction that show dense inflammatory infiltrates and a broad rim of activated macrophages. Thus, there is no correspondence between the absence of Gd-enhancement on MR imaging scans and lesions that are inactive in terms of inflammation (mentioned previously), ongoing demyelination, or tissue injury.

The prognosis of Multiple Sclerosis

MS is characterized by a steady and stable rate of accumulation of neurologic abnormalities that can be observed at an individual level. What differs among patients is the individual slope of the neurologic deterioration. Several factors usually affect the prognosis. For instance, older age at onset, dysfunction of long tract-related initial symptoms, progressive initial course, and male gender are associated with a worse outcome, whereas the combination of younger age at onset, optic neuritis as initial symptom, RR initial course, and female gender is associated with a better prognosis. The initial course of MS is the most influential factor in the prognosis. The second most important factor in prognosis is age at onset. Initial symptoms and gender have a very small effect compared to initial course and age at onset. Abnormalities in the baseline brain MR image have a predictive value as well. MR imaging findings are predictive for the development of MS and T2 lesion volume and its changes at earlier time points are predictive of later disability. For example, the rate of increase in the T2 lesion volume has been seen to be three times higher in those who converted to SPMS than in those who remained in the RR stage at follow-up. The search for other paraclinical factors that could be predictive of the outcome has not been promising so far. For instance, the presence of the HLA-DR15 allele does not significantly correlate with the course and severity of the disease (Celius et al., 2000; Runmarker et al., 1994). Moreover, the issue of the presence of apolipoprotein E alleles is still inconclusive. According to several large series of patients with MS, the epsilon 4 allele is associated with a rapid accumulation of disability (Chapman et al., 2001) and an accelerated evolution of brain MR imaging abnormalities (Fazekas et al., 2000). Currently, only MR imaging can provide useful information for clinical evaluation.

To conclude, the following are important findings in the prognosis of MS. First, the predictive factors of the disability accumulation in MS are essentially the same as those that are predictive of SPMS, which is not really surprising. Second, two phenomena seem to be operating: a weak interplay between relapses and prognosis contrasting with a strong interplay between age and prognosis.

In the next 3 chapters, we will focus on two of the previously mentioned aspects: assessing the molecular component (specifically iron) using magnetic resonance imaging and X-ray fluorescence and its correlation with the vascular component (by investigating a probable vascular model of MS).

Chapter Six

VISUALIZING IRON DEPOSITION IN MULTIPLE SCLEROSIS CADAVER BRAINS

Introduction

For decades, multiple sclerosis (MS) has been understood as an inflammatory demyelinating and neurodegenerative disease of the central nervous system (CNS) (Noseworthy et al., 2000b). The risk factors for and sequence of events triggering MS are poorly understood (Bielekova and Martin, 2004). Until recently, the focus of research into this complex disease has been on immunological (Frohman et al., 2008; Prineas et al., 2001), neurological (Allen et al., 2001; Filippi and Rocca, 2009; Sharma et al., 2006; van Waesberghe et al., 1999), cellular (Connor and Menzies, 1995) and molecular (Dore-Duffy et al., 1983; Forge et al., 1998; Grant et al., 2003; Ho et al., 1986; Stankiewicz et al., 2007; Walton and Kaufmann, 1984; Zamboni, 2006) events. A few early studies suggested that vascular anomalies may lead to MS (Adams, 1988; Fog, 1964; Schelling, 1986) and this hypothesis is now being reexamined by Zamboni and others (Adhya et al., 2006; Ge et al., 2005; Ge et al., 2009; Inglese et al., 2007; Law et al., 2004; Rashid et al., 2004; Singh and Zamboni, 2009; Zamboni, 2006; Zamboni et al., 2009; Zamboni et al., 2007). Zamboni refers to the resulting vascular effects on the brain as "chronic cerebrospinal venous insufficiency" or CCSVI (Zamboni et al., 2009) that leads to iron deposition in the vessel walls (Zamboni, 2006), in the venous drainage system (Haacke et al., 2010b) and in and around MS lesions (Haacke et al., 2009a). MRI studies using susceptibility weighted imaging (SWI) have shown that many patients have iron overload in at least one of the structures of the basal ganglia (Haacke et al., 2010b). A new extension to SWI called susceptibility mapping or SWIM (for short) will make it possible to better quantify iron content without the phase artifacts present in SWI. Both SWI and SWIM could be powerful tools to detect and quantify perivascular iron *in*

vivo (Haacke et al., 2007). Other MR techniques have been used for iron quantification *in vivo* (such as T2 and phase based-sequences) (Bakshi et al., 2002; Haacke et al., 2007; Xu et al., 2008) and *ex vivo* (such as synchrotron X-ray fluorescence (Gh Popescu et al., 2009; Popescu et al., 2009a; Popescu et al., 2009b) and histological staining (Hallgren and Sourander, 1958). Recently, rapid-scanning X-ray fluorescence (Popescu et al., 2009a; Popescu et al., 2009b) (RS-XRF) has been used to simultaneously and quantitatively map iron, copper and zinc in single slices of whole human brain (Popescu et al., 2009b). In this study, SWI and RS-XRF were used in parallel on the same brain slices to evaluate SWI as a tool to image iron in MS.

Materials And methods

Samples: Two formalin fixed MS cadaver brains were obtained from the Human Brain and Spinal Fluid Resource Center (HSB), Los Angeles, CA under University of Saskatchewan ethics approval (BioReb 06-250). We will refer to these two MS brains as MS1 and MS2. MS1 (HSB # 3816) is a coronal section from a 47 year old female who was clinically diagnosed with multiple sclerosis and the gross and microscopic description provided in the HSB neuropathology were consistent with chronic active MS plaque formation. The post mortem interval for this brain was 20.7 hours. There was extensive irregular demyelinating peri-ventricular plaque formation throughout the extent of the body of the right and the left lateral ventricles with satellite extension into the respective corona radiata and the left basal ganglia (figure 6.1 - upper). There was prominent macrophage activity and perivascular lymphocytic cuffing. MS2 (HSB# 3867) (figure 6.1 – lower) is a coronal section from a 75 year old male, diagnosed with MS who died of a heart attack. The postmortem interval for this brain was 12.9 hours. The gross neuropathology report was consistent with chronic MS plaque formation with

mild atherosclerosis involving the basilar cerebral vasculature. Moreover, microscopic study showed prominent decrease in oligodendrocyte density but no macrophage activity or perivascular lymphocytic cuffing.

Magnetic Resonance Imaging: MR images were collected at the MR Research Facility, (Wayne State University, Detroit, MI, USA) on a 3T Siemens Verio system using a gradient echo based SWI sequence ($\alpha = 15^{o}$, TE = 20 ms, TR = 35 ms) and a T2 weighted Fluid Attenuated Inversion Recovery (FLAIR) sequence. For SWI, images were acquired with 0.5 mm resolution in the phase and readout directions, and 1 mm in the slice direction with a bandwidth (BW) of 120 Hz/pixel, a field-of-view (FOV) of 256mm x 192mm and displayed on a 512 x 384 matrix. The parameters for FLAIR sequence acquisition were as follows: ($\alpha = 150^{o}$, TE = 74 ms, TR = 9000 ms, with 1 mm^3 resolution, BW = 250 Hz/pixel and FOV of 256x192).

MR phase images were post-processed using high pass filtering with a central 64 x 64 matrix (Haacke et al., 2009b) zero-filling to create the SWI filtered phase images. These were used as input into the SWIM algorithm to create quantitative susceptibility maps using SPIN software (Signal Processing in NMR, Detroit, MI, USA). The background gelatin fill was confirmed to have zero phase (2048 phase units). The SWIM post processing technique is used to map out the susceptibility difference between structures.

Magnetic susceptibility is a quantitative measure of a material's tendency to interact with or distort an applied magnetic field. The volume susceptibility of iron measured in this paper is affected by the spin status (for example Fe^{3+}), the type of molecule, the number of iron atoms in the molecule, the molecular weight, the concentration of molecule in the volume, tissue density and others. In pathological cases, many factors are not known yet. Thus, the exact relationship

between susceptibility and iron concentration varies in different structures and pathologies, and is still under investigation. In this paper, we have included the iron concentration (μg/cm^2) as measured by XRF.

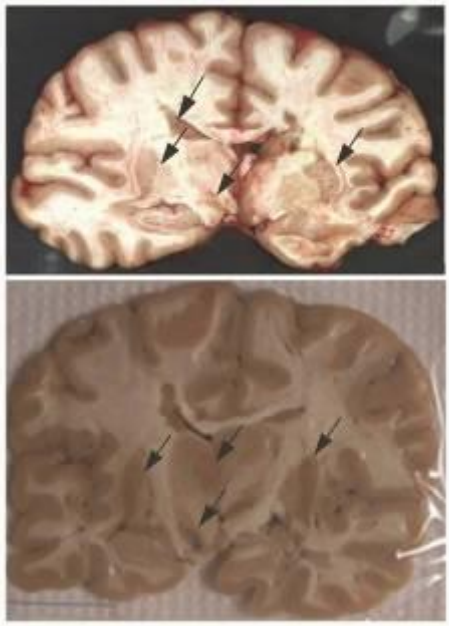

Figure 6.1. Optical images of the two MS brains. Upper: MS1, Lower: MS2. Black arrows point to visualized iron deposition.

X-Ray Fluorescence: RS-XRF imaging was performed at wiggler beam line 10-2 at the Stanford Synchrotron Radiation Lightsource (SSRL). The incident beam was set at 12 keV and was vertically collimated onto a Si (111) monochromator. The incident beam intensity was monitored using a nitrogen-filled ion chamber upstream of a tantalum aperture. This aperture produced a 100 μm x 100 μm spot on the sample with the approximate escape depth of 310 μm. The samples were mounted on a set of motorized stages oriented at 45° to the incident beam to minimize scatter, and raster scanned in the beam with a dwell time of 35 ms/point. A single element silicon drift detector was placed at 90° to the incident beam. Energy windows were

centered ([8.380 - 8,980] Kev for Zn and [6.210 - 6.700] Kev for Fe) to collect fluorescence counts from the emission lines of Fe Kα1 and Kα2 emission lines averaged at a mean Kα energy of (2E×Kα1 + E×Kα2)/3, all other biologically interesting elements, scatter and total incoming counts. Data were normalized against incident energy (I0).

The data were quantified using XRF standard foils (Micromatters Inc.) using Sam's Microanalysis kit (http://ssrl.slac.stanford.edu/~swebb/smak.html) with the output units of 'μg $Fe/cm^{2'}$

RESULTS

MS case 1: Iron, as identified by XRF (figure 6.2a) matches well visually with the SWI-phase image (figure 6.2d). The maximum levels of iron from the different structures was quantified and ranged from a low value of 2.08μg/cm^2 (in white matter) to a highest concentration of 62.56μg/cm^2 next to the vein draining the caudate on the left side of the brain (figure 6.2b).

Iron values near vessels in the globus pallidus and on the left side were about 62.56μg/cm^2 (figure 6.2b). The overall amount of iron in the basal ganglia on the right side seemed lower but this may be due to a slight difference in the section plane. However, the thalamus on the right side has more iron than its corresponding structure in the other hemisphere.

Because myelin is rich in zinc, demyelinated regions show very low zinc. These regions (figure 6.2e (black arrows)) correlate well with plaques visible with fluid attenuated inversion recovery (FLAIR) (figure 6.2f (white arrows)). Iron is slightly elevated at the periphery of several demyelinated plaques.

MS case 2: XRF measured iron in the white matter and gray matter, specifically in the deep gray matter structures (thalamus (figure 6.3a) and basal ganglia (figure 6.3a and b)) of this case is similar to those in case 1 (figure 6.2a,b) ranging from 2.21 to 17.52 μg/cm^2.

MS case 2 shows abundant iron in the basal ganglia that appears to be normal. Iron in the basal ganglia in both hemispheres matches well between the XRF and SWI-phase image (figure 6.3a, c and d). We did not detect any large perivascular iron deposition similar to that seen in MS case 1 but halos of iron and zinc decrease were seen at the periphery of and in some demyelinated plaques (figure 6.3c, d, e and f).

Given the increased interest in CCSVI as a risk factor for MS, we sought to determine if SWI might be an effective means to visualize iron deposits in MS brain by using a parallel imaging strategy in which the presence of iron was independently confirmed using element-specific XRF mapping. The advantage that SWI has is that it can be run on patients to monitor iron content. It remains to be determined if phase as seen with SWI is in fact directly related to iron content and not coming from other elements. SWI has also been shown to reveal MS lesions that were not visualized with conventional T2 weighted imaging. This iron content can be either from heme or non-heme (such as ferritin or hemosiderin) sources.

DISCUSSION

Single echo and multi-echo SWI sequences were acquired in this study. Multi-echo SWI data were processed to calculate T2* maps which have been used to correlate with iron content in the past. However, the T2* maps in this cadaver brain study did not appear to correlate with iron content. This could be because of the confounding effect of local water content which causes an increase in T2* counter-balancing the decrease in T2* caused by the presence of iron.

Confounding effect of local water content was also seen in some but not all MS lesions detected using FLAIR images, where high signals were visualized in corresponding high iron content regions on XRF images.

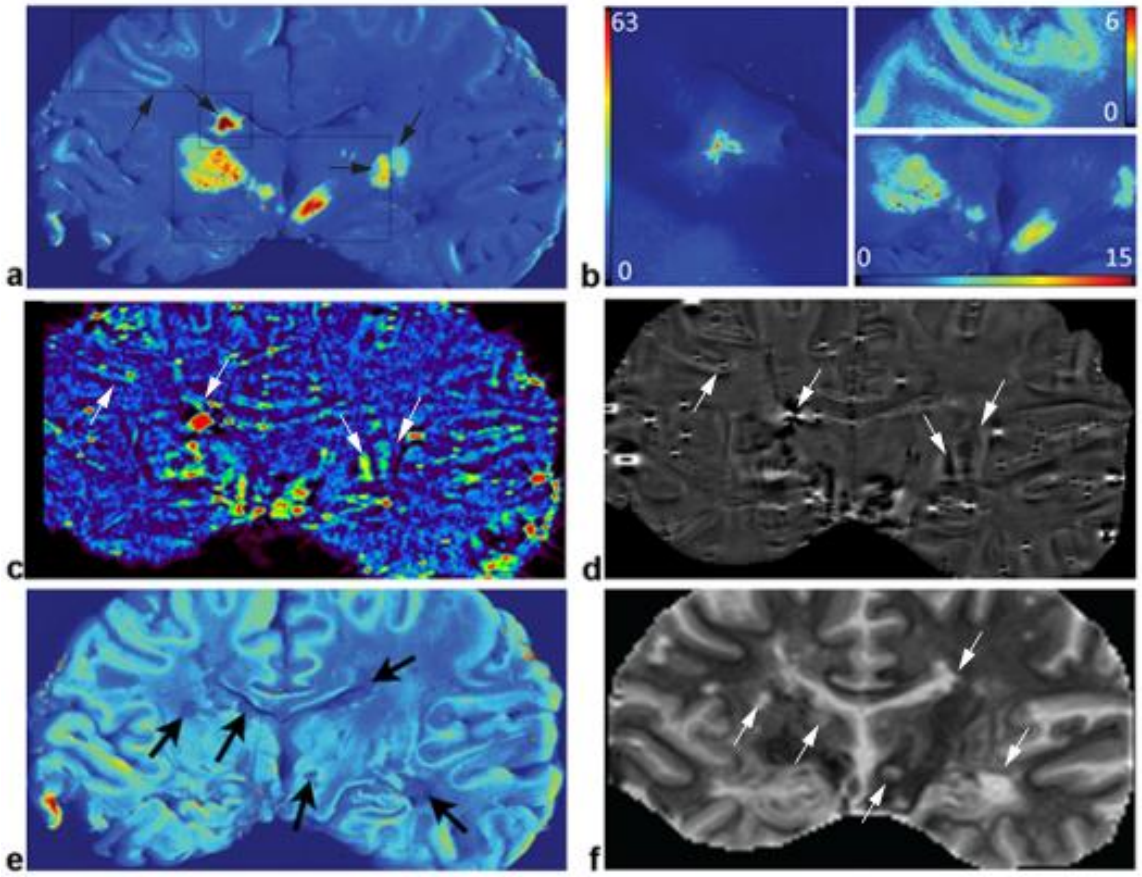

Figure 6.2: Comparison between different acquired MRI sequences showing MS lesions, iron and zinc deposition in MS1: a. XRF Fe map; b. Magnification of selected regions in (a), unit µg/cm2; c. Fe susceptibility mapping; d. SWI phase; e. XRF Zn map, f. FLAIR

In summary, these preliminary results show a good correlation with iron as seen with SWI and SWIM and that seen with RS-XRF. High iron content often correlated with low zinc content as might be expected when there is a depletion of oligodendrocytes. Future work in this

direction should include the creation of a one-to-one quantitative mapping of RS-XRF data with SWIM data. This would make the *in vivo* use of SWI more available as a quantitative methodology to map iron for patients with multiple sclerosis.

Chapter Seven

ASSESSING IRON CONTENT IN THE DEEP GRAY MATTER OF MS PATIENTS AND HEALTHY CONTROLS

Introduction

Multiple Sclerosis (MS) has been considered as both an autoimmune inflammatory demyelinating disease (Lassmann et al., 2007) and a disease where venous involvement is recognized as a possible biomarker or representing some specific damage to the tissue (Schelling, 1986). Recently, the inter-relationship between venous abnormalities, obstructed flow and a possible role for iron in tissue damage has been considered (Singh and Zamboni, 2009; Zamboni et al., 2009).

To a large degree, but not exclusively, the imaging pathogenic landmarks of MS have been well documented mostly in white matter (WM) (Filippi et al., 1998; Haacke et al., 2009a). To a lesser degree, investigators have noticed abnormalities in cortical regions as well, specifically near the gray matter (GM)/WM boundary and in gray matter as well (Haacke et al., 2009a; Nelson et al., 2007). However, determining whether the starting point is in the GM or WM is still unclear (Allen et al., 2001; Neema et al., 2009; Nelson et al., 2007). Currently, there is an increased interest in studying how GM is affected (Filippi and Rocca, 2009; Haacke et al., 2009a; Varga et al., 2009) and particularly deep GM involvement in MS where iron deposition has been observed (Adams, 1988; Eissa et al., 2009; Haacke et al., 2009a). Brain iron accumulation in neurodegenerative diseases, including MS, is not new and has been shown histologically in the past (Craelius et al., 1982; Levine and Chakrabarty, 2004). In MS, its source is likely due to myelin or oligodendrocyte debris, concentrated iron in the macrophages, or as a product of local microhemorrhages following venule wall damage (Adams, 1988; Haacke et al., 2009a). As the wall breaks down, free iron may escape outside the vessel. This process has

typically been seen in the basal ganglia, neurons, oligodendrocytes, macrophages and microglia (Haacke et al., 2009a). Generally, free iron is known to lead to the formation of highly reactive hydroxyl radicals that can trigger cell membrane dysfunction (Gutteridge, 1992) and chronic microglial activation (Lassmann et al., 2007). Thus, iron from any of the above mentioned sources could lead to inflammation, and a further buildup of iron, causing the system to be self-sustainable (Hammond et al., 2008). When iron is present, the result is a hypointense signal on T2 or T2* weighted images and a change in the phase for susceptibility weighted imaging (SWI) (Haacke et al., 2010a; Neema et al., 2009; Zivadinov et al., 2010) which makes it possible to quantify iron changes *in vivo*. Different results have been reported in studying iron involvement in MS. The variations seen in these results have been related to many factors including the type of MS studied, the sample size recruited and the methodologies used to assess iron deposition. From these studies, a number of papers have now shown that there are increases in iron in the basal ganglia and the thalamus (Haacke et al., 2010a; Hammond et al., 2008; Zivadinov et al., 2010). In a recent study (Zivadinov et al., 2010), high iron was found in the pulvinar thalamus, the thalamus and globus pallidus and they considered the iron measured by SWI to be a strong indicator of disability progression, lesion volume accumulation and atrophy. Another study by Burgetova et al (Burgetova et al., 2010) using T2 relaxometry showed that iron does increase in the basal ganglia and the thalamus of MS patients but showed an inverse correlation with lesion load. Zhang et al. (Zhang et al., 2010) also reported a correlation between T2 hypointensities (representing iron deposition) and the patients' disabilities of the relapsing remitting MS group they studied. Ceccarelli et al (Ceccarelli et al., 2010) investigated deep GM T2 hypointensity in clinically isolated syndrome (CIS) MS patients and showed that iron related changes and neurodegeneration can both occur in the early stages of MS. Recent work investigated the

potential role extravasated iron might play by studying CSF ferritin levels, which is considered an indirect measure of iron in the brain (Worthington et al., 2010). They found no difference between the MS population and the control group. Another study (van Toorn et al., 2010) noted that iron deficiency was reported in their MS group studied and iron supplementation was prescribed to these people. Evidently, this treatment resulted in a partial recovery of their symptoms. Thus, the role of iron in MS and its correlation with the clinical outcomes is still unclear and new approaches to investigate brain iron in MS patients are still needed. In this multidisciplinary work, we study a group of 52 MS patients using SWI, which is a powerful MR methodology known to be sensitive to iron. We also present a new weighting scheme to evaluate iron abnormalities and better differentiate between what is considered normal and abnormal iron deposition.

Materials and Methods

Data Acquisition

Fifty-two (52) clinically definite MS patients were imaged (mean age: 43, standard deviation: 11.73, range: 17 to 66 years) under four separate Internal Review Board approved protocols. One hundred and twenty-two (122) normal subjects (mean age: 44, standard deviation: 13.49, range: 20 to 69 years) were included in this study to establish a normal range of iron deposition in the structures of interest. The patient population studied covered 2 types of MS including RRMS (31) and SPMS patients (21) (RRMS mean expanded disability status scale (EDSS): 2.19, EDSS range: 1 to 5.5, mean disease duration: 8 years ; SPMS mean EDSS: 5.92, EDSS range: 3 to 7.5, mean disease duration: 19 years). All patients and controls consented to be

subjects in this study. A velocity compensated, 3D gradient echo sequence was used to generate SWI images.

Site 1: Twelve (12) MS patients were recruited at the Detroit Medical Center, Detroit, MI, USA for this study. SWI data were acquired on a 1.5T Sonata scanner (Siemens Medical Solutions, Erlangen, Germany) equipped with an 8-channel head coil. Imaging parameters for SWI were: repetition time (TR) = 57ms, echo time (TE) = 40ms; flip angle (FA) = 20°, bandwidth (BW) = 80 Hz/pixel, Field of View (FOV) = 256x192 mm^2 , matrix size 512x448), with a resolution of 0.5x0.5x2mm^3.

Site 2: Thirty-one (31) MS patients and 18 normal subjects were scanned on a 3T GE Signa Excite HD 12.0 Twin Speed 8-channel scanner (General Electric, Milwaukee, WI, USA) at the University of Buffalo, Buffalo, NY, USA. A multi-channel head and neck coil was used to acquire the SWI data. The imaging parameters were: TR=40ms, TE=22ms, FA=12°, and FOV=256x192mm^2 (512x256 matrix with PhaseFOV = 0.75) and image resolution of 0.5x1x2mm^3.

Site 3: Nine (9) MS patients were scanned using a 3T Siemens TIM Trio system (Siemens Medical Solutions, Erlangen, Germany) at Jena University Hospital, Jena, Germany. A 12-channel receive head-matrix coil was used to acquire the SWI data. The imaging parameters were: TR=29ms, TE=20ms; FA=15°, BW=120 Hz/pixel, FOV= 256 x 192 mm^2, matrix 512x256 with FoV Phase=0.75, corresponding to an image resolution of 0.5x1x2mm^3, iPAT = 2 (24 reference lines), 128 partitions.

Site 4: The SWI data of another 104 normal subjects (previously studied (Haacke et al., 2010c)) were added to the 18 normal cases studied in site 2 to create a baseline for iron content in the deep grey matter nuclei of healthy subjects as a function of age.

The ability to use and compare data from different sites, acquired at different field strengths, lies behind the concept that the phase values will remain constant if the product of field strength to the echo time is kept constant and is otherwise independent of field strength or system manufacturer (Haacke et al., 2009b). Thus, no matter what field strength is used, evaluating iron content using phase images should report consistent results. To experimentally test this concept, we recruited 36 normal controls from site 1, 2 and 3 who were scanned using the parameters specific to each site and analyzed their data. The results were compared to the 104 normal cases from site 4 and indeed showed that these measured values (from site 1, 2 and 3) lay within the normal range deduced from site 4 data.

Data Analysis

A 64x64 (or equivalent) low spatial frequency kernel matrix was used to complex-divide the original *k*-space data to create an effective high pass filtered phase image (Haacke et al., 2009b). The resulting SWI filtered phase images were used as a means to quantify iron content. The following seven deep gray matter structures were studied for iron content (methodology described in previous studies (Haacke et al., 2010a; Haacke et al., 2010c; Zivadinov et al., 2010)) including: the globus pallidus (GP), the head of the caudate nucleus (CN), the putamen (PUT), the thalamus (THA), the substantia nigra (SN), the red nucleus (RN) and the pulvinar thalamus (PT).

Our in-house software SPIN (Signal Processing in NMR, MRI Institute for Biomedical Research, Detroit, MI, USA) was used for the data analysis. Each structure was separated into two regions-of-interest: the normal iron content region (RI) and the high iron content region (RII). Since our interest was to quantify high iron content, our main focus was on RII and the

total region (RI+RII). To achieve this quantification, we used the same process described in more detail in Haacke et al. (Haacke et al., 2010c). To separate these two regions automatically, thresholds were based on the data from recent papers (Haacke et al., 2007; Miao, 2008). For the structures that were not included in these papers (pulvinar thalamus and thalamus), appropriate thresholds were calculated by analyzing twenty normal cases with ages ranging from 20 to 39 years old. Otherwise, the thresholds were set using the mean value measured minus two times the standard deviation (SD) across an elderly population to be on the conservative side as outlined in Haacke et al (Haacke et al., 2007) and across the above mentioned 20 normal cases. The boundary of each structure was drawn manually by three well trained graduate students and the high iron content region was found automatically by using threshold values. The intra-class correlation coefficient reliability (ICC) was evaluated by comparing the results of 5 different subjects from 3 different observers using Statistical Package for Social Sciences (SPSS) software. All three observers evaluated the same structure's average iron content in RII, the normalized area and the total iron in the putamen. The ICC values for these measures were 0.71, 0.93 and 0.81, respectively. SPIN can output the statistical measures of the total structure and the high iron content region for later analysis. Different measures have been evaluated (Haacke et al., 2010c; Zivadinov et al., 2010): 1) the fraction of the structure that had high iron content (percentage area), 2) the average putative iron per voxel in RII and 3) the total putative iron content in the high iron content region. The main criterion to differentiate normal from abnormal is that the measured iron content should lay outside the 95% prediction interval lines of the normal population. Moreover, iron deposition measures were weighted according to their spread around the mean values. This abnormality weighting AW (m) was achieved by substracting the measured mean value (MV) from the estimated values of normal iron deposition of age matched

controls MV_n (calculated from the linear regression) , then subtracting m times the estimated standard deviation (SD_n) (m=2 while considering a 95% confidence interval) and dividing the results by SD_n (equation 7.1).

$$AW(m) = ((MV - MV_n) - mSD_n)/ SD_n \quad (7.1)$$

In this paper, the results will be shown for both m=2 and m = 3.

Results

The main purpose of this study was to quantify iron content in the basal ganglia and thalamus of MS patients using phase information acquired from SWI data, and create a new weighting scheme that allows us to better differentiate between normal and abnormal iron deposition in MS patients compared to control subjects. Iron overload was well visualized in MS patients in a number of regions related to the basal ganglia and thalamus. Figure 7.1 displays the iron content visualized in an age matched control (age 39) and an MS patient (age 40) in the basal ganglia and midbrain using SWI. Note that both have iron content in the red nucleus and substantia nigra, however, iron overload was only seen in the MS case. High iron deposition can be seen in the CN, GP, PUT and PT of this MS patient. In the normal subject, iron deposition in these brain structures is much less and is evenly distributed.

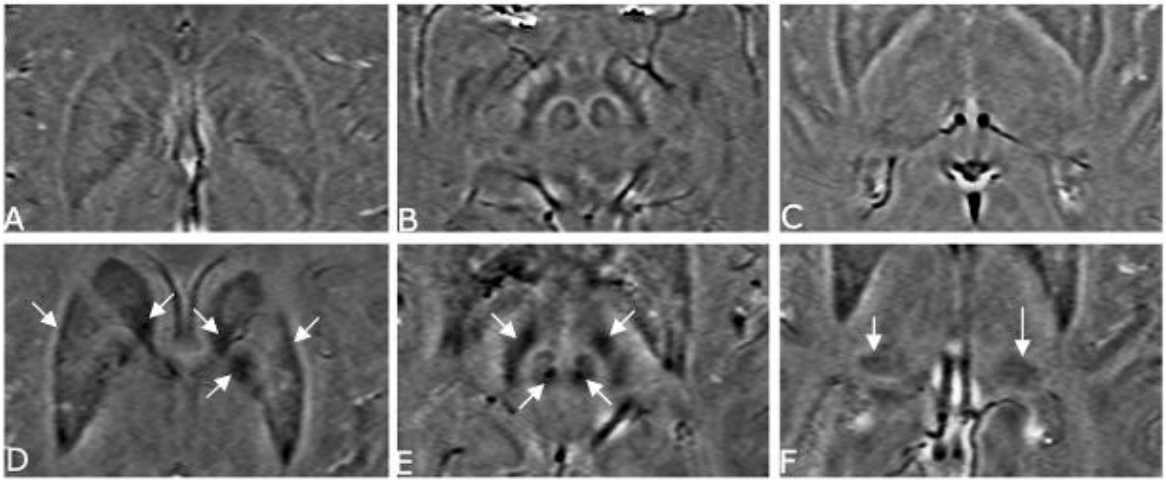

Figure 7.1. SWI filtered phase images displaying the basal ganglia and the midbrain of an age-matched normal control (A, B, C) and MS patient (D, E, F) showing abnormal iron deposition in the globus pallidus, putamen and the caudate nucleus (D); the substantia nigra and the red nucleus of the midbrain (E); and the pulvinar thalamus (F).

Abnormal iron changes were seen upon visual examination in Figure 7.1, with the quantified results appearing in Figure 7.2. Generally, the degree of abnormal iron accumulation varied depending upon whether one measures total iron in RII, average iron in RII or the normalized percentage area of RII. In Figure 7.2, we display these three measurements for the CN and PT as an example to show the abnormal iron content of MS patients relative to normal subjects.

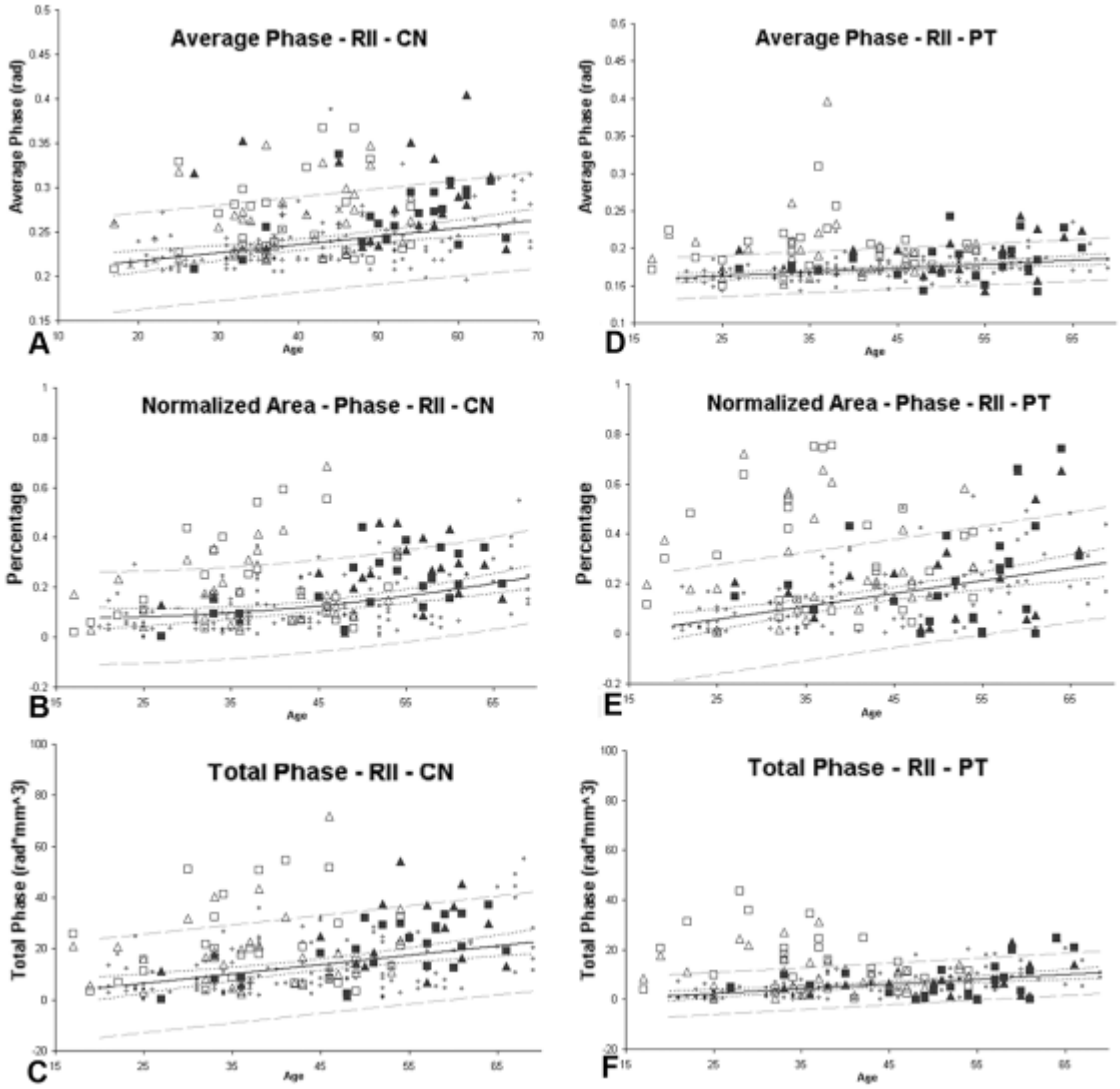

Figure 7.2. Average phase, normalized area and total phase of RII in CN and PT. Small dots represent normal subjects. The solid line is the regression line and the outer dashed lines represent the 95% prediction interval of the regression. Hollow squares and triangles represent relapsing remitting MS patients and the solid squares and triangles represent secondary progressive MS patients. The squares and triangles represent the left and right hemisphere. Many of the MS patients have brain iron content beyond the 95% prediction intervals.

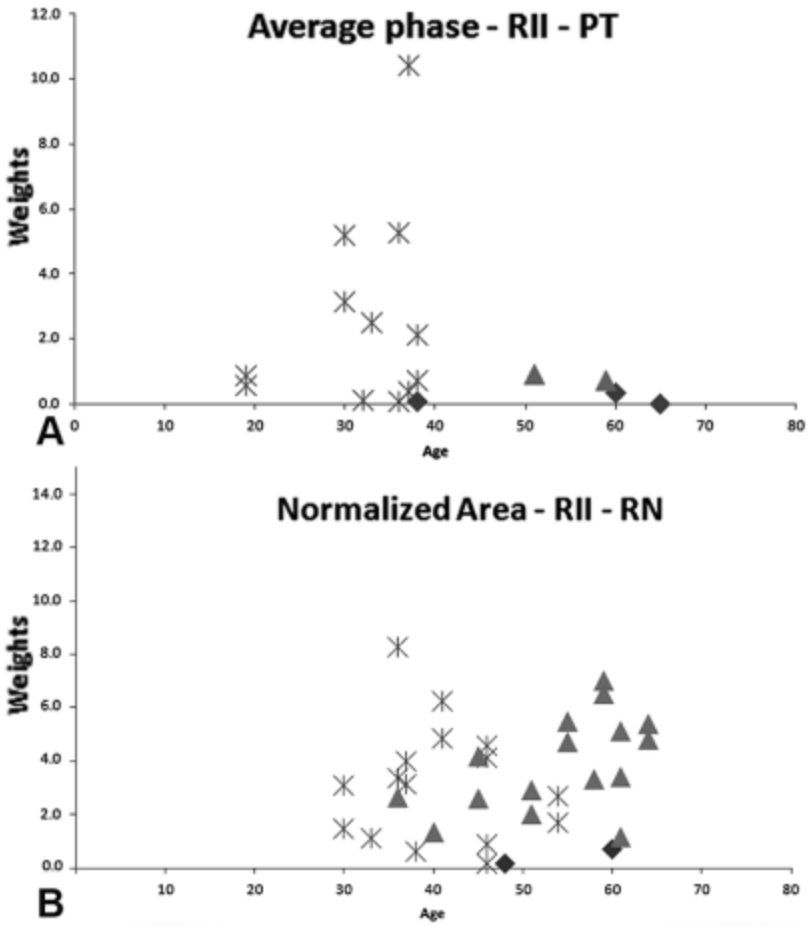

Figure 7.3: Plots showing individual weighting of different parameters (average phase: upper row, normalized area: middle row and the total phase: lower row) of the pulvinar thalamus (A, B, C) and the red nucleus (D, E, F). The asterisks represent the RRMS patients, the triangles represent the SPMS and the diamonds represent the healthy subjects. MS patients and normal subjects with weighting higher than 1 are shown in the plots (these results correspond to m=3 - for quantitative evaluation, please refer to table 7.1).

Figure 7.3 displays the individual weighting results calculated using Eq. (1) for the PT, and RN. A clear separation between normal subjects and MS was visualized with MS patients having iron content higher than 3 times the SD of normal subjects. Figure 7.4 displays the subtotal weighting of the 4 structures for each measured parameter including average phase, normalized area and total phase. The last graph, Figure 7.4d, shows the total weighting of all the parameters of the CN, PT, RN and SN combined. The figure also demonstrates that there were

no normal controls younger than roughly 40 years with abnormal iron content, as reflected by a weight factor larger than 1.0.

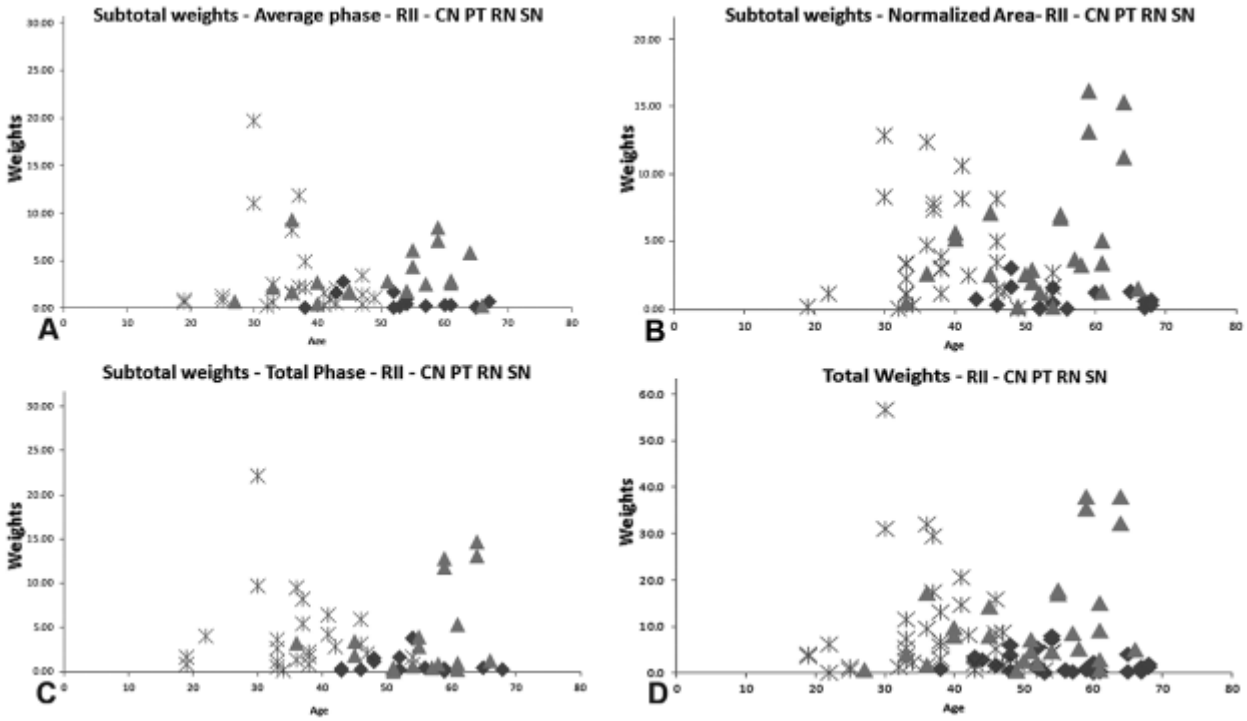

Figure 7.4: Four plots showing the subtotal (A, B and C) weighting factors and the total weighting factor (D) of the four structures with the weighting factor greater than 1 (these results correspond to m=3): CN, PT, RN and SN. The asterisks represent the RRMS patients, the triangles represent the SPMS patients and the diamonds represent the healthy subjects. For quantitative results of these graphs, please refer to table 7.2.

The percentages of patients with abnormal iron content in both control subjects and MS patients are shown in Tables 7.1 and 7.2. Note that in these tables, the evaluations and calculations were done for both hemispheres thereby resulting in a total which is 2 times the number of subjects[*]. In Table 7.1, individual weights (one parameter for one structure), subtotal weights (one parameter for all the structures) and the total weights (all parameters for all the structures) are displayed for m=2 and m=3 (higher than 2 and 3 times the SD, respectively). Comparing normal subjects to MS patients ($p<0.05$), the total weights showed that 76% of all MS patients have abnormally high iron content (higher than 2 SD) in at least one of the

structures whereas only 27% of controls have abnormally high iron content. Similar results were seen for subtotal and individual weights (except in the putamen). Results for subjects with iron deposition higher than 3 SD still show still high values for MS patients.

Table 7.1: Abnormal iron deposition weighting (percentage) for normal controls (N) and MS patients (P).

Total Weights		**N**				**P**	
		29.7				80.1	
Subtotal Weights		**N**	**P**	**N**	**P**	**N**	**P**
		RII – Average Phase		**RII – Normalized Area**		**RII – Total Phase**	
		17.2	52.8	17.6	63.2	16.9	52.8
Individual Weights	CN	4.7	21.6	4.41	19.8	–	–
	PT	1.8	29.2	4	34.9	–	–
	RN	4.4	35.8	–	–	5.8	33.01
	SN	3.3	23.58	4.4	35.8	–	–
	GP	4.4	8.4	3.67	10.3	–	–
	THA	4.04	21.7	3.67	4.7	–	–
	PUT	4.77	3.77	4.41	5.6	–	–

N: Percentage of normal subjects lying above 2 standard deviations from the normal mean ($p<0.05$). P: Percentage of patients lying above 2 standard deviations from the normal mean. The dash (–): data not available.

In table 7.2, we display the total and subtotal weights calculated from CN, PT, RN and SN iron content that again lies above 2 and 3 times higher than SD (m=2 and 3 in Eq.(1))MS patients were divided into RR and SP and into two age ranges (≤40 and >40). We found that 27% of the normal population, 74% of RRMS patients and 79% of SPMS patients had iron content above 2 SD from the mean while 13% of control subjects have higher than 3 SD iron content compared to 67% of SPMS patients and 65% RRMS patients. The younger RRMS population tends to have a higher percentage of abnormal iron deposition compared to normal controls. for m=2 and m=3 except for subtotal weight – average phase.

Table 7.2: Total and subtotal iron content weightings of all the four structures (CN, PT, RN and SN) for normal controls and MS patients with iron content higher than 3 standard deviations. RR: Relapsing Remitting MS; SP: Secondary progressive MS; TMS: Total number of MS patients.

Total Weights			
	RR MS/TMS	*SP MS/TMS*	*Normal High/Total*
20-40	24/36 (67%)	4/8 (50%)	1/112 (1%)
41-70	16/26 (62%)	24/34 (71%)	30/132 (23%)
20-70	40/62 (65%)	28/42 (67%)	31/244* (13%)
Subtotal Weights – Normalized Area			
	RR MS/TMS	*SP MS/TMS*	*Normal High/Total*
20-40	19/36 (53%)	4/8 (50%)	0/112 (0%)
41-70	12/26 (46%)	20/34 (59%)	15/132 (11%)
20-70	31/62 (50%)	24/42 (57%)	15/244 (6%)
Subtotal Weights – Average Phase			
	RR MS/TMS	*SP MS/TMS*	*Normal High/Total*
20-40	16/36 (44%)	6/8 (75%)	1/112 (1%)
41-70	9/36 (35%)	14/34 (41%)	13/132 (10%)
20-70	25/62(40%)	20/42 (50%)	14/244 (6%)
Subtotal Weights – Total Phase			
	RR MS/TMS	*SP MS/TMS*	*Normal High/Total*
20-40	17/36 (47%)	1/8 (13%)	0/112 (0%)
41-70	8/26 (31%)	17/34 (50%)	14/132 (11%)
20-70	25/62 (40%)	18/42 (43%)	14/244 (6%)

*Both the left and right hemispheres measurements were included in this calculation: therefore, since the total number of normal controls is 122, including the left and right measurements together will lead to 244 as the total count. This doubling is also applies to the MS population studied; there is 62 values quoted for RR and 42 values for SP, yielding a total of 104.

Discussion

The interest and association of MS with veins and iron deposition is not new (Haacke, 2011). We know that the basal ganglia from the dentate nucleus, the midbrain and up to the thalamostriate system are all drained by the medial venous drainage system out into the straight sinus. It is just these regions that have increased iron content as seen with SWI and with conventional MRI (Neema et al., 2009; Singh and Zamboni, 2009). The recent work of Haacke et al (Haacke et al., 2010a) suggests that the iron increase seen in MRI occurs at the confluence of the small draining veins out of the structures of interest such as the putamen, globus pallidus and caudate nucleus. Given the previous evidence that MS is a perivenular disease and that iron builds up in the venule wall (Adams, 1988; Zamboni, 2006), it may be that these increases in iron represent venous endothelial. However, it is still unknown whether iron deposition is a cause or a consequence of the inflammatory demyelinating aspect in MS pathology. On the other hand, the work by Neema et al (Neema et al., 2009) showed the presence of deep gray matter T2 hypointensities and suggested that excessive iron deposition is associated with the progression of disease.The plots in Figure 7.3 show that SPMS and RRMS are well separated with a dominance of RRMS for younger ages and dominance of SPMS for older ages.

MR phase information has become more frequently used to evaluate iron content as a function of age in the human brain (Ogg et al., 1999; Xu et al., 2008). In a previous paper, we introduced the concept of a high iron content region and normal iron content region (Haacke et al., 2010a; Haacke et al., 2010c). This made it possible to study not only smaller increases in iron content more confidently but also to study both the average iron content per pixel and the normalized area of increased iron content with age which showed different and interesting results as mentioned earlier (Haacke et al., 2010c; Zivadinov et al., 2010). This approach revealed subtle

changes in iron content that cannot be seen with the single region approach because even large increases in iron in a small area would be washed out when looking at iron over the whole region. The variability shown in our results demonstrates that evaluating abnormal iron content is not best achieved by using total iron content measurements. Rather, more information can be obtained by evaluating the area of the high iron content region as well as the average iron content per pixel. These two measures appear to present better quantitative indicators of iron content abnormality. In this study, the CN, PT, RN and SN are shown to be more susceptible to abnormal iron deposition than the other structures studied (with RN being the most susceptible (30%) followed by the PT (27.9%) - see table 7.1). However, no significant correlation of iron content with EDSS was found with any of the measures we did regardless of the structure studied. This high iron content seen in the basal ganglia, the thalamus and the midbrain structures may be consistent with the hypothesis of venous hypertension (Singh and Zamboni, 2009).

Conclusion

Abnormal iron content using the total iron weighting scheme described herein was clearly identified in RRMS patients especially those less than 40 years of age with almost no abnormal iron seen in the normal population. Evidently, iron in the basal ganglia (CN), thalamus (PT) and the midbrain (RN and SN) may be a biomarker for MS. Further work in this direction would be to compare iron content with severity of venous disease in chronic cerebrospinal venous insufficiency.

Chapter Eight

CEREBRAL VASCULATURE OF SWINE AS A PROBABLE MODEL FOR NEURODEGENERATIVE DISEASE

Introduction

The use of animal models in research has provided a wealth of information about the etiology of many diseases (Batoulis et al., 2011; Chesselet and Richter, 2011; Li et al., 2011; Liu et al., 2012; Mao et al., 2012). In multiple sclerosis (MS), which is known to be an inflammatory, demyelinating disease, the main etiology remains unknown (Batoulis et al., 2011; Noseworthy et al., 2000b). Whether inflammation is the triggering factor or a consequence of the pathological cascade is yet to be determined (Haacke et al., 2010a). The heterogeneity of MS pathological substrates has led to developing many animal models to address different triggering factors. The following models are mainly used: toxic agent induction of MS (Dousset et al., 1995), viral models (Schneider, 2009) and experimental autoimmune encephalomyelitis (EAE) models (Batoulis et al., 2011). All these models investigate the role of the immune system in MS development; however, other aspects including: genetic predisposition, aberrant cranial anatomy, vascular risk factors, and traumatic brain injury have shown evidence as potential causative or progressive agents to the disease (Damadian and Chu, 2011; Haacke, 2011; Milo and Kahana, 2010; Ramagopalan et al., 2010), therefore necessitating further investigation.

Recently, the role of vascular abnormalities in MS has regained a worldwide interest as a probable contributing factor to the pathology of MS (Zamboni et al., 2009). This study of Zamboni et al. has shown that extracranial venous anomalies are seen in MS patients and strongly correlate with the disease course. This has led researchers to look for a correlation of vascular treatment using percutaneous transluminal angioplasty (PTA) with clinical outcomes (Zamboni et al., 2011; Zivadinov et al., 2011). Using MRI, it has been shown that MS patients

with stenotic internal jugular veins (IJV) also show reduced outflow through these vessels with the development of collateral outflow routes and no flow related adaption in the cervical arterial system (Feng et al., 2012a; Haacke et al., 2012c). In the 1930s, Tracey Putnam attempted to show the critical role of venous drainage by blocking the small veins in the canine brain (Putnam, 1935). His results showed that, for the most part, canines developed sclerotic lesions in the presence of obstructed blood drainage from the brain. Our goal here is to evaluate the vasculature of the Yucatan pig in an effort to prepare for a series of experiments to see if reduced venous flow in the pig also leads to the development of sclerotic lesions. If this can be done, it would represent a major breakthrough in the understanding of the etiology of MS. Although this new theory has been the main drive behind this study, MS is not the only disease with a vascular aspect (Haacke et al., 2012a) and, thus, a vascular animal model may well benefit studies on vascular related neurological diseases as well.

The use of pigs (swine) as animal models is not novel approach (Schook et al., 2005). The driving force for investigating swine is the fact that their neurovasculature is similar to that in humans. Previous swine models have been used to study cardiovascular diseases (Reffelmann et al., 2004) as well as neurological disease (Andaluz et al., 2002; Duhaime, 2006; Kornum and Knudsen, 2011); however, no one has used these animals to study the cerebrovascular aspect of neurological disease. In reviewing the literature, few papers have discussed the anatomy of the pig's cerebrovasculature with a focus on the venous side (Ghoshal and Zguigal, 1986; Lavoie et al., 2008). Reported results do not agree on how the venous vasculature drains blood from the brain. In one study (Ghoshal and Zguigal, 1986), Ghoshal and Zguigal show that the cerebral blood drains along four different pathways while Lavoie et al. (Lavoie et al., 2008) show that the blood from the brain drains through only two pathways (see figure 8.1). The disagreement

between these two studies comes from the use of different techniques to assess the veins as well as the number of pigs used. In this paper, we used magnetic resonance imaging (MRI) to assess the pig's cerebrovasculature *in vivo* in order to understand the venous anatomy of the pig and to show the similarities between human and pig vascular anatomy.

Material and Methods

Animals

Three micro Yucatan pigs (swine) have been used in this study and were maintained in accordance with the National Research Council's Guide for the Care and Use of Laboratory Animals (2010) at Wayne State University, an AAALAC-accredited institution. All procedures were reviewed and approved by the university's Institutional Animal Care and Use Committee. The ages when the pigs were imaged varied between 5 and 7 months. Amongst these three pigs, two were female and one was male. The weight of the three pigs was 21, 22 and 23 kg respectively.

Preparation for MR scans

After the delivery of the animals, all pigs underwent a one week acclimation period. At the time of the MR scan, all animals were sedated using 33 mg/kg IM ketamine and 0.5 mg/kg IM midazolam and were intubated and manually ventilated. Anesthesia was maintained with propofol (12-20 mg/kg/hr IV continuous rate infusion) throughout the duration of transportation and the scan. During scanning, all pigs were positioned at rest on their right side with their head facing into the bore.

MR protocol

Although this study is vascular by nature, the protocol consisted of many MR sequences to assess both the structural and functional anatomy of the pig. The protocol included the following sequences: an axial 2D time-of-flight (TOF) MR venography (with saturation pulse) and arteriovenography (with no saturation pulse) scans for the neck and head vasculature; an axial 2D phase-contrast (PC) MR scan for flow quantification; an axial high resolution 3D TOF MR arteriovenography of the brain; and sagittal 3D volumetric interpolated breath-hold sequence VIBE to assess the vasculature of the brain and neck. 2D PC MRI data were collected to observe flow in the extracranial veins of the neck in each of the three pigs at the vertebral levels of C6/C7 and C3/C4 as well as at the outer base of the cranium. Additional extracranial flow data was collected on the male pig to provide a more comprehensive map of flow including a slice positioned perpendicular to flow exiting the cranium, at the inner base of the cranium, and at the C1 neck level. 2D PC MRI data were also collected on the male pig through intracranial structures of interest: the ophthalmic sinus, dorsal sagittal sinus (DSS), straight sinus (SS), and transverse sinus. In addition: an axial 2D T2 weighted scan; coronal T1 weighted scan; an axial fluid attenuated inversion recovery (FLAIR) scan; and susceptibility weighted imaging (SWI) scan were collected to assess the structural anatomy of the pig brain. Parameters for sequences collected are presented in Table 8.1. The following scans were collected post contrast agent injection: 3D TOF angiography, 3D VIBE and SWI. The contrast agent used was Magnevist [Bayer, Wayne, New Jersey] and was injected with a concentration of 0.2 mL/kg [0.1 mmol/kg]). The total scan time was one hour and 40 minutes.

Data processing

Data were processed using Signal Processing in Nuclear MR software (SPIN, Detroit, Michigan). This software has been used to create 3D models of the pigs' vasculature in order to visualize and understand the vascular system. SPIN was also used to quantify the flow in all vessels through a manually defined cross section at different levels of the neck and head.

Results

Structural cerebral anatomy of the pig

Figure 8.2 displays the axial slices across the whole brain seen on T2 weighted imaging. The contrast between white matter, gray matter and the ventricles is well visualized at all levels. This contrast was also seen on the T1 weighted images shown in figure 8.3. The T1 weighted images, that were originally acquired coronally, are displayed in figure 8.4. This figure shows: the cerebral hemisphere; the corpus callosum; the cerebellum; the hypothalamus; the pons and the spinal cord. These structures are seen and well defined in the human anatomy.

Swine Cerebral Venous Vasculature

The cerebral drainage system of the pig was well visualized using high resolution 3D TOF MR arteriovenography and 3D VIBE (figure 8.5). For our purposes, the similarity between humans and the pig brain anatomical and vascular structures is notable in the area of the thalamostriate veins, vein of Galen, and straight sinus (figure 8.5a). Figure 8.5 highlights the drainage of the DSS (analogous to the superior sagittal sinus), which drains the superficial veins of the brain. The SS drains the inferior sagittal sinus as well as the central cerebral vein and the basal vein. The SS joins the DSS at the torcular herophili, and bifurcates primarily into the

transverse sinuses as seen in figure 8.5b. Figure 8.6 on the other hand displays cross sections of the brain's vasculature using susceptibility weighted imaging, which is known to reveal the venous microvasculature. Figure 8.6a shows the superficial cerebral veins while figure 8.6b and 8.6c show an axial view revealing the thalamostriate system at the level of the basal ganglia and midbrain of the pig.

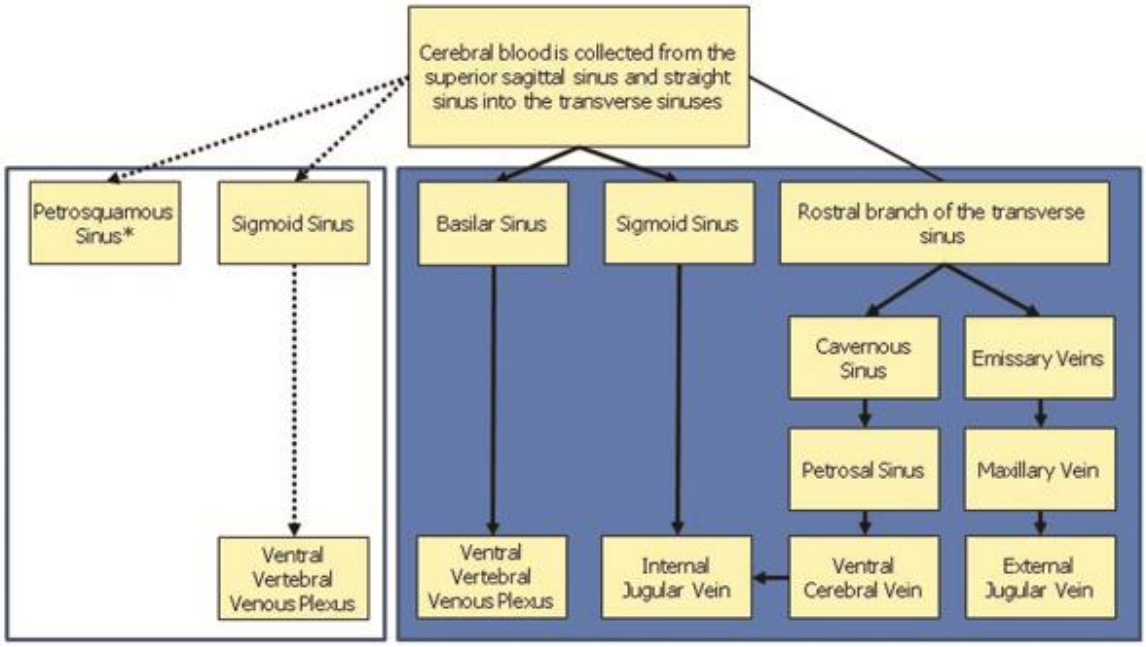

Figure 8.1: The venous drainage system of the swine reported in the literature. The solid lines show what was reported by Ghoshal et al. 1986 and the dashed lines show what was reported by Lavoie et al. 2008. *The author did not report any continuity of the petrosquamous sinus.

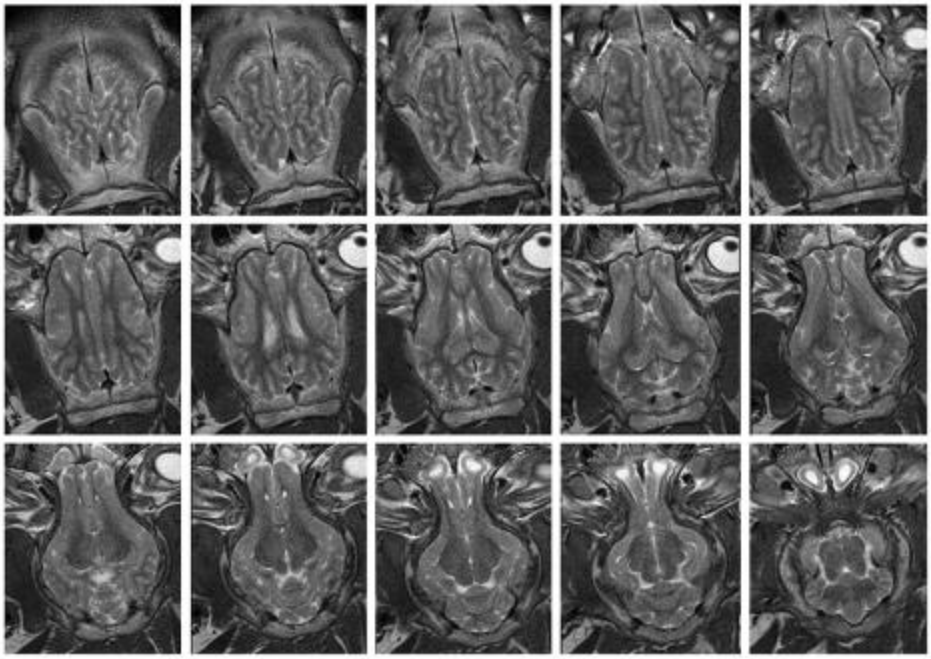

Figure 8.2: T2 weighted images showing an axial cross section along the whole brain, revealing good contrast between white matter, gray matter and CSF similar to that seen in humans.

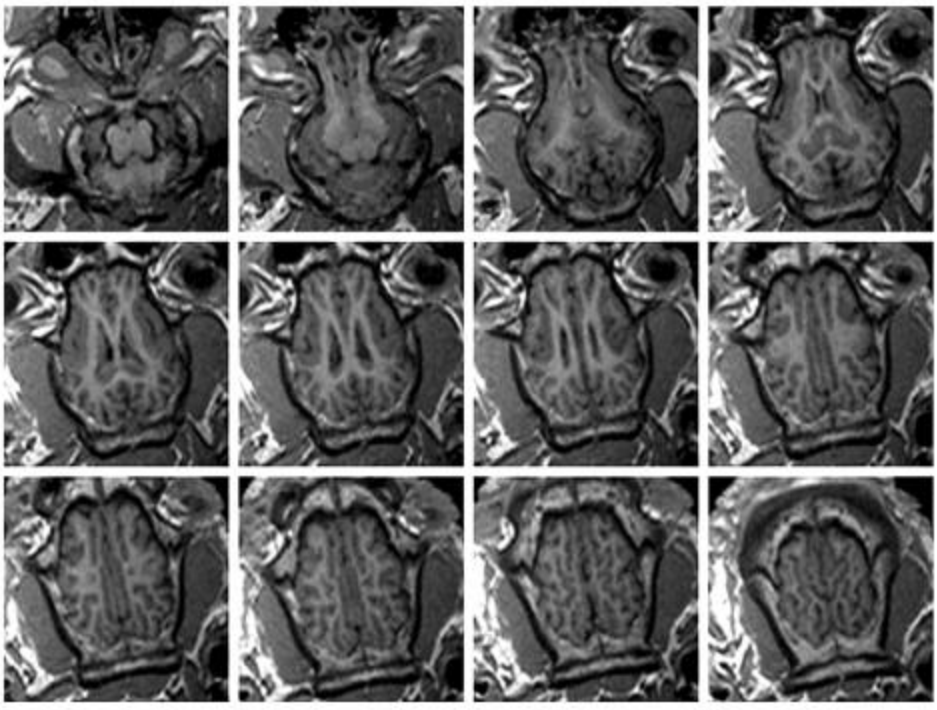

Figure 8.3: T1 weighted images showing an axial cross section along the whole brain, revealing good contrast between white matter, gray matter and CSF similar to that in humans.

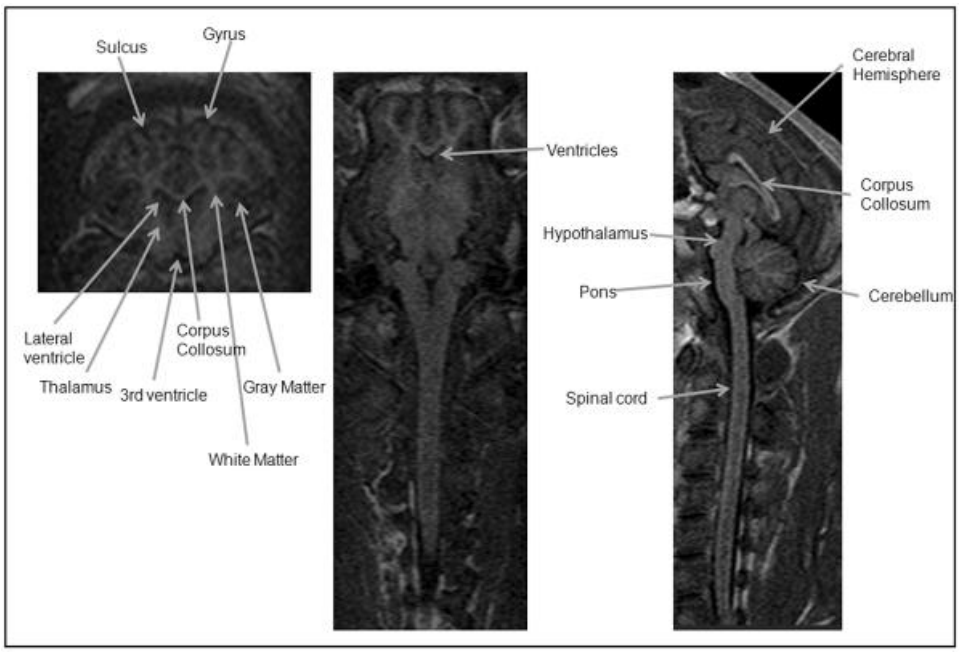

Figure 8.4: T1 weighted images showing coronal, axial and sagittal views (left to right) displaying different structures of the brain and the spinal cord.

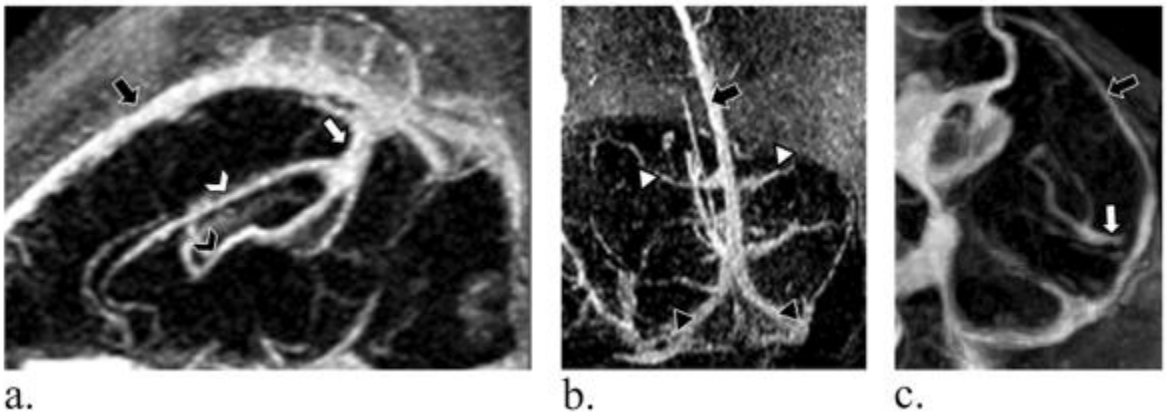

Figure 8.5: A and B - 3D post contrast MRV, C - 3D VIBE. Dorsal sagittal sinus (DSS) (black arrow); internal cerebral vein (white chevron), thalamostriate system (black chevron); straight sinus (SS) (white arrow); cerebral superficial veins (white arrow head); transverse sinuses (black arrow head).

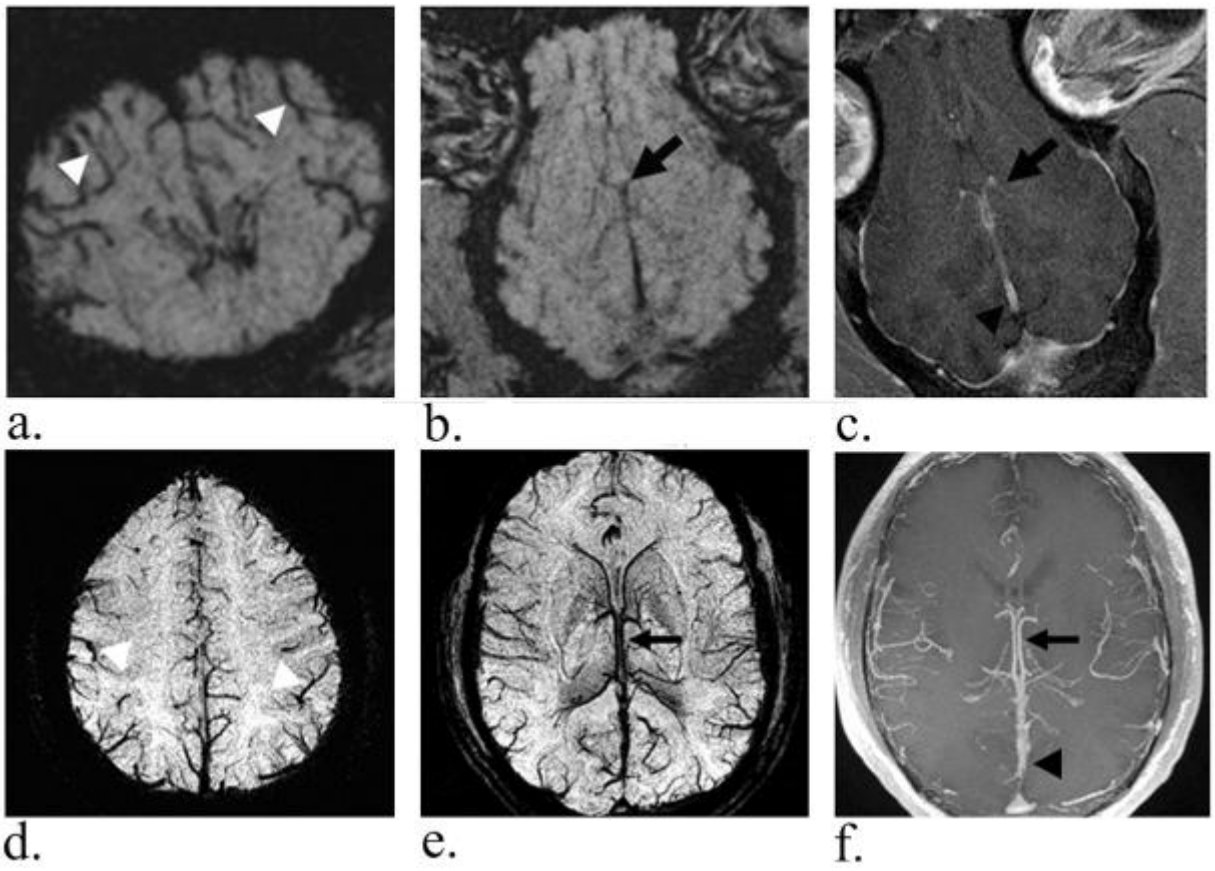

Figure 8.6: Left and middle - SWI, Right - T1 weighted images post contrast. Superficial cerebral veins (white arrow head) and thalamostriate system (black arrow) draining through the internal cerebral vein into the vein of Galen back to the straight sinus (arrow head) in the pig (A-C) and the human (D-F).

The vasculature at neck level

Imaging the neck using axial 2D TOF MRV and 2D TOF MRA has revealed different components of the blood supply and blood drainage to and from the brain. Figure 8.7a shows the common carotid arteries which bifurcate into internal and external carotid arteries. The internal carotid arteries go on to supply the brain, while the external carotid arteries supply the frontal part of the head. Figure 8.7b, on the other hand, shows the external jugular veins which drain the

frontal part of the head. In addition, we see the internal jugular veins which drain the cavernous sinus back into the brachiocephalic trunk. A large venous structure (figure 8.7c) is seen which represents a dominant drainage route from the brain, and runs parallel with the spinal cord. Many papers have referred to it as the ventral vertebral venous plexus (VVVP) or the paraspinal venous network (Lavoie et al., 2008). This is homologous to the epidural plexus in humans, however, in the supine position, the dominant outflow in the human is most commonly through the IJVs and in the upright position through the paraspinal network (Alperin et al., 2005). In humans, the anterior condylar confluent allows for the redirection of blood flow between these vessels (San Millan Ruiz et al., 2012), however this structure was not clearly noted in the vasculature of the pig. Anastomoses of varying diameter were observed between the IJV, external jugular veins (EJV), and VVVP in all three pigs.

The vasculature as a whole

Figure 8.8 displays the entire vasculature of the pig including both arteries and veins at the brain and neck levels as visualized on 2D TOF MRV data. As mentioned previously, the DSS drains all the superficial veins of the brain. The straight sinus, which drains the center of the brain, joins the DSS to drain into the transverse sinuses. The transverse sinuses run bilaterally and then bifurcate to rostral and basal branches, with the former running between the occipital lobe and the cerebellum and the latter running dorsal to the cerebellum. The rostral branch connects the transverse sinus to cavernous sinus, which drains into the IJV through the emissary veins. Conversely, the basal branch drains into the basilar sinus, which then drains into the VVVP (or known as paraspinal venous network). The IJVs then drain into the subclavian veins

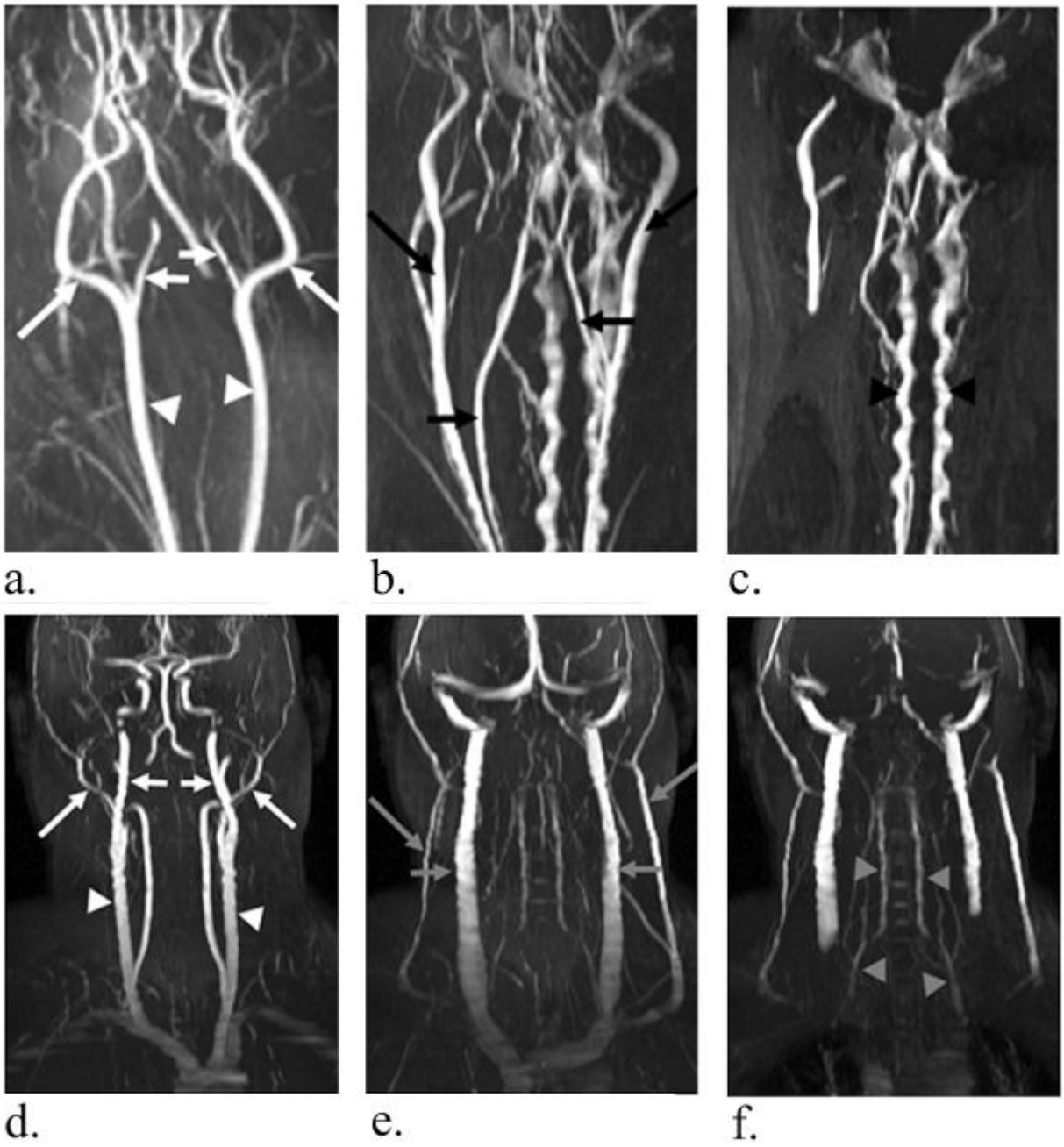

Figure 8.7: 3D projection of the 2D MRV data set. (A,D): Common carotid artery (white arrow head); internal carotid artery (short white arrow); external carotid artery (long white arrow); (B,E): internal jugular vein (short black and grey arrows); external jugular vein (long black and grey arrow) and (C,F): ventral vertebral venous plexus or also known as paravertebral veins (black and grey arrow head) in pigs (A-C) and human subject (D-F).

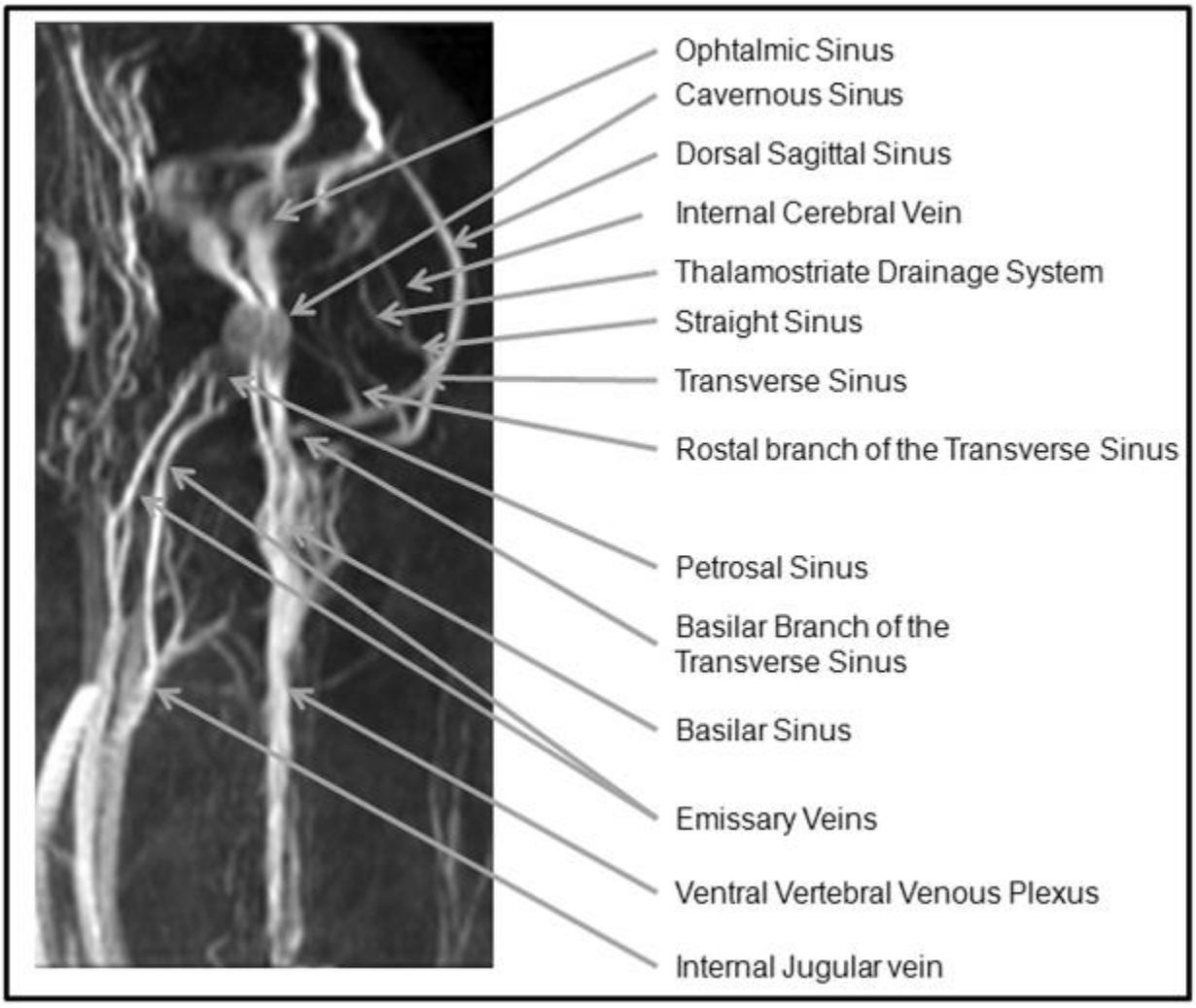

Figure 8.8: Detailed anatomical description of the drainage system of the swine brain as shown in a 3D projection of the 2D TOF MRV data set.

back into the heart, while the VVVP travels down caudal posterior, draining the spine, and reaching the subclavian vein into the heart.

Quantitative flow measurements of the vasculature of the head and neck

Flow measurements at the mid neck level revealed a dominance of blood draining into the paraspinal veins compared to the internal or external jugular veins. Table 8.2 details the quantitative flow measurements acquired at multiple levels in the head and neck for the male pig. DSS and the SS were collected on individual flow slices which were oriented perpendicular to the path of the vessel. The flow through the DSS was greater than the flow through the SS at a ratio of 2.5:1 with the DSS carrying 0.28ml/s and the SS carrying 0.11ml/s of blood. Draining from the confluence of these two sinuses, asymmetry was found in the right and left transverse sinus. The left was the strongly favored flow pathway carrying 0.46ml/s as the right transverse sinus was found to carry 0.02ml/s.

As detailed above, the transverse sinus can drain to the cavernous sinus. A flow slice was also positioned through the ophthalmic sinuses connection to the cavernous sinus as they were observed to be large structures. These structures carried greater flow than the dural sinus, with the right ophthalmic sinus showing 0.69ml/s and the left 0.65ml/s. Combining the flow from the transverse sinus and ophthalmic sinus, it was estimated that flow through the cavernous sinus was approximately 1.80ml/s; however it should be noted that smaller veins which drain to the cavernous sinus were not included. The major outflow route from the brain in the pig has been previously thought to be through the VVVP and separately through the emissary veins leading to the IJV. The quantitative flow measurements suggest that this is true, with the IJV carrying a

Table 8.1: Imaging parameters for the sequences collected during MR scanning.

Abbreviations: TOF=time of flight; PC=phase contrast; VIBE=volumetric breath-hold examination; TR=repetition time; TE=echo time; FA=flip angle; BW=bandwidth; FOV=field of view; TH=thickness. *Tracking F special saturation pulse was applied to acquire 2D MRV data.

Sequence	**2D TOF MRAV***	**2D PC MR**	**3D TOF MR`AV**	**3D VIBE**	**2D T2WI**	**3D T1WI**	**2D T2 FLAIR**	**SWI**
Orientation	axial	orthogonal to vessel	axial	sagittal	axial	coronal	axial	axial
TR (ms)	23	12	28	3.97	5000	1750	7000	29
TE (ms)	5.02	5.4	5	1.43	82	2.98	129	20
FA (degrees)	60	15	30	25	120	9	150	15
BW (Hz/pixel)	217	248	181	685	222	181	296	121
FOV (mm^2)	256x256	256x256	256x256	349x273	128x96	256x256	128x96	256x192
Matrix Size	512x512	448x448	1024x1024	384x300	256x192	512x512	256x192	512x384
Resolution (mm^2)	0.5x0.5	0.6x0.6	0.25x0.25	0.9x0.9	0.5x0.5	0.5x0.5	0.5x0.5	0.5x0.5
Slice TH (mm)	2.5	4	0.5	0.9	2	1	2	1

Table 8.2: Quantitative flow measurements acquired at multiple levels in the head and neck for the male pig. Data shown reflects the flow acquired on 7 separate phase contrast MRI slices.

Vessel name	Right Sided Flow (ml/s)	Left Sided Flow (ml/s)	Combined Flow (ml/s)
Intracranial Venous Vasculature			
Dorsal sagittal sinus	0.28		0.28
Straight sinus	0.11		0.11
Total for mid-line dural sinus	*0.39*		*0.39*
Transverse sinus	0.02	0.46	0.48
Opthalmic sinus	0.67	0.65	1.32
Total flow to cavernous sinus	*0.69*	*1.11*	*1.80*
Extracranial Venous Vasculature as it exits the cranium			
Emissary vein of internal jugular vein	0.26	0.68	0.94
Ventral vertebral plexus	0.51	0.59	1.10
External jugular vein	0.49	0.43	0.92
Anterior facial vein	0.02	0.30	0.32
Total flow exiting cranium	*1.28*	*2.00*	*3.28*
Extracranial Venous Vasculature at the inner base of the skull			
Internal jugular vein	0.23	0.66	0.89
Ventral vertebral plexus	1.01	0.77	1.78
External jugular vein	0.53	0.57	1.10
Anterior facial vein	0.36	1.04	1.40
Total flow at the inner base of the skull	*2.13*	*3.04*	*5.17*
Extracranial Venous Vasculature at the outer base of the skull			
Internal jugular vein	0.23	0.64	0.87
Ventral vertebral plexus	0.66	0.95	1.61
External jugular vein	1.11	0.36	1.47
Anterior facial vein	0.55	0.97	1.52
Total flow at the outer base of the skull	*2.55*	*2.92*	*5.47*
Extracranial Venous Vasculature at the C1 vertebral level			
Internal jugular vein	0.40	1.41	1.81
Ventral vertebral plexus	0.94	1.05	1.99
External jugular vein	0.93	0.87	1.80
Anterior facial vein	0.00	0.49	0.49
Total flow at the C1 vertebral level	*2.27*	*3.82*	*6.09*
Extracranial Venous Vasculature at the C4 vertebral level			
Internal jugular vein	0.10	1.58	1.68
Ventral vertebral plexus	1.37	1.31	2.68
External jugular vein	0.99	1.48	2.47
Total flow at the C4 vertebral level	*2.46*	*4.37*	*6.83*
Extracranial Venous Vasculature at the C7 vertebral level			
Internal jugular vein	0.24	1.92	2.16
Ventral vertebral plexus	1.62	1.64	3.26
External jugular vein	1.28	1.30	2.58
Total flow at the C4 vertebral level	*3.14*	*4.86*	*8.00*

Table 8.3: Comparison of the distribution of flow through the major veins of the neck for all three pigs. Values shown are percentage of total venous flow quantified for a given level in a given pig, therefore the percentages will add to 100 for each pig. Abbreviations: R=right sided; L=left sided; IJV=internal jugular vein; EJV; external jugular vein; VVVP=ventral vertebral venous plexus; AFV=anterior facial veins.

Parameter	Pig 1	Pig 2	Pig 3	Average (St Dev)
Sex	Male	Female	Female	
Age	7 months	5 months	6 months	
Weight	23 kg	21 kg	22 kg	
		Foramen Magnum Flow Results		
R-IJV	4.2	11.0	5.0	6.8 (3.7)
L-IJV	11.7	8.5	4.4	8.2 (3.7)
R-EJV	20.4	12.5	19.6	17.5 (4.3)
L-EJV	6.6	19.1	18.8	14.8 (7.1)
R-VVVP	12.1	13.9	14.3	13.4 (1.2)
L-VVVP	17.4	18.9	27.2	21.2 (5.3)
R-AFV	10.1	5.7	4.2	6.7 (3.0)
L-AFV	17.4	10.5	6.5	11.4 (5.6)
		C3/4 Flow Results		
R-IJV	1.5	0.1	1.6	1.1 (0.8)
L-IJV	23.1	14.4	2.2	13.2 (10.5)
R-EJV	14.5	13.7	22.8	17.0 (5.0)
L-EJV	21.7	29.4	30.1	27.1 (4.7)
R-VVVP	19.2	16.6	19.9	18.6 (1.7)
L-VVVP	20.1	25.7	23.3	23.0 (2.8)
		C6/7 Flow Results		
R-IJV	2.9	1.3	1.6	1.9 (0.9)
L-IJV	23.4	16.5	2.3	14.1 (10.7)
R-EJV	19.8	19.9	26.4	22.0 (3.8)
L-EJV	20.0	25.2	29.2	24.8 (4.6)
R-VVVP	15.6	16.5	18.7	16.9 (1.6)
L-VVVP	18.3	20.6	21.8	20.2 (1.8)

combined 0.89ml/s and the VVVP 1.10ml/s of flow on a flow slice positioned perpendicular to flow as it exits the cranium. Asymmetry was found in the flow between the right and left IJV with a ratio of 2.6:1 while the flow in the VVVP had a ratio of 1.2:1 with left sided dominance.

A comparison of the flow through the major veins of the neck for all three pigs is shown in Table 8.3. Flow was normalized to total venous flow quantified in order to limit bias due to potential differences in total flow between pigs. Veins were classified as: VVVP, IJV, EJV, and anterior facial veins (AFV). The AFV represented a diverse group of veins including those within the superficial, ventral region as well as those surrounding the trachea and esophagus. The EJV included were lateral vessels which appeared to drain the nose and superficial tissues. The IJV were identified as the continuation of the emissary vein originating from the cavernous sinus, and their close proximity to the internal and common carotid arteries were also evident. The VVVP were identified as those vessels surrounding the dural sac and also, when observed, smaller vessels in the paraspinal region. Some vessels were excluded due to their small size as a definite contour was not identified.

Flow at the outer base of the cranium shows that the VVVP carried the largest portion of total venous outflow, and in each of the three pigs a left sided dominance was observed. The EJV and AFV carried high flow as well, carrying a combined flow of around half of the total venous outflow quantified in each of the three pigs (50.5+/-3.6%). Flow through the IJV was lower than the EJV or VVVP, and shows the highest variability compared to the other vessels. The pigs show three different trends for the IJV flow: left sided, right sided and bilateral dominance. In pig 3, the lowest IJV flow was quantified and an increase of flow through the left VVVP was observed without a clear increase in flow through the other vessels.

Flow at the lower neck levels of C3/4 and C6/7 demonstrated the dominance of outflow through the EJV as flow drained into these vessels from the superficial tissues and smaller veins of the face (the AFV were not clearly observed at these levels). The flow through the left IJV had the highest variability. In two pigs, it carried a large portion of venous outflow (23.4% and

16.5%); however, in one of the female pigs it carried low flow (2.3%). The right IJV was found to carry low flow in all three pigs, including pig 2 which had right sided IJV dominance at the base of the cranium. The right and left EJV carried relatively symmetric flow compared to the IJV with the left EJV carrying slightly more in each of the three pigs. The EJV drained between 39.8% of total venous outflow in the male pig to 55.6% in one of the female pigs. The VVVP carried a consistently large portion of the total venous outflow in each of the three pigs. As observed in the EJV, the right VVVP carried slightly less flow than the left.

Discussion

The main goal of this work was to visualize and understand the cerebral vasculature of the pig brain, its drainage and whether a vascular animal model is feasible for vascular related neurological diseases. In a previous study, Wang el al. (Wang et al., 2010) worked on establishing a cerebral sinus thrombosis animal model, where a thrombin was injected into the DSS of the pig. This work revealed bilateral parasagittal infarction as well as edema, the same as seen in humans using MRI. They concluded that pigs can be used as an animal model for cerebral sinus thrombosis to understand the associated pathophysiology and to develop better therapeutic approaches. In another study, Chai el al. (Chai et al., 1995) designed an experiment to test whether jugular venous ligation can change the intraluminal and intracranial pressures and hemispheric cerebral blood flow and whether removing the ligation will reverse the effect. His work showed that this procedure did increase cerebral blood flow but there was no increase in jugular venous pressure or intracranial pressure. These results can be explained by the fact that the main venous drainage system in swine is the ventral vertebral venous plexus as seen in this paper and in Lavoie et al. (Lavoie et al., 2008). In the latter paper, the authors identified an

anteriorly and rostrally coursing vein, named the petrosquamous sinus, which mainly drains into the retromandibular vein. In *homo sapiens*, the petrosquamous sinus is an embryological remnant structure which typically recedes during fetal development, its continued presence being linked to increased incidence of infection and symptoms such as vertigo. Also notable was that Lavoie et al. did not show any link between intracranial venous structures and the internal jugular veins. This link, on the other hand, was seen in our results through the cavernous sinus which drains into the jugular vein. Similar patterns have been described *ex vivo* in Ghoshal et al. (Ghoshal and Zguigal, 1986). In addition, anastomoses have been identified in our data between the vertebral venous plexus and the jugular veins in all three pigs, as well as anastomoses which bilaterally link the IJV. These results suggest that the reason Chai et al. (Chai et al., 1995) failed to see any increase in venous or intracranial pressure was because the main drainage from the brain takes place through the vertebral venous plexus which can link back to the IJV. However, if we occlude the ventral vertebral veins at the most cranial segment available, this might lead to the expected increase in intracranial pressure and a form of chronic venous hypertension.

In this respect, the use of pig as a vascular model for chronic venous hypertension is plausible. Although further research is warranted, there are still clear vascular differences between the pig and human. The ideal effect of creating the potentially causative or exacerbating forces generated in MS patients exhibiting chronic cerebrospinal venous insufficiency (CCSVI) has not yet been shown; however the model template is now well understood. In pigs, drainage of blood flow does not appear to be dominated by that from the brain as it is in the neck of humans. Large amounts of blood flow appear to collect in the vessels from the superficial muscle and fat pad of the pig, as well as a large supply of blood draining from the olfactory, ocular, and gustatory tissues. This flow appears to drain primarily into the EJV and AFV, but the venous

system of the pig is dynamic and contains connections between dominant outflow routes. Blood flow does drain from the brain into the VVVP and to the IJV; however, this flow could potentially become collateralized. In order to successfully obstruct blood drainage from the brain, careful evaluation of the pig's vasculature and precise occlusion techniques would be needed to ensure that appropriate stress is induced in the venous system.

The results indicate that the positioning of the pig during scanning had an effect on the overall flow in the extracranial vessels. As the pig was oriented on the right side, this may have compressed the vessels in the neck and redirected blood flow into alternative pathways. This may be a possible explanation for the low blood flow observed in the right IJV compared to the left side at the lower neck levels. This type of adaption has also been evidenced in the neck of humans, however, further research is needed to explain what effect this may have on intracranial pressure and CCSVI.

A limitation of this study is that the quantitative flow data is not cardiac gated because of the very rapid heart rate under sedation. Therefore, this limits the picture of whether reflux or bidirectional flow is present in the venous system as well as obscures the ability to assess the cerebrospinal fluid oscillatory profile. Despite this, MRI allows for the quantification of blood flow on average, and when normalized to total arterial flow can give indications of the redirection of blood flow in the presence of obstruction in the dominant, venous outflow routes in comparison to the baseline explained in this work.

In conclusion, we have shown that MRI can provide a complete visualization of the cerebral venous drainage system and its function in the pig brain and neck. Blood flow can be quantified and the proportion of blood leaving the brain through the vertebral venous plexus and

internal jugular vein analyzed. The structures seen suggest that in order to initiate a stress on the venous system in the brain, the large ventral vertebral venous plexus will need to be occluded.

Chapter Nine

CONCLUSIONS AND FUTURE DIRECTIONS

Conclusions

In this thesis, we used a modern 3T MR whole body human spectrometer to study one of the most important molecules in the brain, iron, and its manifestation in multiple sclerosis. Due to its magnetic characteristics, we were able to visualize and resolve the brain structures and sub-structures *in vivo* using a new technique known as susceptibility weighted imaging. This technique presented a better contrast and differentiation compared to conventional MR sequences. Its accuracy was validated quantitatively against one of the most dependable iron imaging techniques, X-Ray fluorescence, where we showed similar contrast in both methods. In this same study where we used MS cadaver brains, we were also able to report the presence of iron in MS lesions and other brain structures using both methodologies.

Taking it one step further, we assessed iron content in the midbrain and basal ganglia structures in MS patients compared to normal controls. We presented a new post processing approach to evaluate iron in the structure of interest. Our results showed an increase in iron content in several structures of MS brains compared to healthy subjects. Specifically, we were able to distinguish the red nucleus as being the most affected structure in older MS patients, while increases in iron in the pulvinar thalamus was more dominant in younger subjects.

Finally, we studied the similarities between the human and the pig cerebrovascular drainage systems and their routes to the heart through the neck vessels, as a means to create a new animal model for MS linking iron and lesion development to vascular abnormalities. We reported the differences, which were minor, making this model a good approach to test the vascular theory. My major efforts in the published work of chapters 4, 6, 7 and 8 were in designing the experiments followed by data acquisition and analysis. The next step of this project

is underway, and we will give a brief update on the status of that study and where we are heading as part of this work's future direction.

Future directions:

Iron in the brain

In this thesis, we presented a new approach to assess iron content in the brain of MS patients compared to normal subjects using phase images from SWI data. Although phase was able to reveal abnormal iron deposition in MS patients, phase is geometry dependent. The next step will be to repeat this analysis using a new phase post processing technique known as susceptibility weighted imaging and mapping (SWIM) that removes this geometry dependence and gives a magnetic source imaging measure of putative iron content. The resulting susceptibility map has in fact been shown to correlate well with iron content using XRF and other means. The previous phase data can be used to restudy the same group of MS patients we originally evaluated. These SWIM data will make it possible to measure iron throughout a given structure not just in one slice as in the previous work.

Multiple Sclerosis: a vascular model

The direct relationship between venous obstruction, iron deposition and inflammation (and hence tissue damage and lesion development), has not been well studied, however, every piece of this puzzle has a strong stand-alone role in MS research. A review of the literature from the past century presents decent evidence that this new vascular theory might explain some of the MS landmarks including immunological responses, vessel wall breakdown and iron deposition in lesions and in the deep gray matter.

In order to address this conflict with a convincing scientific methodology, one of the best approaches is to develop an animal model that has similar blood drainage behavior as humans, create vascular obstructions at different degrees to stress the cerebral venous system, and monitor the different aspects of venous hypertension, reduced blood flow in the brain and any developing sclerotic lesions. Changes in blood flow and iron can be monitored with MR angiography, MR venography, quantitative flow imaging and SWI. In a clinical setting, knowing the start point is never possible; by the time the patient has a series of symptoms, the damage has already taken place. Therefore, the ability to visualize and monitor structural and functional changes in this model using MRI might give us the chance to create a chronological order of the pathological pathways seen in MS.

All the steps of this proposed direction have been independently reported in the literature, including: similarities between the human and pig venous drainage systems (Ghoshal and Zguigal, 1986; Si et al., 2008; Zezula-Szpyra and Grzegorzewski, 2000), the application of venous occlusions (Schutze et al., 2007), the resulting venous hypertension in swine (Lavoie et al., 2008) and lesion development in dogs (Putnam, 1935). Currently, we are following two Yucatan micropigs, one with induced stenosis and the other as a companion normal control. In our proposed implementation of this approach, the pigs were be scanned repeatedly after ligation at post op, 3 and 6 months respectively to monitor cerebral perfusion and lesion development. Quantitative measures will be made for vessel lumen and flow for all the major veins and arteries feeding the brain to measure the cardiovascular input/output. Lesion load if seen will be compared to the flow abnormalities. However, the simple presence of lesions will be considered a major finding assuming that no lesions are present in baseline imaging. (More details of this new direction can be found in Appendix 2.)

In conclusion, MS is one of the most complex neurodegenerative diseases, with many contributing factors. Any promising approach should be investigated if it has the potential to enhance the patient's quality of life. We hope that this work will add a piece to the MS puzzle, whether it is through a better understanding of the role iron plays or by creating an animal model that will lead to a better understanding of the role abnormal venous vasculature plays as a comorbidity in multiple sclerosis.

APPENDIX A

PHASE CONTRAST QUANTITATIVE FLOW IMAGING

Introduction

Phase contrast (PC) is an MR imaging technique that has long been used to quantify flow parameters *in vivo* non-invasively. It is mainly applied to image blood and cerebrospinal fluid flow assessing local velocity. The basic concept is the use of flow encoding gradients to translate phase into velocity information. The application of those gradients (bipolar gradients) yields a linear proportionality between velocity and phase, hence they are known as velocity encoding gradients (Moran et al., 1985). In this appendix, we will briefly go through the link between phase and velocity given that we used this method in chapter 8 to draw a map of blood flow in the pig model.

The bipolar gradient is usually applied in the direction of the flow of interest Figure (A.1). The gradients are applied in one of the three logical gradient axes (read encoding, phase encoding or partition encoding direction) or can be applied along two or more if any arbitrary direction is desired. These bipolar gradients are usually added to conventional gradient echo sequences (Bernstein et al., 2004). However, we know from chapter 3 that there are other contributors to the phase component in GRE sequences (such as field inhomogeneity). Therefore, PC acquires two sets of data with the same exact parameters, except for the first moment of the bipolar gradients. The phase images from these two data sets are subtracted on a pixel by pixel basis, accentuating the flow while suppressing all other sources of unwanted phase information. In doing these subtractions, two methods are commonly used and known as phase difference (PD) and complex difference methods. Although the latter is less sensitive to partial volume effects, the former depicts the direction of the flow and contains information about the volume

flow rate. Given our interest with PD, we will go on to explain how it works after we introduce the link between phase and velocity.

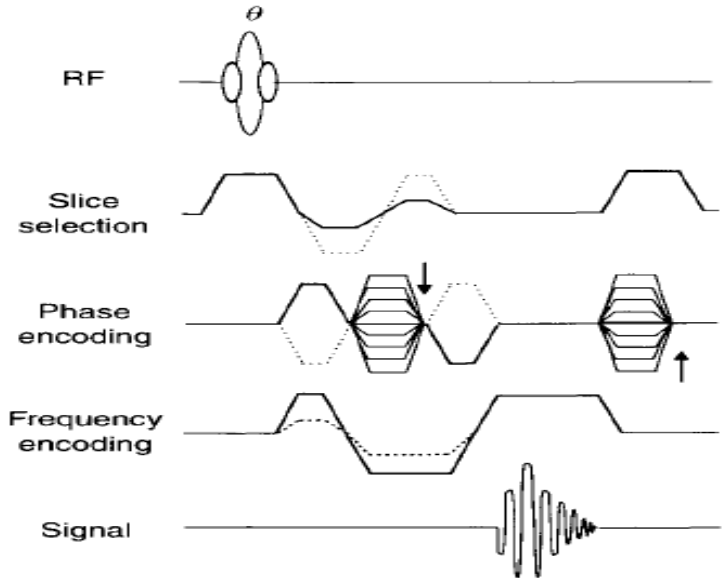

Figure A.1: Typical Phase contrast Pulse Sequence (Bernstein et al., 2004)

The amount of velocity encoding is manifest in the change in the gradient first moment (Δm_1). The relationship between the change in phase and Δm_1 is given by:

$$\Delta\varphi = \gamma \Delta m_1 v \qquad (A.1)$$

To set the dynamic range for the phase difference, the operator is asked to prescribe a parameter known as velocity encoding (v_{enc}), which is also known as the aliasing velocity. In other words, v_{enc} is defined as the velocity corresponding to a change in phase of π. From eq. A.1, we get:

$$\gamma \Delta m_1 v_{enc} = \pi \qquad (A.2)$$

Combining equations A.1 and A.2 yields:

$$\Delta\varphi = (v/ v_{enc})*\pi \qquad (A.3)$$

The choice of v_{enc} (cm/s) depends on the amount of flow we are interested in measuring. A high v_{enc} gives higher dynamic range, however it reduces sensitivity to low flow. On the other hand, low v_{enc} gives higher sensitivity but leads aliasing when $|v| > |v_{enc}|$.

The difference in phase $\Delta\varphi$ is calculated using the PD reconstruction method that we mentioned earlier. This approach uses the phase information in the image domain and applies a pixel by pixel subtraction to yield a $\Delta\varphi$ map (Haacke, 1999). In the cases where $|v| < |v_{enc}|$, the quantitative value of the velocity can be extracted from:

$$v = (\Delta\varphi/\pi)* v_{enc} \qquad (A.4)$$

In the case of aliasing, however, the velocity will be underestimated and therefore, appropriate anti-aliasing algorithms should be applied prior to PD reconstruction.

APPENDIX B

PROGRESS TO DATE OF THE VASCULAR ANIMAL MODEL OF MS

The three pigs initially imaged to understand the cerebral venous drainage system were considered as animal subjects to test the hypothesis. The surgery of the first pig was done and has achieved a complete occlusion of the right vertebral vein and a partial occlusion of the left vertebral vein (figure B.1 – post op 1 – red arrow). This process has helped decreasing the blood drainage from the brain by 20%. In a second attempt, we were successful in occluding all the jugular veins (internal and external) (post op 2 - red arrows). MR scans were and will be repeated every three months to visualize any lesion development as an association between venous abnormalities and brain damage in MS (figure B.1).

In this follow up, we have seen the development of collaterals (blue arrows) around the occluded vessel, which is reported in the majority of patients with vascular drainage abnormalities, giving us the confidence that we are on the right track. We aim to do quantitative measures for vessel lumen and flow for all the major veins and arteries feeding the brain to measure the cardiovascular input/output. Lesion load if seen will be compared to the flow abnormalities. However, the simple presence of lesions will be considered a major finding assuming that no lesions are present in baseline imaging.

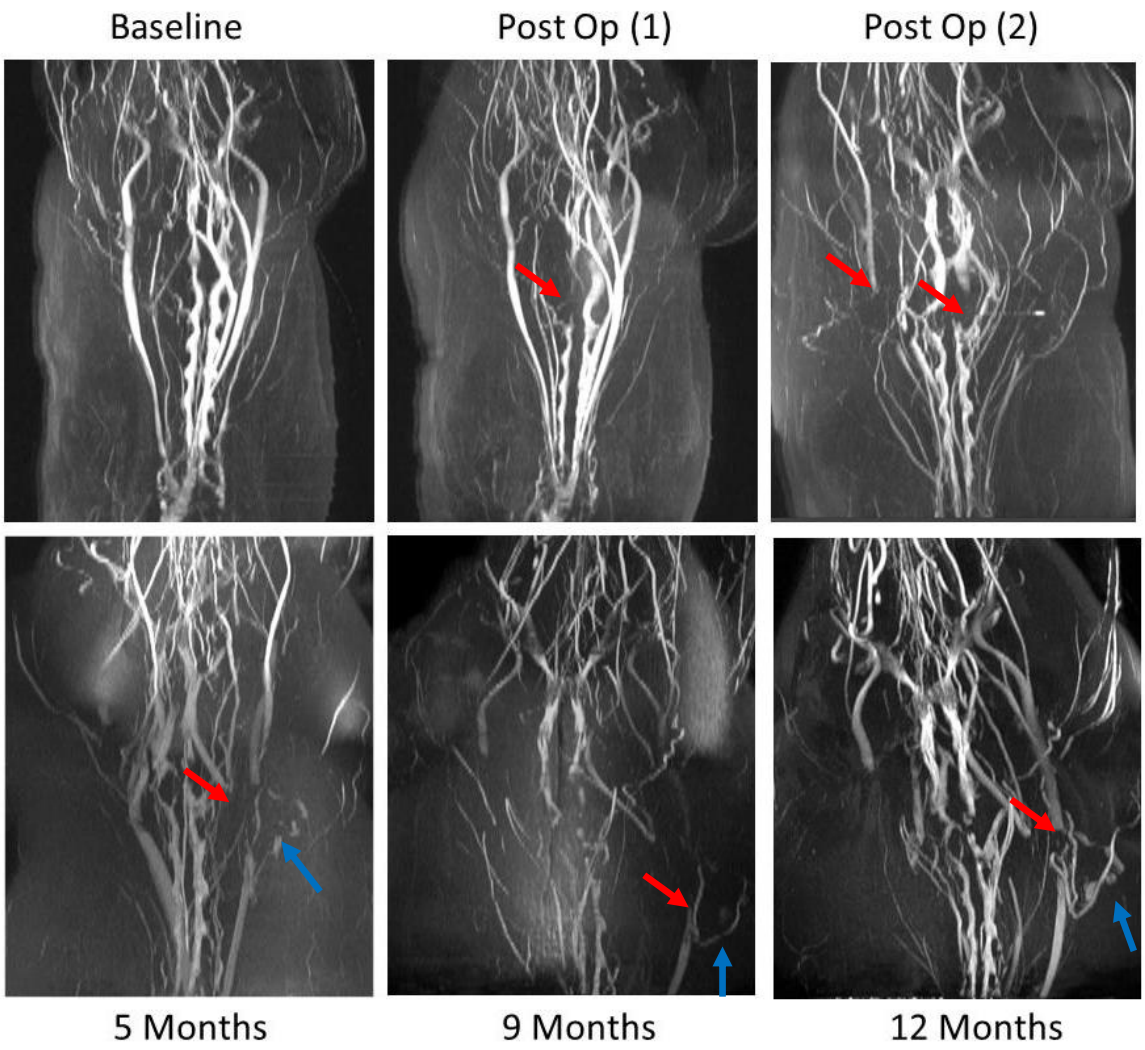

Figure B.1: The venous drainage system pre and post-surgery (5, 9 and 13 months follow-up).

APPENDIX C

THE JOHN WILEY AND SONS LICENSE TERMS AND CONDITIONS

JOHN WILEY AND SONS LICENSE TERMS AND CONDITIONS

Aug 13, 2013

This is a License Agreement between Charbel Habib ("You") and John Wiley and Sons ("John Wiley and Sons") provided by Copyright Clearance Center ("CCC"). The license consists of your order details, the terms and conditions provided by John Wiley and Sons, and the payment terms and conditions.

All payments must be made in full to CCC. For payment instructions, please see information listed at the bottom of this form.

License Number	3207100300856
License date	Aug 13, 2013
Licensed content publisher	John Wiley and Sons
Licensed content publication	Journal of Magnetic Resonance Imaging
Licensed content title	MR imaging of the yucatan pig head and neck vasculature
Licensed copyright line	Copyright © 2013 Wiley Periodicals, Inc.
Licensed content author	Charbel A. Habib,David Utriainen,Jean Peduzzi-Nelson,Elizabeth Dawe,Janine Mattei,Zahid Latif,Kenneth Casey,E. Mark Haacke
Licensed content date	Jan 24, 2013
Start page	n/a
End page	n/a
Type of use	Dissertation/Thesis
Requestor type	Author of this Wiley article
Format	Print and electronic
Portion	Full article
Will you be translating?	No
Total	0.00 USD
Terms and Conditions	

TERMS AND CONDITIONS

This copyrighted material is owned by or exclusively licensed to John Wiley & Sons, Inc. or one of its group companies (each a "Wiley Company") or a society for whom a Wiley Company has exclusive publishing rights in relation to a particular journal (collectively "WILEY"). By clicking "accept" in connection with completing this licensing transaction, you agree that the following terms and conditions apply to this transaction (along with the billing and payment terms and conditions established by the Copyright Clearance Center Inc., ("CCC's Billing and Payment terms and conditions"), at the time that you opened your RightsLink account (these are available at any time at http://myaccount.copyright.com).

Terms and Conditions

1. The materials you have requested permission to reproduce (the "Materials") are protected by copyright.

2.You are hereby granted a personal, non-exclusive, non-sublicensable, non-transferable, worldwide, limited license to reproduce the Materials for the purpose specified in the licensing process. This license is for a one-time use only with a maximum distribution equal to the number that you identified in the licensing process. Any form of republication granted by this license must be completed within two years of the date of the grant of this license (although copies prepared before may be distributed thereafter). The Materials shall not be used in any other manner or for any other purpose. Permission is granted subject to an appropriate acknowledgement given to the author, title of the material/book/journal and the publisher. You shall also duplicate the copyright notice that appears in the Wiley publication in your use of the Material. Permission is also granted on the understanding that nowhere in the text is a previously published source acknowledged for all or part of this Material. Any third party material is expressly excluded from this permission.

3. With respect to the Materials, all rights are reserved. Except as expressly granted by the terms of the license, no part of the Materials may be copied, modified, adapted (except for minor reformatting required by the new Publication), translated, reproduced, transferred or distributed, in any form or by any means, and no derivative works may be made based on the Materials without the prior permission of the respective copyright owner. You may not alter, remove or suppress in any manner any copyright, trademark or other notices displayed by the Materials. You may not license, rent, sell, loan, lease, pledge, offer as security, transfer or assign the Materials, or any of the rights granted to you hereunder to any other person.

4. The Materials and all of the intellectual property rights therein shall at all times remain the exclusive property of John Wiley & Sons Inc or one of its related companies (WILEY) or their respective licensors, and your interest therein is only that of having possession of and the right to reproduce the Materials pursuant to Section 2 herein during the continuance of this Agreement. You agree that you own no right, title or interest in or to the Materials or any of the intellectual property rights therein. You shall have no rights hereunder other than the license as provided for above in Section 2. No right, license or interest to any trademark, trade name, service mark or other branding ("Marks") of WILEY or its licensors is granted hereunder, and you agree that you shall not assert any such right, license or interest with respect thereto.

5. NEITHER WILEY NOR ITS LICENSORS MAKES ANY WARRANTY OR REPRESENTATION OF ANY KIND TO YOU OR ANY THIRD PARTY, EXPRESS, IMPLIED OR STATUTORY, WITH RESPECT TO THE MATERIALS OR THE ACCURACY OF ANY INFORMATION CONTAINED IN THE MATERIALS, INCLUDING, WITHOUT LIMITATION, ANY IMPLIED WARRANTY OF MERCHANTABILITY, ACCURACY, SATISFACTORY QUALITY, FITNESS FOR A PARTICULAR PURPOSE, USABILITY, INTEGRATION OR NON-INFRINGEMENT AND ALL SUCH WARRANTIES ARE HEREBY EXCLUDED BY WILEY AND ITS

LICENSORS AND WAIVED BY YOU.

6. WILEY shall have the right to terminate this Agreement immediately upon breach of this Agreement by you.

7. You shall indemnify, defend and hold harmless WILEY, its Licensors and their respective directors, officers, agents and employees, from and against any actual or threatened claims, demands, causes of action or proceedings arising from any breach of this Agreement by you.

8. IN NO EVENT SHALL WILEY OR ITS LICENSORS BE LIABLE TO YOU OR ANY OTHER PARTY OR ANY OTHER PERSON OR ENTITY FOR ANY SPECIAL, CONSEQUENTIAL, INCIDENTAL, INDIRECT, EXEMPLARY OR PUNITIVE DAMAGES, HOWEVER CAUSED, ARISING OUT OF OR IN CONNECTION WITH THE DOWNLOADING, PROVISIONING, VIEWING OR USE OF THE MATERIALS REGARDLESS OF THE FORM OF ACTION, WHETHER FOR BREACH OF CONTRACT, BREACH OF WARRANTY, TORT, NEGLIGENCE, INFRINGEMENT OR OTHERWISE (INCLUDING, WITHOUT LIMITATION, DAMAGES BASED ON LOSS OF PROFITS, DATA, FILES, USE, BUSINESS OPPORTUNITY OR CLAIMS OF THIRD PARTIES), AND WHETHER OR NOT THE PARTY HAS BEEN ADVISED OF THE POSSIBILITY OF SUCH DAMAGES. THIS LIMITATION SHALL APPLY NOTWITHSTANDING ANY FAILURE OF ESSENTIAL PURPOSE OF ANY LIMITED REMEDY PROVIDED HEREIN.

9. Should any provision of this Agreement be held by a court of competent jurisdiction to be illegal, invalid, or unenforceable, that provision shall be deemed amended to achieve as nearly as possible the same economic effect as the original provision, and the legality, validity and enforceability of the remaining provisions of this Agreement shall not be affected or impaired thereby.

10. The failure of either party to enforce any term or condition of this Agreement shall not constitute a waiver of either party's right to enforce each and every term and condition of this Agreement. No breach under this agreement shall be deemed waived or excused by either party unless such waiver or consent is in writing signed by the party granting such waiver or consent. The waiver by or consent of a party to a breach of any provision of this Agreement shall not operate or be construed as a waiver of or consent to any other or subsequent breach by such other party.

11. This Agreement may not be assigned (including by operation of law or otherwise) by you without WILEY's prior written consent.

12. Any fee required for this permission shall be non-refundable after thirty (30) days from receipt

13. These terms and conditions together with CCC's Billing and Payment terms and conditions (which are incorporated herein) form the entire agreement between you and WILEY concerning this licensing transaction and (in the absence of fraud) supersedes all prior agreements and representations of the parties, oral or written. This Agreement may not be amended except in writing signed by both parties. This Agreement shall be binding upon and inure to the benefit of the parties' successors, legal representatives, and authorized assigns.

14. In the event of any conflict between your obligations established by these terms and conditions

and those established by CCC's Billing and Payment terms and conditions, these terms and conditions shall prevail.

15. WILEY expressly reserves all rights not specifically granted in the combination of (i) the license details provided by you and accepted in the course of this licensing transaction, (ii) these terms and conditions and (iii) CCC's Billing and Payment terms and conditions.

16. This Agreement will be void if the Type of Use, Format, Circulation, or Requestor Type was misrepresented during the licensing process.

17. This Agreement shall be governed by and construed in accordance with the laws of the State of New York, USA, without regards to such state's conflict of law rules. Any legal action, suit or proceeding arising out of or relating to these Terms and Conditions or the breach thereof shall be instituted in a court of competent jurisdiction in New York County in the State of New York in the United States of America and each party hereby consents and submits to the personal jurisdiction of such court, waives any objection to venue in such court and consents to service of process by registered or certified mail, return receipt requested, at the last known address of such party.

Wiley Open Access Terms and Conditions

Wiley publishes Open Access articles in both its Wiley Open Access Journals program [http://www.wileyopenaccess.com/view/index.html] and as Online Open articles in its subscription journals. The majority of Wiley Open Access Journals have adopted the Creative Commons Attribution License (CC BY) which permits the unrestricted use, distribution, reproduction, adaptation and commercial exploitation of the article in any medium. No permission is required to use the article in this way provided that the article is properly cited and other license terms are observed. A small number of Wiley Open Access journals have retained the Creative Commons Attribution Non Commercial License (CC BY-NC), which permits use, distribution and reproduction in any medium, provided the original work is properly cited and is not used for commercial purposes.

Online Open articles - Authors selecting Online Open are, unless particular exceptions apply, offered a choice of Creative Commons licenses. They may therefore select from the CC BY, the CC BY-NC and the Attribution-NoDerivatives (CC BY-NC-ND). The CC BY-NC-ND is more restrictive than the CC BY-NC as it does not permit adaptations or modifications without rights holder consent.

Wiley Open Access articles are protected by copyright and are posted to repositories and websites in accordance with the terms of the applicable Creative Commons license referenced on the article. At the time of deposit, Wiley Open Access articles include all changes made during peer review, copyediting, and publishing. Repositories and websites that host the article are responsible for incorporating any publisher-supplied amendments or retractions issued subsequently.
Wiley Open Access articles are also available without charge on Wiley's publishing platform, **Wiley Online Library** or any successor sites.

Conditions applicable to all Wiley Open Access articles:

- The authors' moral rights must not be compromised. These rights include the right of "paternity" (also known as "attribution" - the right for the author to be identified as such) and "integrity" (the right for the author not to have the work altered in such a way that the author's reputation or integrity may be damaged).

- Where content in the article is identified as belonging to a third party, it is the obligation of the user to ensure that any reuse complies with the copyright policies of the owner of that content.

- If article content is copied, downloaded or otherwise reused for research and other purposes as permitted, a link to the appropriate bibliographic citation (authors, journal, article title, volume, issue, page numbers, DOI and the link to the definitive published version on Wiley Online Library) should be maintained. Copyright notices and disclaimers must not be deleted.
    - Creative Commons licenses are copyright licenses and do not confer any other rights, including but not limited to trademark or patent rights.

- Any translations, for which a prior translation agreement with Wiley has not been agreed, must prominently display the statement: "This is an unofficial translation of an article that appeared in a Wiley publication. The publisher has not endorsed this translation."

Conditions applicable to non-commercial licenses (CC BY-NC and CC BY-NC-ND)

For non-commercial and non-promotional purposes individual non-commercial users may access, download, copy, display and redistribute to colleagues Wiley Open Access articles. In addition, articles adopting the CC BY-NC may be adapted, translated, and text- and data-mined subject to the conditions above.

Use by commercial "for-profit" organizations

Use of non-commercial Wiley Open Access articles for commercial, promotional, or marketing purposes requires further explicit permission from Wiley and will be subject to a fee. Commercial purposes include:

- Copying or downloading of articles, or linking to such articles for further redistribution, sale or licensing;

- Copying, downloading or posting by a site or service that incorporates advertising with such content;

- The inclusion or incorporation of article content in other works or services (other than normal quotations with an appropriate citation) that is then available for sale or licensing, for a fee (for example, a compilation produced for marketing purposes, inclusion in a sales pack)

- Use of article content (other than normal quotations with appropriate citation) by for-profit organizations for promotional purposes
- Linking to article content in e-mails redistributed for promotional, marketing or educational purposes;
- Use for the purposes of monetary reward by means of sale, resale, license, loan, transfer or other form of commercial exploitation such as marketing products
- Print reprints of Wiley Open Access articles can be purchased from: corporatesales@wiley.com

The modification or adaptation for any purpose of an article referencing the CC BY-NC-ND License requires consent which can be requested from RightsLink@wiley.com .

Other Terms and Conditions:

BY CLICKING ON THE "I AGREE..." BOX, YOU ACKNOWLEDGE THAT YOU HAVE READ AND FULLY UNDERSTAND EACH OF THE SECTIONS OF AND PROVISIONS SET FORTH IN THIS AGREEMENT AND THAT YOU ARE IN AGREEMENT WITH AND ARE WILLING TO ACCEPT ALL OF YOUR OBLIGATIONS AS SET FORTH IN THIS AGREEMENT.

v1.8

If you would like to pay for this license now, please remit this license along with your payment made payable to "COPYRIGHT CLEARANCE CENTER" otherwise you will be invoiced within 48 hours of the license date. Payment should be in the form of a check or money order referencing your account number and this invoice number RLNK501089159. Once you receive your invoice for this order, you may pay your invoice by credit card. Please follow instructions provided at that time.

Make Payment To:
Copyright Clearance Center
Dept 001
P.O. Box 843006
Boston, MA 02284-3006

For suggestions or comments regarding this order, contact RightsLink Customer Support: customercare@copyright.com or +1-877-622-5543 (toll free in the US) or +1-978-646-2777.

Gratis licenses (referencing $0 in the Total field) are free. Please retain this printable

license for your reference. No payment is required.

APPENDIX D

THE AMERICAN JOURNAL OF NEURORADIOLOGY EDITOR'S PERMISSIONS

Mary Harder

From: charbela.habib@gmail.com on behalf of Charbel Habib [chabib@med.wayne.edu]
Sent: Monday, August 12, 2013 2:26 PM
To: Mary Harder
Subject: Permission to use the papers in my PhD thesis

Dear Mrs. Harder,

Thank you for taking my call earlier today.

Below are the two papers which are part of my PhD dissertation and has been accepted for publication in your journal.

Habib CA, Liu M, Bawany N, Garbern J, Krumbein I, Mentzel HJ, Reichenbach J, Magnano C, Zivadinov R, Haacke EM.. Assessing abnormal iron content in the deep gray matter of patients with multiple sclerosis versus healthy controls. AJNR Am J Neuroradiol. 2012 Feb;33(2):252-8. doi: 10.3174/ajnr.A2773. Epub 2011 Nov 24.

Manova ES, **Habib CA**, Boikov AS, Ayaz M, Khan A, Kirsch WM, Kido DK, Haacke EM.Characterizing the mesencephalon using susceptibility-weighted imaging.AJNR Am J Neuroradiol. 2009 Mar;30(3):569-74. doi: 10.3174/ajnr.A1401. Epub 2008 Dec 26.

I would like to request a permission to have these papers in my thesis.

Please let me know if any other information is needed for this permission to be granted.

Thank you.

Sincerely,
Charbel A. Habib, B.E., M.S.

Research Assistant
Wayne State University
MR Research Facility
Dept. of Radiology, School of Medicine
3990 John R St,
Detroit, MI 48201

Phone: (313) 966 7433
(313) 966 7432

Permission granted by the copyright owner, contingent upon the consent of the author(s); provided complete credit is given to the original source and © owner. Credit line: (initials, last name of author(s), (title of article), (name of journal), (volume #), (issue #), (inclusive pages), (year of publication, © by American Society of Neuroradiology

Per: Mary Harder 8/12/13
(Permissions Editor)

REFERENCES

2010. Guide for the care and use of laboratory animals, 8th ed. National Academy Press, Washington, DC.

Abduljalil, A.M., Schmalbrock, P., Novak, V., Chakeres, D.W., 2003. Enhanced gray and white matter contrast of phase susceptibility-weighted images in ultra-high-field magnetic resonance imaging. J Magn Reson Imaging 18, 284-290.

Abo-Krysha, N., Rashed, L., 2008. The role of iron dysregulation in the pathogenesis of multiple sclerosis: an Egyptian study. Multiple sclerosis 14, 602-608.

Adams, C.W., 1988. Perivascular iron deposition and other vascular damage in multiple sclerosis. J Neurol Neurosurg Psychiatry 51, 260-265.

Adhya, S., Johnson, G., Herbert, J., Jaggi, H., Babb, J.S., Grossman, R.I., Inglese, M., 2006. Pattern of hemodynamic impairment in multiple sclerosis: dynamic susceptibility contrast perfusion MR imaging at 3.0 T. NeuroImage 33, 1029-1035.

Albert, M., Antel, J., Bruck, W., Stadelmann, C., 2007. Extensive cortical remyelination in patients with chronic multiple sclerosis. Brain Pathol 17, 129-138.

Allen, I.V., McQuaid, S., Mirakhur, M., Nevin, G., 2001. Pathological abnormalities in the normal-appearing white matter in multiple sclerosis. Neurol Sci 22, 141-144.

Alperin, N., Lee, S.H., Sivaramakrishnan, A., Hushek, S.G., 2005. Quantifying the effect of posture on intracranial physiology in humans by MRI flow studies. J Magn Reson Imaging 22, 591-596.

Andaluz, N., Zuccarello, M., Wagner, K.R., 2002. Experimental animal models of intracerebral hemorrhage. Neurosurgery clinics of North America 13, 385-393.

Babbe, H., Roers, A., Waisman, A., Lassmann, H., Goebels, N., Hohlfeld, R., Friese, M., Schroder, R., Deckert, M., Schmidt, S., Ravid, R., Rajewsky, K., 2000. Clonal expansions of CD8(+) T cells dominate the T cell infiltrate in active multiple sclerosis lesions as shown by micromanipulation and single cell polymerase chain reaction. J Exp Med 192, 393-404.

Bakshi, R., Benedict, R.H., Bermel, R.A., Caruthers, S.D., Puli, S.R., Tjoa, C.W., Fabiano, A.J., Jacobs, L., 2002. T2 hypointensity in the deep gray matter of patients with multiple sclerosis: a quantitative magnetic resonance imaging study. Arch Neurol 59, 62-68.

Bakshi, R., Shaikh, Z.A., Janardhan, V., 2000. MRI T2 shortening ('black T2') in multiple sclerosis: frequency, location, and clinical correlation. Neuroreport 11, 15-21.

Balashov, K.E., Smith, D.R., Khoury, S.J., Hafler, D.A., Weiner, H.L., 1997. Increased interleukin 12 production in progressive multiple sclerosis: induction by activated CD4+ T cells via CD40 ligand. Proc Natl Acad Sci U S A 94, 599-603.

Barkhof, F., Filippi, M., Miller, D.H., Scheltens, P., Campi, A., Polman, C.H., Comi, G., Ader, H.J., Losseff, N., Valk, J., 1997. Comparison of MRI criteria at first presentation to predict conversion to clinically definite multiple sclerosis. Brain : a journal of neurology 120 (Pt 11), 2059-2069.

Bartzokis, G., Aravagiri, M., Oldendorf, W.H., Mintz, J., Marder, S.R., 1993. Field dependent transverse relaxation rate increase may be a specific measure of tissue iron stores. Magn Reson Med 29, 459-464.

Bartzokis, G., Mintz, J., Sultzer, D., Marx, P., Herzberg, J.S., Phelan, C.K., Marder, S.R., 1994. In vivo MR evaluation of age-related increases in brain iron. AJNR Am J Neuroradiol 15, 1129-1138.

Batoulis, H., Recks, M.S., Addicks, K., Kuerten, S., 2011. Experimental autoimmune encephalomyelitis--achievements and prospective advances. APMIS : acta pathologica, microbiologica, et immunologica Scandinavica 119, 819-830.

Beard, J.L., Connor, J.R., Jones, B.C., 1993. Iron in the brain. Nutr Rev 51, 157-170.

Benson, R.R., Gattu, R., Sewick, B., Kou, Z., Zakariah, N., Cavanaugh, J.M., Haacke, E.M., 2012. Detection of hemorrhagic and axonal pathology in mild traumatic brain injury using advanced MRI: implications for neurorehabilitation. NeuroRehabilitation 31, 261-279.

Bernstein, M.A., King, K.F., Zhou, Z.J., 2004. Handbook of MRI pulse sequences. Academic Press, Amsterdam ; Boston.

Bielekova, B., Martin, R., 2004. Development of biomarkers in multiple sclerosis. Brain : a journal of neurology 127, 1463-1478.

Bizzi, A., Brooks, R.A., Brunetti, A., Hill, J.M., Alger, J.R., Miletich, R.S., Francavilla, T.L., Di Chiro, G., 1990. Role of iron and ferritin in MR imaging of the brain: a study in primates at different field strengths. Radiology 177, 59-65.

Bo, L., Vedeler, C.A., Nyland, H.I., Trapp, B.D., Mork, S.J., 2003. Subpial demyelination in the cerebral cortex of multiple sclerosis patients. J Neuropathol Exp Neurol 62, 723-732.

Brass, S.D., Benedict, R.H., Weinstock-Guttman, B., Munschauer, F., Bakshi, R., 2006. Cognitive impairment is associated with subcortical magnetic resonance imaging grey matter T2 hypointensity in multiple sclerosis. Mult Scler 12, 437-444.

Bronnum-Hansen, H., Koch-Henriksen, N., Stenager, E., 2004. Trends in survival and cause of death in Danish patients with multiple sclerosis. Brain : a journal of neurology 127, 844-850.

Bruck, W., Bitsch, A., Kolenda, H., Bruck, Y., Stiefel, M., Lassmann, H., 1997. Inflammatory central nervous system demyelination: correlation of magnetic resonance imaging findings with lesion pathology. Ann Neurol 42, 783-793.

Bruck, W., Porada, P., Poser, S., Rieckmann, P., Hanefeld, F., Kretzschmar, H.A., Lassmann, H., 1995. Monocyte/macrophage differentiation in early multiple sclerosis lesions. Ann Neurol 38, 788-796.

Brusko, T.M., Wasserfall, C.H., Agarwal, A., Kapturczak, M.H., Atkinson, M.A., 2005. An integral role for heme oxygenase-1 and carbon monoxide in maintaining peripheral tolerance by CD4+CD25+ regulatory T cells. J Immunol 174, 5181-5186.

Burgetova, A., Seidl, Z., Krasensky, J., Horakova, D., Vaneckova, M., 2010. Multiple sclerosis and the accumulation of iron in the Basal Ganglia: quantitative assessment of brain iron using MRI t(2) relaxometry. Eur Neurol 63, 136-143.

Ceccarelli, A., Rocca, M.A., Neema, M., Martinelli, V., Arora, A., Tauhid, S., Ghezzi, A., Comi, G., Bakshi, R., Filippi, M., 2010. Deep gray matter T2 hypointensity is present in patients with clinically isolated syndromes suggestive of multiple sclerosis. Mult Scler 16, 39-44.

Celius, E.G., Harbo, H.F., Egeland, T., Vartdal, F., Vandvik, B., Spurkiand, A., 2000. Sex and age at diagnosis are correlated with the HLA-DR2, DQ6 haplotype in multiple sclerosis. J Neurol Sci 178, 132-135.

Chai, P.J., Skaryak, L.A., Ungerleider, R.M., Greeley, W.J., Kern, F.H., Schulman, S.R., Hansell, D.R., Auten, R.L., Mahaffey, S.F., Meliones, J.N., 1995. Jugular ligation does not increase intracranial pressure but does increase bihemispheric cerebral blood flow and metabolism. Critical care medicine 23, 1864-1871.

Chakeres, D.W., Abduljalil, A.M., Novak, P., Novak, V., 2002. Comparison of 1.5 and 8 tesla high-resolution magnetic resonance imaging of lacunar infarcts. J Comput Assist Tomogr 26, 628-632.

Chao, C.P., Kotsenas, A.L., Broderick, D.F., 2006. Cerebral amyloid angiopathy: CT and MR imaging findings. Radiographics : a review publication of the Radiological Society of North America, Inc 26, 1517-1531.

Chapman, J., Vinokurov, S., Achiron, A., Karussis, D.M., Mitosek-Szewczyk, K., Birnbaum, M., Michaelson, D.M., Korczyn, A.D., 2001. APOE genotype is a major predictor of long-term progression of disability in MS. Neurology 56, 312-316.

Chesselet, M.F., Richter, F., 2011. Modelling of Parkinson's disease in mice. Lancet neurology 10, 1108-1118.

Comabella, M., Balashov, K., Issazadeh, S., Smith, D., Weiner, H.L., Khoury, S.J., 1998. Elevated interleukin-12 in progressive multiple sclerosis correlates with disease activity and is normalized by pulse cyclophosphamide therapy. J Clin Invest 102, 671-678.

Confavreux, C., Aimard, G., Devic, M., 1980. Course and prognosis of multiple sclerosis assessed by the computerized data processing of 349 patients. Brain : a journal of neurology 103, 281-300.

Confavreux, C., Vukusic, S., 2006. Natural history of multiple sclerosis: a unifying concept. Brain : a journal of neurology 129, 606-616.

Confavreux, C., Vukusic, S., 2008. The clinical epidemiology of multiple sclerosis. Neuroimaging Clin N Am 18, 589-622, ix-x.

Connor, J.R., Menzies, S.L., 1995. Cellular management of iron in the brain. J Neurol Sci 134 Suppl, 33-44.

Connor, J.R., Snyder, B.S., Arosio, P., Loeffler, D.A., LeWitt, P., 1995. A quantitative analysis of isoferritins in select regions of aged, parkinsonian, and Alzheimer's diseased brains. Journal of neurochemistry 65, 717-724.

Connor, J.R., Snyder, B.S., Beard, J.L., Fine, R.E., Mufson, E.J., 1992. Regional distribution of iron and iron-regulatory proteins in the brain in aging and Alzheimer's disease. Journal of neuroscience research 31, 327-335.

Cottrell, D.A., Kremenchutzky, M., Rice, G.P., Koopman, W.J., Hader, W., Baskerville, J., Ebers, G.C., 1999. The natural history of multiple sclerosis: a geographically based study. 5. The clinical features and natural history of primary progressive multiple sclerosis. Brain : a journal of neurology 122 (Pt 4), 625-639.

Craelius, W., Migdal, M.W., Luessenhop, C.P., Sugar, A., Mihalakis, I., 1982. Iron deposits surrounding multiple sclerosis plaques. Arch Pathol Lab Med 106, 397-399.

Crawford, M.P., Yan, S.X., Ortega, S.B., Mehta, R.S., Hewitt, R.E., Price, D.A., Stastny, P., Douek, D.C., Koup, R.A., Racke, M.K., Karandikar, N.J., 2004. High prevalence of autoreactive, neuroantigen-specific CD8+ T cells in multiple sclerosis revealed by novel flow cytometric assay. Blood 103, 4222-4231.

Cunnane, S.C., Ho, S.Y., Dore-Duffy, P., Ells, K.R., Horrobin, D.F., 1989. Essential fatty acid and lipid profiles in plasma and erythrocytes in patients with multiple sclerosis. Am J Clin Nutr 50, 801-806.

Damadian, R.V., Chu, D., 2011. The possible role of cranio-cervical trauma and abnormal CSF hydrodynamics in the genesis of multiple sclerosis. Physiol Chem Phys Med NMR 41, 1-17.

De Stefano, N., Narayanan, S., Matthews, P.M., Francis, G.S., Antel, J.P., Arnold, D.L., 1999. In vivo evidence for axonal dysfunction remote from focal cerebral demyelination of the type seen in multiple sclerosis. Brain : a journal of neurology 122 (Pt 10), 1933-1939.

Dore-Duffy, P., Catalanotto, F., Donaldson, J.O., Ostrom, K.M., Testa, M.A., 1983. Zinc in multiple sclerosis. Ann Neurol 14, 450-454.

Dousset, V., Brochet, B., Deloire, M.S., Lagoarde, L., Barroso, B., Caille, J.M., Petry, K.G., 2006. MR imaging of relapsing multiple sclerosis patients using ultra-small-particle iron oxide and compared with gadolinium. AJNR Am J Neuroradiol 27, 1000-1005.

Dousset, V., Brochet, B., Vital, A., Gross, C., Benazzouz, A., Boullerne, A., Bidabe, A.M., Gin, A.M., Caille, J.M., 1995. Lysolecithin-induced demyelination in primates: preliminary in vivo study with MR and magnetization transfer. AJNR Am J Neuroradiol 16, 225-231.

Drayer, B., Burger, P., Hurwitz, B., Dawson, D., Cain, J., 1987. Reduced signal intensity on MR images of thalamus and putamen in multiple sclerosis: increased iron content? AJR Am J Roentgenol 149, 357-363.

Duda, P.W., Schmied, M.C., Cook, S.L., Krieger, J.I., Hafler, D.A., 2000. Glatiramer acetate (Copaxone) induces degenerate, Th2-polarized immune responses in patients with multiple sclerosis. J Clin Invest 105, 967-976.

Duhaime, A.C., 2006. Large animal models of traumatic injury to the immature brain. Developmental neuroscience 28, 380-387.

Duvernoy, H., 1999. Human Brainstem Vessels., 2nd ed. ed. Springer-Verlag, Berlin.

Eissa, A., Lebel, R.M., Korzan, J.R., Zavodni, A.E., Warren, K.G., Catz, I., Emery, D.J., Wilman, A.H., 2009. Detecting lesions in multiple sclerosis at 4.7 tesla using phase susceptibility-weighting and T2-weighting. J Magn Reson Imaging 30, 737-742.

Fazekas, F., Strasser-Fuchs, S., Schmidt, H., Enzinger, C., Ropele, S., Lechner, A., Flooh, E., Schmidt, R., Hartung, H.P., 2000. Apolipoprotein E genotype related differences in brain lesions of multiple sclerosis. J Neurol Neurosurg Psychiatry 69, 25-28.

Feng, W., Utriainen, D., Trifan, G., Sethi, S., Hubbard, D., Haacke, E.M., 2012b. Quantitative flow measurements in the internal jugular veins of multiple sclerosis patients using magnetic resonance imaging. Reviews on recent clinical trials 7, 117-126.

Ferguson, B., Matyszak, M.K., Esiri, M.M., Perry, V.H., 1997. Axonal damage in acute multiple sclerosis lesions. Brain : a journal of neurology 120 (Pt 3), 393-399.

Filippi, M., Rocca, M.A., 2009. MR Imaging of Gray Matter Involvement in Multiple Sclerosis: Implications for Understanding Disease Pathophysiology and Monitoring Treatment Efficacy. AJNR Am J Neuroradiol.

Filippi, M., Rocca, M.A., Martino, G., Horsfield, M.A., Comi, G., 1998. Magnetization transfer changes in the normal appearing white matter precede the appearance of enhancing lesions in patients with multiple sclerosis. Ann Neurol 43, 809-814.

Fog, T., 1964. On the Vessel-Plaque Relationships in the Brain in Multiple Sclerosis. Acta Neurol Scand Suppl 40, SUPPL 10:19-15.

Fontenot, J.D., Rudensky, A.Y., 2004. Molecular aspects of regulatory T cell development. Semin Immunol 16, 73-80.

Forge, J.K., Pedchenko, T.V., LeVine, S.M., 1998. Iron deposits in the central nervous system of SJL mice with experimental allergic encephalomyelitis. Life sciences 63, 2271-2284.

Frahm J, H.A., Matthei D, et al., 1986. FLASH imaging: Rapid imaging using low flip angle pulses. . J Magn Reson Imaging 67, 256-266.

Frahm, J., Haase, A., Matthaei, D., 1986. Rapid three-dimensional MR imaging using the FLASH technique. J Comput Assist Tomogr 10, 363-368.

Frohman, E.M., Eagar, T., Monson, N., Stuve, O., Karandikar, N., 2008. Immunologic mechanisms of multiple sclerosis. Neuroimaging Clin N Am 18, 577-588, ix.

Frohman, E.M., Goodin, D.S., Calabresi, P.A., Corboy, J.R., Coyle, P.K., Filippi, M., Frank, J.A., Galetta, S.L., Grossman, R.I., Hawker, K., Kachuck, N.J., Levin, M.C., Phillips, J.T., Racke, M.K., Rivera, V.M., Stuart, W.H., 2003. The utility of MRI in suspected MS: report of the Therapeutics and Technology Assessment Subcommittee of the American Academy of Neurology. Neurology 61, 602-611.

Frohman, E.M., Racke, M.K., Raine, C.S., 2006. Multiple sclerosis--the plaque and its pathogenesis. N Engl J Med 354, 942-955.

Ge, Y., Law, M., Johnson, G., Herbert, J., Babb, J.S., Mannon, L.J., Grossman, R.I., 2005. Dynamic susceptibility contrast perfusion MR imaging of multiple sclerosis lesions: characterizing hemodynamic impairment and inflammatory activity. AJNR Am J Neuroradiol 26, 1539-1547.

Ge, Y., Zohrabian, V.M., Osa, E.O., Xu, J., Jaggi, H., Herbert, J., Haacke, E.M., Grossman, R.I., 2009. Diminished visibility of cerebral venous vasculature in multiple sclerosis by susceptibility-weighted imaging at 3.0 Tesla. J Magn Reson Imaging 29, 1190-1194.

Gelman, N., Gorell, J.M., Barker, P.B., Savage, R.M., Spickler, E.M., Windham, J.P., Knight, R.A., 1999. MR imaging of human brain at 3.0 T: preliminary report on transverse relaxation rates and relation to estimated iron content. Radiology 210, 759-767.

Gh Popescu, B.F., George, M.J., Bergmann, U., Garachtchenko, A.V., Kelly, M.E., McCrea, R.P., Luning, K., Devon, R.M., George, G.N., Hanson, A.D., Harder, S.M., Chapman, L.D., Pickering, I.J., Nichol, H., 2009. Mapping metals in Parkinson's and normal brain using rapid-scanning x-ray fluorescence. Phys Med Biol 54, 651-663.

Ghoshal, N.G., Zguigal, H., 1986. Dural sinuses in the pig and their extracranial venous connections. American journal of veterinary research 47, 1165-1169.

Goodkin, D.E., Hertsgaard, D., Rudick, R.A., 1989. Exacerbation rates and adherence to disease type in a prospectively followed-up population with multiple sclerosis. Implications for clinical trials. Arch Neurol 46, 1107-1112.

Goodman, L., 1953. Alzheimer's disease; a clinico-pathologic analysis of twenty-three cases with a theory on pathogenesis. J Nerv Ment Dis 118, 97-130.

Grant, S.M., Wiesinger, J.A., Beard, J.L., Cantorna, M.T., 2003. Iron-deficient mice fail to develop autoimmune encephalomyelitis. J Nutr 133, 2635-2638.

Grytten Torkildsen, N., Lie, S.A., Aarseth, J.H., Nyland, H., Myhr, K.M., 2008. Survival and cause of death in multiple sclerosis: results from a 50-year follow-up in Western Norway. Multiple sclerosis 14, 1191-1198.

Gutteridge, J.M., 1992. Iron and oxygen radicals in brain. Ann Neurol 32 Suppl, S16-21.

Haacke, E., Brown, R., Thompson, M., Venkatesan, R., 1999. Magnetic Resonance Imaging - Physical Principles and Sequence Design. Wiley-Liss.

Haacke, E., Reichenbach, J.R., 2011. Susceptibility Weighted Imaging in MRI: Basic Concepts and Clinical Applications. Wiley-Blackwell.

Haacke, E.M., 1999. Magnetic resonance imaging : physical principles and sequence design. Wiley, New York.

Haacke, E.M., 2011. Chronic cerebral spinal venous insufficiency in multiple sclerosis. Expert review of neurotherapeutics 11, 5-9.

Haacke, E.M., Ayaz, M., Khan, A., Manova, E.S., Krishnamurthy, B., Gollapalli, L., Ciulla, C., Kim, I., Petersen, F., Kirsch, W., 2007. Establishing a baseline phase behavior in magnetic resonance imaging to determine normal vs. abnormal iron content in the brain. J Magn Reson Imaging 26, 256-264.

Haacke, E.M., Beggs, C.B., Habib, C., 2012b. The role of venous abnormalities in neurological disease. Rev Recent Clin Trials 7, 100-116.

Haacke, E.M., Cheng, N.Y., House, M.J., Liu, Q., Neelavalli, J., Ogg, R.J., Khan, A., Ayaz, M., Kirsch, W., Obenaus, A., 2005. Imaging iron stores in the brain using magnetic resonance imaging. Magnetic resonance imaging 23, 1-25.

Haacke, E.M., Feng, W., Utriainen, D., Trifan, G., Wu, Z., Latif, Z., Katkuri, Y., Hewett, J., Hubbard, D., 2012c. Patients with multiple sclerosis with structural venous abnormalities on MR imaging exhibit an abnormal flow distribution of the internal jugular veins. J Vasc Interv Radiol 23, 60-68 e61-63.

Haacke, E.M., Garbern, J., Miao, Y., Habib, C., Liu, M., 2010a. Iron stores and cerebral veins in MS studied by susceptibility weighted imaging. Int Angiol 29, 149-157.

Haacke, E.M., Makki, M., Ge, Y., Maheshwari, M., Sehgal, V., Hu, J., Selvan, M., Wu, Z., Latif, Z., Xuan, Y., Khan, O., Garbern, J., Grossman, R.I., 2009a. Characterizing iron deposition in multiple sclerosis lesions using susceptibility weighted imaging. J Magn Reson Imaging 29, 537-544.

Haacke, E.M., Miao, Y.W., Liu, M., Habib, C.A., Katkuri, Y., Liu, T., Yang, Z., Lang, Z., Hu, J., Hu, J., 2010c. Correlation of putative iron content as represented by changes in R2* and phase with age in deep gray matter of healthy adults. J Magn Reson *32*, 561-557.

Haacke, E.M., Mittal, S., Wu, Z., Neelavalli, J., Cheng, Y.C., 2009b. Susceptibility-weighted imaging: technical aspects and clinical applications, part 1. AJNR Am J Neuroradiol 30, 19-30.

Haacke, E.M., Xu, Y., Cheng, Y.C., Reichenbach, J.R., 2004. Susceptibility weighted imaging (SWI). Magn Reson Med 52, 612-618.

Habib, C.Z., W., Haacke, E., Webb, S., Nichol, H., Year Visualizing iron deposition in multiple sclerosis cadaver brains. In 6th International Conference on Medical Applications of Synchrotron Radiation. Melbourne (Australia).

Hagemeier, J., Dwyer, M.G., Bergsland, N., Schweser, F., Magnano, C.R., Heininen-Brown, M., Ramasamy, D.P., Carl, E., Kennedy, C., Melia, R., Polak, P., Deistung, A., Geurts, J.J., Reichenbach, J.R., Zivadinov, R., 2013. Effect of Age on MRI Phase Behavior in the Subcortical Deep Gray Matter of Healthy Individuals. AJNR Am J Neuroradiol.

Hallgren, B., Sourander, P., 1958. The effect of age on the non-haemin iron in the human brain. Journal of neurochemistry 3, 41-51.

Hammond, K.E., Metcalf, M., Carvajal, L., Okuda, D.T., Srinivasan, R., Vigneron, D., Nelson, S.J., Pelletier, D., 2008. Quantitative in vivo magnetic resonance imaging of multiple sclerosis at 7 Tesla with sensitivity to iron. Ann Neurol 64, 707-713.

Hare, D., Ayton, S., Bush, A., Lei, P., 2013. A delicate balance: Iron metabolism and diseases of the brain. Frontiers in aging neuroscience 5, 34.

Hauser, S.L., Waubant, E., Arnold, D.L., Vollmer, T., Antel, J., Fox, R.J., Bar-Or, A., Panzara, M., Sarkar, N., Agarwal, S., Langer-Gould, A., Smith, C.H., 2008. B-cell depletion with rituximab in relapsing-remitting multiple sclerosis. N Engl J Med 358, 676-688.

He, J., Inglese, M., Li, B.S., Babb, J.S., Grossman, R.I., Gonen, O., 2005. Relapsing-remitting multiple sclerosis: metabolic abnormality in nonenhancing lesions and normal-appearing white matter at MR imaging: initial experience. Radiology 234, 211-217.

Ho, S.Y., Catalanotto, F.A., Lisak, R.P., Dore-Duffy, P., 1986. Zinc in multiple sclerosis. II: Correlation with disease activity and elevated plasma membrane-bound zinc in erythrocytes from patients with multiple sclerosis. Ann Neurol 20, 712-715.

Hochmeister, S., Grundtner, R., Bauer, J., Engelhardt, B., Lyck, R., Gordon, G., Korosec, T., Kutzelnigg, A., Berger, J.J., Bradl, M., Bittner, R.E., Lassmann, H., 2006. Dysferlin is a new marker for leaky brain blood vessels in multiple sclerosis. J Neuropathol Exp Neurol 65, 855-865.

Hynson, J.L., Kornberg, A.J., Coleman, L.T., Shield, L., Harvey, A.S., Kean, M.J., 2001. Clinical and neuroradiologic features of acute disseminated encephalomyelitis in children. Neurology 56, 1308-1312.

Imaizumi, T., Chiba, M., Honma, T., Niwa, J., 2003. Detection of hemosiderin deposition by T2*-weighted MRI after subarachnoid hemorrhage. Stroke; a journal of cerebral circulation 34, 1693-1698.

Inglese, M., Park, S.J., Johnson, G., Babb, J.S., Miles, L., Jaggi, H., Herbert, J., Grossman, R.I., 2007. Deep gray matter perfusion in multiple sclerosis: dynamic susceptibility contrast perfusion magnetic resonance imaging at 3 T. Arch Neurol 64, 196-202.

Jensen, J.H., Szulc, K., Hu, C., Ramani, A., Lu, H., Xuan, L., Falangola, M.F., Chandra, R., Knopp, E.A., Schenck, J., Zimmerman, E.A., Helpern, J.A., 2009. Magnetic field correlation as a measure of iron-generated magnetic field inhomogeneities in the brain. Magn Reson Med 61, 481-485.

Kappos, L., Polman, C.H., Freedman, M.S., Edan, G., Hartung, H.P., Miller, D.H., Montalban, X., Barkhof, F., Bauer, L., Jakobs, P., Pohl, C., Sandbrink, R., 2006. Treatment with interferon beta-1b delays conversion to clinically definite and McDonald MS in patients with clinically isolated syndromes. Neurology 67, 1242-1249.

Karandikar, N.J., Crawford, M.P., Yan, X., Ratts, R.B., Brenchley, J.M., Ambrozak, D.R., Lovett-Racke, A.E., Frohman, E.M., Stastny, P., Douek, D.C., Koup, R.A., Racke, M.K., 2002. Glatiramer acetate (Copaxone) therapy induces CD8(+) T cell responses in patients with multiple sclerosis. J Clin Invest 109, 641-649.

Ke, Y., 2003. Iron misregulation in the brain: a primary cause of neurodegeneration disorders. Lancet neurology 2, 246-253.

Kidd, D., Barkhof, F., McConnell, R., Algra, P.R., Allen, I.V., Revesz, T., 1999. Cortical lesions in multiple sclerosis. Brain : a journal of neurology 122 (Pt 1), 17-26.

Kim, E., Na, D.G., Kim, E.Y., Kim, J.H., Son, K.R., Chang, K.H., 2007. MR imaging of metronidazole-induced encephalopathy: lesion distribution and diffusion-weighted imaging findings. AJNR Am J Neuroradiol 28, 1652-1658.

Kleinig, T.J., 2013. Associations and implications of cerebral microbleeds. Journal of clinical neuroscience : official journal of the Neurosurgical Society of Australasia 20, 919-927.

Koeppen, A.H., 1995. The history of iron in the brain. J Neurol Sci 134 Suppl, 1-9.

Konofal, E., Lecendreux, M., Arnulf, I., Mouren, M.C., 2004. Iron deficiency in children with attention-deficit/hyperactivity disorder. Archives of pediatrics & adolescent medicine 158, 1113-1115.

Kornek, B., Storch, M.K., Weissert, R., Wallstroem, E., Stefferl, A., Olsson, T., Linington, C., Schmidbauer, M., Lassmann, H., 2000. Multiple sclerosis and chronic autoimmune encephalomyelitis: a comparative quantitative study of axonal injury in active, inactive, and remyelinated lesions. Am J Pathol 157, 267-276.

Kornum, B.R., Knudsen, G.M., 2011. Cognitive testing of pigs (Sus scrofa) in translational biobehavioral research. Neuroscience and biobehavioral reviews 35, 437-451.

Kurtzke, J.F., Beebe, G.W., Nagler, B., Auth, T.L., Kurland, L.T., Nefzger, M.D., 1973. Studies on the natural history of multiple sclerosis. 7. Correlates of clinical change in an early bout. Acta Neurol Scand 49, 379-395.

Kutzelnigg, A., Lucchinetti, C.F., Stadelmann, C., Bruck, W., Rauschka, H., Bergmann, M., Schmidbauer, M., Parisi, J.E., Lassmann, H., 2005. Cortical demyelination and diffuse white matter injury in multiple sclerosis. Brain : a journal of neurology 128, 2705-2712.

Langer-Gould, A., Brara, S.M., Beaber, B.E., Zhang, J.L., 2013. Incidence of multiple sclerosis in multiple racial and ethnic groups. Neurology 80, 1734-1739.

Langkammer, C., Ropele, S., Pirpamer, L., Fazekas, F., Schmidt, R., 2013. MRI for Iron Mapping in Alzheimer's Disease. Neuro-degenerative diseases.

Lassmann, H., 2008. The pathologic substrate of magnetic resonance alterations in multiple sclerosis. Neuroimaging Clin N Am 18, 563-576, ix.

Lassmann, H., Bruck, W., Lucchinetti, C.F., 2007. The immunopathology of multiple sclerosis: an overview. Brain Pathol 17, 210-218.

Lavoie, P., Metellus, P., Velly, L., Vidal, V., Rolland, P.H., Mekaouche, M., Dubreuil, G., Levrier, O., 2008. Functional cerebral venous outflow in swine and baboon: feasibility of an intracranial venous hypertension model. Journal of investigative surgery : the official journal of the Academy of Surgical Research 21, 323-329.

Law, M., Saindane, A.M., Ge, Y., Babb, J.S., Johnson, G., Mannon, L.J., Herbert, J., Grossman, R.I., 2004. Microvascular abnormality in relapsing-remitting multiple sclerosis: perfusion MR imaging findings in normal-appearing white matter. Radiology 231, 645-652.

Levin, M.C., Lee, S.M., Kalume, F., Morcos, Y., Dohan, F.C., Jr., Hasty, K.A., Callaway, J.C., Zunt, J., Desiderio, D., Stuart, J.M., 2002. Autoimmunity due to molecular mimicry as a cause of neurological disease. Nat Med 8, 509-513.

LeVine, S.M., 1997. Iron deposits in multiple sclerosis and Alzheimer's disease brains. Brain Res 760, 298-303.

Levine, S.M., Chakrabarty, A., 2004. The role of iron in the pathogenesis of experimental allergic encephalomyelitis and multiple sclerosis. Ann N Y Acad Sci 1012, 252-266.

Li, Y., Zhang, L., Kallakuri, S., Zhou, R., Cavanaugh, J.M., 2011. Quantitative relationship between axonal injury and mechanical response in a rodent head impact acceleration model. Journal of neurotrauma 28, 1767-1782.

Lim, I.A., Faria, A.V., Li, X., Hsu, J.T., Airan, R.D., Mori, S., van Zijl, P.C., 2013. Human brain atlas for automated region of interest selection in quantitative susceptibility mapping: Application to determine iron content in deep gray matter structures. NeuroImage 82C, 449-469.

Liu, C., Li, W., Johnson, G.A., Wu, B., 2011. High-field (9.4 T) MRI of brain dysmyelination by quantitative mapping of magnetic susceptibility. NeuroImage 56, 930-938.

Liu, Y., Lai, W.H., Liao, S.Y., Siu, C.W., Yang, Y.Z., Tse, H.F., 2012. Lack of Cardiac Nerve Sprouting after Intramyocardial Transplantation of Bone Marrow-Derived Stem Cells in a Swine Model of Chronic Ischemic Myocardium. Journal of cardiovascular translational research.

Lovett-Racke, A.E., Trotter, J.L., Lauber, J., Perrin, P.J., June, C.H., Racke, M.K., 1998. Decreased dependence of myelin basic protein-reactive T cells on CD28-mediated costimulation in multiple sclerosis patients. A marker of activated/memory T cells. J Clin Invest 101, 725-730.

Lucchinetti, C., Bruck, W., Parisi, J., Scheithauer, B., Rodriguez, M., Lassmann, H., 2000. Heterogeneity of multiple sclerosis lesions: implications for the pathogenesis of demyelination. Ann Neurol 47, 707-717.

Mao, J.C., Pace, E., Pierozynski, P., Kou, Z., Shen, Y., Vandevord, P., Haacke, E.M., Zhang, X., Zhang, J., 2012. Blast-induced tinnitus and hearing loss in rats: behavioral and imaging assays. Journal of neurotrauma 29, 430-444.

McDonnell, G.V., Hawkins, S.A., 1998. Clinical study of primary progressive multiple sclerosis in Northern Ireland, UK. J Neurol Neurosurg Psychiatry 64, 451-454.

Miao, Y., Liu T , Wu JL, Year Correlation Study of Susceptibility Weighted Imaging (SWI) Study on Deep Brain Gray Nuclei and Age. In The 94th RSNA. Chicago.

Miller, D.H., Rudge, P., Johnson, G., Kendall, B.E., Macmanus, D.G., Moseley, I.F., Barnes, D., McDonald, W.I., 1988. Serial gadolinium enhanced magnetic resonance imaging in multiple sclerosis. Brain : a journal of neurology 111 (Pt 4), 927-939.

Milo, R., Kahana, E., 2010. Multiple sclerosis: geoepidemiology, genetics and the environment. Autoimmun Rev 9, A387-394.

Minderhoud, J.M., van der Hoeven, J.H., Prange, A.J., 1988. Course and prognosis of chronic progressive multiple sclerosis. Results of an epidemiological study. Acta Neurol Scand 78, 10-15.

Mittal, S., Wu, Z., Neelavalli, J., Haacke, E.M., 2009. Susceptibility-weighted imaging: technical aspects and clinical applications, part 2. AJNR Am J Neuroradiol 30, 232-252.

Moos, T., Rosengren Nielsen, T., Skjorringe, T., Morgan, E.H., 2007. Iron trafficking inside the brain. Journal of neurochemistry 103, 1730-1740.

Moran, P.R., Moran, R.A., Karstaedt, N., 1985. Verification and evaluation of internal flow and motion. True magnetic resonance imaging by the phase gradient modulation method. Radiology 154, 433-441.

Morris, C.M., Candy, J.M., Oakley, A.E., Bloxham, C.A., Edwardson, J.A., 1992. Histochemical distribution of non-haem iron in the human brain. Acta anatomica 144, 235-257.

Mugler, J.P., 3rd, Brookeman, J.R., 1990. Three-dimensional magnetization-prepared rapid gradient-echo imaging (3D MP RAGE). Magn Reson Med 15, 152-157.

Muhoberac, B.B., Vidal, R., 2013. Abnormal iron homeostasis and neurodegeneration. Frontiers in aging neuroscience 5, 32.

Neema, M., Arora, A., Healy, B.C., Guss, Z.D., Brass, S.D., Duan, Y., Buckle, G.J., Glanz, B.I., Stazzone, L., Khoury, S.J., Weiner, H.L., Guttmann, C.R., Bakshi, R., 2009. Deep gray matter involvement on brain MRI scans is associated with clinical progression in multiple sclerosis. J Neuroimaging 19, 3-8.

Neema, M., Stankiewicz, J., Arora, A., Dandamudi, V.S., Batt, C.E., Guss, Z.D., Al-Sabbagh, A., Bakshi, R., 2007. T1- and T2-based MRI measures of diffuse gray matter and white matter damage in patients with multiple sclerosis. J Neuroimaging 17 Suppl 1, 16S-21S.

Nelson, F., Poonawalla, A.H., Hou, P., Huang, F., Wolinsky, J.S., Narayana, P.A., 2007. Improved identification of intracortical lesions in multiple sclerosis with phase-sensitive inversion recovery in combination with fast double inversion recovery MR imaging. AJNR Am J Neuroradiol 28, 1645-1649.

Noseworthy, J.H., Lucchinetti, C., Rodriguez, M., Weinshenker, B.G., 2000a. Multiple sclerosis. N Engl J Med 343, 938-952.

Noseworthy, J.H., Wolinsky, J.S., Lublin, F.D., Whitaker, J.N., Linde, A., Gjorstrup, P., Sullivan, H.C., 2000b. Linomide in relapsing and secondary progressive MS: part I: trial design and clinical results. North American Linomide Investigators. Neurology 54, 1726-1733.

Ogg, R.J., Langston, J.W., Haacke, E.M., Steen, R.G., Taylor, J.S., 1999. The correlation between phase shifts in gradient-echo MR images and regional brain iron concentration. Magnetic resonance imaging 17, 1141-1148.

Ogg, R.J., Steen, R.G., 1998. Age-related changes in brain T1 are correlated with iron concentration. Magn Reson Med 40, 749-753.

Ordidge, R.J., Gorell, J.M., Deniau, J.C., Knight, R.A., Helpern, J.A., 1994. Assessment of relative brain iron concentrations using T2-weighted and T2*-weighted MRI at 3 Tesla. Magn Reson Med 32, 335-341.

Owens, G.P., Ritchie, A.M., Burgoon, M.P., Williamson, R.A., Corboy, J.R., Gilden, D.H., 2003. Single-cell repertoire analysis demonstrates that clonal expansion is a prominent feature of the B cell response in multiple sclerosis cerebrospinal fluid. J Immunol 171, 2725-2733.

Panitch, H.S., Hirsch, R.L., Haley, A.S., Johnson, K.P., 1987. Exacerbations of multiple sclerosis in patients treated with gamma interferon. Lancet 1, 893-895.

Patani, R., Balaratnam, M., Vora, A., Reynolds, R., 2007. Remyelination can be extensive in multiple sclerosis despite a long disease course. Neuropathol Appl Neurobiol 33, 277-287.

Pfefferbaum, A., Adalsteinsson, E., Rohlfing, T., Sullivan, E.V., 2009. MRI estimates of brain iron concentration in normal aging: comparison of field-dependent (FDRI) and phase (SWI) methods. NeuroImage 47, 493-500.

Polman, C.H., Reingold, S.C., Edan, G., Filippi, M., Hartung, H.P., Kappos, L., Lublin, F.D., Metz, L.M., McFarland, H.F., O'Connor, P.W., Sandberg-Wollheim, M., Thompson, A.J., Weinshenker, B.G., Wolinsky, J.S., 2005. Diagnostic criteria for multiple sclerosis: 2005 revisions to the "McDonald Criteria". Ann Neurol 58, 840-846.

Popescu, B.F., Robinson, C.A., Chapman, L.D., Nichol, H., 2009a. Synchrotron X-ray fluorescence reveals abnormal metal distributions in brain and spinal cord in spinocerebellar ataxia: a case report. Cerebellum 8, 340-351.

Popescu, B.F., Robinson, C.A., Rajput, A., Rajput, A.H., Harder, S.L., Nichol, H., 2009b. Iron, copper, and zinc distribution of the cerebellum. Cerebellum 8, 74-79.

Poser, C.M., Paty, D.W., Scheinberg, L., McDonald, W.I., Davis, F.A., Ebers, G.C., Johnson, K.P., Sibley, W.A., Silberberg, D.H., Tourtellotte, W.W., 1983. New diagnostic criteria for multiple sclerosis: guidelines for research protocols. Ann Neurol 13, 227-231.

Prineas, J.W., Barnard, R.O., Revesz, T., Kwon, E.E., Sharer, L., Cho, E.S., 1993. Multiple sclerosis. Pathology of recurrent lesions. Brain : a journal of neurology 116 (Pt 3), 681-693.

Prineas, J.W., Kwon, E.E., Cho, E.S., Sharer, L.R., Barnett, M.H., Oleszak, E.L., Hoffman, B., Morgan, B.P., 2001. Immunopathology of secondary-progressive multiple sclerosis. Ann Neurol 50, 646-657.

Prineas, J.W., Kwon, E.E., Goldenberg, P.Z., Ilyas, A.A., Quarles, R.H., Benjamins, J.A., Sprinkle, T.J., 1989. Multiple sclerosis. Oligodendrocyte proliferation and differentiation in fresh lesions. Lab Invest 61, 489-503.

Putnam, T., 1935. Studies in multiple sclerosis: encephalitis and sclerotic plaques produced by venular obstruction. Arch of Neurol and Psych 33, 929-940.

Quintana, C., 2007. About the presence of Hemosiderin in the Hippocampus of Alzheimer Patients. Journal Of Alzheimer's Disease 12, 157-160.

Quintana, C., Bellefqih, S., Laval, J.Y., Guerquin-Kern, J.L., Wu, T.D., Avila, J., Ferrer, I., Arranz, R., Patino, C., 2006. Study of the localization of iron, ferritin, and hemosiderin in Alzheimer's disease hippocampus by analytical microscopy at the subcellular level. J Struct Biol 153, 42-54.

Ramagopalan, S.V., Dobson, R., Meier, U.C., Giovannoni, G., 2010. Multiple sclerosis: risk factors, prodromes, and potential causal pathways. Lancet neurology 9, 727-739.

Rashid, W., Parkes, L.M., Ingle, G.T., Chard, D.T., Toosy, A.T., Altmann, D.R., Symms, M.R., Tofts, P.S., Thompson, A.J., Miller, D.H., 2004. Abnormalities of cerebral perfusion in multiple sclerosis. J Neurol Neurosurg Psychiatry 75, 1288-1293.

Rauscher, A., Sedlacik, J., Barth, M., Mentzel, H.J., Reichenbach, J.R., 2005. Magnetic susceptibility-weighted MR phase imaging of the human brain. AJNR Am J Neuroradiol 26, 736-742.

Reffelmann, T., Sensebat, O., Birnbaum, Y., Stroemer, E., Hanrath, P., Uretsky, B.F., Schwarz, E.R., 2004. A novel minimal-invasive model of chronic myocardial infarction in swine. Coronary artery disease 15, 7-12.

Reichenbach, J.R., Venkatesan, R., Schillinger, D.J., Kido, D.K., Haacke, E.M., 1997. Small vessels in the human brain: MR venography with deoxyhemoglobin as an intrinsic contrast agent. Radiology 204, 272-277.

Renoux, C., Vukusic, S., Mikaeloff, Y., Edan, G., Clanet, M., Dubois, B., Debouverie, M., Brochet, B., Lebrun-Frenay, C., Pelletier, J., Moreau, T., Lubetzki, C., Vermersch, P., Roullet, E., Magy, L., Tardieu, M., Suissa, S., Confavreux, C., Adult Neurology Departments, K.S.G., 2007. Natural history of multiple sclerosis with childhood onset. N Engl J Med 356, 2603-2613.

Rocca, M.A., Iannucci, G., Rovaris, M., Comi, G., Filippi, M., 2003. Occult tissue damage in patients with primary progressive multiple sclerosis is independent of T2-visible lesions--a diffusion tensor MR study. J Neurol 250, 456-460.

Ropele, S., de Graaf, W., Khalil, M., Wattjes, M.P., Langkammer, C., Rocca, M.A., Rovira, A., Palace, J., Barkhof, F., Filippi, M., Fazekas, F., 2011. MRI assessment of iron deposition in multiple sclerosis. J Magn Reson Imaging 34, 13-21.

Runmarker, B., Andersson, C., Oden, A., Andersen, O., 1994. Prediction of outcome in multiple sclerosis based on multivariate models. J Neurol 241, 597-604.

San Millan Ruiz, D., Fasel, J.H., Gailloud, P., 2012. Unilateral hypoplasia of the rostral end of the superior sagittal sinus. AJNR Am J Neuroradiol 33, 286-291.

Sasaki, M., Shibata, E., Tohyama, K., Takahashi, J., Otsuka, K., Tsuchiya, K., Takahashi, S., Ehara, S., Terayama, Y., Sakai, A., 2006. Neuromelanin magnetic resonance imaging of locus ceruleus and substantia nigra in Parkinson's disease. Neuroreport 17, 1215-1218.

Schafer, A., Wharton, S., Gowland, P., Bowtell, R., 2009. Using magnetic field simulation to study susceptibility-related phase contrast in gradient echo MRI. NeuroImage 48, 126-137.

Schelling, F., 1986. Damaging venous reflux into the skull or spine: relevance to multiple sclerosis. Med Hypotheses 21, 141-148.

Schenck, J.F., Zimmerman, E.A., 2004. High-field magnetic resonance imaging of brain iron: birth of a biomarker? NMR Biomed 17, 433-445.

Schenker, C., Meier, D., Wichmann, W., Boesiger, P., Valavanis, A., 1993. Age distribution and iron dependency of the T2 relaxation time in the globus pallidus and putamen. Neuroradiology 35, 119-124.

Schneider, R., 2009. Neuronal degeneration in a viral model of multiple sclerosis. The Journal of neuroscience : the official journal of the Society for Neuroscience 29, 15353-15354.

Schook, L., Beattie, C., Beever, J., Donovan, S., Jamison, R., Zuckermann, F., Niemi, S., Rothschild, M., Rutherford, M., Smith, D., 2005. Swine in biomedical research: creating the building blocks of animal models. Animal biotechnology 16, 183-190.

Schutze, M., Janda, M., Bajorat, J., Piek, J., Noldge-Schomburg, G.F., Hofmockel, R., 2007. A surgical technique for catheterization of the sagittal sinus in pigs. Lab Anim 41, 492-495.

Semnic, R., Svetel, M., Dragasevic, N., Petrovic, I., Kozic, D., Marinkovic, J., Kostic, V.S., Sener, R.N., 2005. Magnetic resonance imaging morphometry of the midbrain in patients with Wilson disease. J Comput Assist Tomogr 29, 880-883.

Sharma, J., Zivadinov, R., Jaisani, Z., Fabiano, A.J., Singh, B., Horsfield, M.A., Bakshi, R., 2006. A magnetization transfer MRI study of deep gray matter involvement in multiple sclerosis. J Neuroimaging 16, 302-310.

Si, Z., Luan, L., Kong, D., Zhao, G., Wang, H., Zhang, K., Yu, T., Pang, Q., 2008. MRI-based investigation on outflow segment of cerebral venous system under increased ICP condition. Eur J Med Res 13, 121-126.

Siemonsen, S., Finsterbusch, J., Matschke, J., Lorenzen, A., Ding, X.Q., Fiehler, J., 2008. Age-dependent normal values of T2* and T2' in brain parenchyma. AJNR Am J Neuroradiol 29, 950-955.

Singh, A.V., Zamboni, P., 2009. Anomalous venous blood flow and iron deposition in multiple sclerosis. J Cereb Blood Flow Metab.

Sofic, E., Paulus, W., Jellinger, K., Riederer, P., Youdim, M.B., 1991. Selective increase of iron in substantia nigra zona compacta of parkinsonian brains. Journal of neurochemistry 56, 978-982.

Sohmiya, M., Tanaka, M., Aihara, Y., Hirai, S., Okamoto, K., 2001. Age-related structural changes in the human midbrain: an MR image study. Neurobiology of aging 22, 595-601.

Sohmiya, M., Tanaka, M., Aihara, Y., Okamoto, K., 2004. Structural changes in the midbrain with aging and Parkinson's disease: an MRI study. Neurobiology of aging 25, 449-453.

Stankiewicz, J., Panter, S.S., Neema, M., Arora, A., Batt, C.E., Bakshi, R., 2007. Iron in chronic brain disorders: imaging and neurotherapeutic implications. Neurotherapeutics 4, 371-386.

Steimle, V., Siegrist, C.A., Mottet, A., Lisowska-Grospierre, B., Mach, B., 1994. Regulation of MHC class II expression by interferon-gamma mediated by the transactivator gene CIITA. Science 265, 106-109.

Stys, P.K., Waxman, S.G., Ransom, B.R., 1992. Ionic mechanisms of anoxic injury in mammalian CNS white matter: role of Na+ channels and Na(+)-Ca2+ exchanger. The Journal of neuroscience : the official journal of the Society for Neuroscience 12, 430-439.

Sullivan, J.L., 2004. Is stored iron safe? J Lab Clin Med 144, 280-284.

Tintore, M., Rovira, A., Rio, J., Nos, C., Grive, E., Tellez, N., Pelayo, R., Comabella, M., Montalban, X., 2005. Is optic neuritis more benign than other first attacks in multiple sclerosis? Ann Neurol 57, 210-215.

Tjoa, C.W., Benedict, R.H., Weinstock-Guttman, B., Fabiano, A.J., Bakshi, R., 2005. MRI T2 hypointensity of the dentate nucleus is related to ambulatory impairment in multiple sclerosis. J Neurol Sci 234, 17-24.

Tourdias, T., Roggerone, S., Filippi, M., Kanagaki, M., Rovaris, M., Miller, D.H., Petry, K.G., Brochet, B., Pruvo, J.P., Radue, E.W., Dousset, V., 2012. Assessment of disease activity in multiple sclerosis phenotypes with combined gadolinium- and superparamagnetic iron oxide-enhanced MR imaging. Radiology 264, 225-233.

Trapp, B.D., Peterson, J., Ransohoff, R.M., Rudick, R., Mork, S., Bo, L., 1998. Axonal transection in the lesions of multiple sclerosis. N Engl J Med 338, 278-285.

Trojano, M., Avolio, C., Manzari, C., Calo, A., De Robertis, F., Serio, G., Livrea, P., 1995. Multivariate analysis of predictive factors of multiple sclerosis course with a validated method to assess clinical events. J Neurol Neurosurg Psychiatry 58, 300-306.

van Toorn, R., Schoeman, J.F., Solomons, R., Rensburg, M.A., van Rensburg, S.J., 2010. Iron status in children with recurrent episodes of tumefactive cerebral demyelination. J Child Neurol 25, 1401-1407.

van Waesberghe, J.H., Kamphorst, W., De Groot, C.J., van Walderveen, M.A., Castelijns, J.A., Ravid, R., Lycklama a Nijeholt, G.J., van der Valk, P., Polman, C.H., Thompson, A.J., Barkhof, F., 1999. Axonal loss in multiple sclerosis lesions: magnetic resonance imaging insights into substrates of disability. Ann Neurol 46, 747-754.

Varga, A.W., Johnson, G., Babb, J.S., Herbert, J., Grossman, R.I., Inglese, M., 2009. White matter hemodynamic abnormalities precede sub-cortical gray matter changes in multiple sclerosis. J Neurol Sci 282, 28-33.

Villar, L.M., Garcia-Barragan, N., Sadaba, M.C., Espino, M., Gomez-Rial, J., Martinez-San Millan, J., Gonzalez-Porque, P., Alvarez-Cermeno, J.C., 2008. Accuracy of CSF and MRI criteria for dissemination in space in the diagnosis of multiple sclerosis. J Neurol Sci 266, 34-37.

Vymazal, J., Brooks, R.A., Baumgarner, C., Tran, V., Katz, D., Bulte, J.W., Bauminger, R., Di Chiro, G., 1996. The relation between brain iron and NMR relaxation times: an in vitro study. Magn Reson Med 35, 56-61.

Walter, P.B., Knutson, M.D., Paler-Martinez, A., Lee, S., Xu, Y., Viteri, F.E., Ames, B.N., 2002. Iron deficiency and iron excess damage mitochondria and mitochondrial DNA in rats. Proc Natl Acad Sci U S A 99, 2264-2269.

Walton, J.C., Kaufmann, J.C., 1984. Iron deposits and multiple sclerosis. Arch Pathol Lab Med 108, 755-756.

Wang, J., Tan, H.Q., Li, M.H., Sun, X.J., Fu, C.M., Zhu, Y.Q., Zhou, B., Xu, H.W., Wang, W., Xue, B., 2010. Development of a new model of transvenous thrombosis in the pig superior sagittal sinus using thrombin injection and balloon occlusion. Journal of neuroradiology. Journal de neuroradiologie 37, 109-115.

Wegner, C., Esiri, M.M., Chance, S.A., Palace, J., Matthews, P.M., 2006. Neocortical neuronal, synaptic, and glial loss in multiple sclerosis. Neurology 67, 960-967.

Weinshenker, B.G., Rice, G.P., Noseworthy, J.H., Carriere, W., Baskerville, J., Ebers, G.C., 1991. The natural history of multiple sclerosis: a geographically based study. 3.

Multivariate analysis of predictive factors and models of outcome. Brain : a journal of neurology 114 (Pt 2), 1045-1056.

Worthington, V., Killestein, J., Eikelenboom, M.J., Teunissen, C.E., Barkhof, F., Polman, C.H., Uitdehaag, B.M., Petzold, A., 2010. Normal CSF ferritin levels in MS suggest against etiologic role of chronic venous insufficiency. Neurology 75, 1617-1622.

Xu, X., Wang, Q., Zhang, M., 2008. Age, gender, and hemispheric differences in iron deposition in the human brain: an in vivo MRI study. NeuroImage 40, 35-42.

Yang, H., Yang, M., Guan, H., Liu, Z., Zhao, S., Takeuchi, S., Yanagisawa, D., Tooyama, I., 2013. Mitochondrial ferritin in neurodegenerative diseases. Neuroscience research.

Yasui, M., Kihira, T., Ota, K., Mukoyama, M., Adachi, K., Sasajima, K., Iwata, S., 1991. [Zinc concentration in the central nervous system in a case of multiple sclerosis--comparison with other neurological diseases]. No to shinkei = Brain and nerve 43, 951-955.

Zaleski, S., 1886. Das Eisen der Organe bei Morbus maculosus Werlhofii (The iron in Morbus maculosus Werlhofii). Arch. Exp. Patho. Pharmakol 23, 77-90.

Zamboni, P., 2006. The big idea: iron-dependent inflammation in venous disease and proposed parallels in multiple sclerosis. J R Soc Med 99, 589-593.

Zamboni, P., Galeotti, R., Menegatti, E., Malagoni, A.M., Tacconi, G., Dall'Ara, S., Bartolomei, I., Salvi, F., 2009. Chronic cerebrospinal venous insufficiency in patients with multiple sclerosis. J Neurol Neurosurg Psychiatry 80, 392-399.

Zamboni, P., Menegatti, E., Bartolomei, I., Galeotti, R., Malagoni, A.M., Tacconi, G., Salvi, F., 2007. Intracranial venous haemodynamics in multiple sclerosis. Curr Neurovasc Res 4, 252-258.

Zamboni, P., Menegatti, E., Weinstock-Guttman, B., Dwyer, M.G., Schirda, C.V., Malagoni, A.M., Hojnacki, D., Kennedy, C., Carl, E., Bergsland, N., Magnano, C., Bartolomei, I., Salvi, F., Zivadinov, R., 2011. Hypoperfusion of brain parenchyma is associated with the severity of chronic cerebrospinal venous insufficiency in patients with multiple sclerosis: a cross-sectional preliminary report. BMC medicine 9, 22.

Zezula-Szpyra, A., Grzegorzewski, W., 2000. Morphology of the dorsal nasal, frontal and facial veins in adult gilts. Folia Morphol (Warsz) 59, 179-191.

Zhang, Y., Metz, L.M., Yong, V.W., Mitchell, J.R., 2010. 3T deep gray matter T2 hypointensity correlates with disability over time in stable relapsing-remitting multiple sclerosis: a 3-year pilot study. J Neurol Sci 297, 76-81.

Zheng, W., Nichol, H., Liu, S., Cheng, Y.C., Haacke, E.M., 2013. Measuring iron in the brain using quantitative susceptibility mapping and X-ray fluorescence imaging. NeuroImage 78, 68-74.

Zivadinov, R., Ramanathan, M., Dolic, K., Marr, K., Karmon, Y., Siddiqui, A.H., Benedict, R.H., Weinstock-Guttman, B., 2011. Chronic cerebrospinal venous insufficiency in multiple sclerosis: diagnostic, pathogenetic, clinical and treatment perspectives. Expert review of neurotherapeutics 11, 1277-1294.

Zivadinov, R., Schirda, C., Dwyer, M.G., Haacke, M.E., Weinstock-Guttman, B., Menegatti, E., Heininen-Brown, M., Magnano, C., Malagoni, A.M., Wack, D.S., Hojnacki, D., Kennedy, C., Carl, E., Bergsland, N., Hussein, S., Poloni, G., Bartolomei, I., Salvi, F., Zamboni, P., 2010. Chronic cerebrospinal venous insufficiency and iron deposition on susceptibility-weighted imaging in patients with multiple sclerosis: a pilot case-control study. Int Angiol 29, 158-175.

ABSTRACT

IMAGING IRON CONTENT IN PATIENTS WITH MULTIPLE SCLEROSIS USING MAGNETIC RESONANCE IMAGING

by

CHARBEL A. HABIB

December 2013

Advisor: Dr. E. Mark Haacke

Major: Biomedical Engineering

Degree: Doctor of Philosophy

The importance of iron in maintaining normal physiological processes in the human body has been well emphasized in the literature. However, "when iron behaves badly", its abnormal presence might lead to a spectrum of pathologies depending on what function has been altered. In the brain, for instance, abnormal iron content is thought to be associated with neurodegenerative diseases. In this dissertation, we study iron involvement in one of the most debilitating neurological diseases, multiple sclerosis (MS), using *in vivo* magnetic resonance imaging. We first test the sensitivity and specificity of the MR method used, known as susceptibility weighted imaging (SWI) compared to other conventional MR techniques and rapid-scanning X-ray fluorescence in MS cadaver brains. Then, we use SWI phase images to assess iron content in the deep gray matter structures of MS patients compared to normal controls. Finally, we assess the possibility of developing a new MS vascular animal model to study the link between vascular abnormalities, iron deposition and sclerotic lesions.

As a result of this work, we show that SWI provides a better contrast to image the structures and substructures of the brain based on their iron content compared to conventional

MR techniques. The power of SWI in imaging iron content was validated by the use of X-Ray fluorescence (which is known to be an element specific imaging method), showing similar contrast and making SWI the method of choice to image iron content *in vivo*. Using SWI, we show a clear separation between MS patients and normal subjects, when we assessed iron content in the midbrain, thalamus and basal ganglia. We report that out of the seven structures studied, two were more susceptible to abnormal iron deposition (the pulvinar thalamus in young adults, and the red nucleus in elderly people). Finally, in an MR based study, we show that the swine and the human share a similar cerebrovascular drainage system starting from the superficial cerebral veins and deep cervical veins all the way to the heart, aiming to use this model to test the vascular involvement in MS.

AUTOBIOGRAPHICAL STATEMENT

Charbel A. Habib
14287 E 12 Mile Rd Apt D ◆ Warren, MI, 48088 ◆ (312) 961-9631 ◆ dv8118@wayne.edu

Education

2009 - Present	PhD in Biomedical Engineering Wayne State University (WSU) Detroit, MI 48202
2007 - 2009	MS in Biomedical Engineering Wayne State University (WSU) Detroit, MI 48202
2002 - 2007	Bachelor in Electrical Engineering Notre Dame University (NDU) Zouk Mosbeh, Lebanon

Professional Experience

2010 - Present	Research Assistant: Grant Administrator - Department of Radiology – School of Medicine –Wayne University, Detroit, MI
2009 - 2010	Graduate Research Assistant – Department of Radiology – School of Medicine Wayne University, Detroit, MI
2008 - 2009	Graduate Teaching Assistant – Department of Biomedical Engineering – Wayne State University, Detroit, MI
2008	Student Assistant – Department of Radiology – School of Medicine –Wayne State University – Detroit, MI

Publications and Book Chapters

Habib CA, Utriainen D, Peduzzi-Nelson J, Dawe E, Mattei J, Latif Z, Casey K, Haacke EM. MR imaging of the yucatan pig head and neck vasculature**.** J Magn Reson Imaging. 2013 Jan 24.

Haacke, E.M., Beggs C.B., and **Habib CA**. The role of venous abnormalities in neurological disease. Rev Recent Clin Trials, 2012. 7(2): p. 100-16.

Habib CA, Liu M, Bawany N, Garbern J, Krumbein I, Mentzel HJ, Reichenbach J, Magnano C, Zivadinov R, Haacke EM. Assessing abnormal iron content in the deep gray matter of patients with multiple sclerosis versus healthy controls. AJNR Am J Neuroradiol, 2012. 33(2): p. 252-8.

Manju Liu, **Charbel Habib,** Yanwei Miao, and E. Mark Haacke. Measuring Iron Content with Phase. Chapter 22, Susceptibility Weighted Imaging in MRI. Eds. E. Mark Haacke and Jurgen R. Reichenbach, Wiley, 2011. pp 369-402.

Habib CA, Zheng W, Haacke EM, Webb S, Nichol H. "Visualizing iron deposition in multiple sclerosis cadaver brains." *6th International Conference on Medical Applications of Synchrotron Radiation*. AIP Conference Proceedings 2010; (1266), pp. 78-83.

Haacke EM, Garbern J, Miao Y, **Habib CA**, Liu M. Iron Stores and Cerebral Veins in MS Studied by Susceptibility Weighted Imaging. International Angiology 2010; Apr;29(2):149-57.

Haacke EM, Miao YM, Liu M, **Habib CA,** Liu T, Yang Z, Lang Z, et al. Correlation of putative iron content as represented by changes in R2* and phase with age in deep gray matter of healthy adults. J Mag Res Im 2010; Sep;32(3):561-76

Manova ES, **Habib CA**, Boikov AS, et al. Characterizing the mesencephalon using susceptibility-weighted imaging. AJNR Am J Neuroradiol 2009:30:569-574.